# PAVEMENT AIR VOID PROPERTY DETERMINATION AND INCORPORATION OF PAVEMENT AIR VOID PROPERTIES IN PAVEMENT OXIDATION MODELING WITH AN EMPHASIS ON X-RAY CT IMAGE ANALYSIS

A Dissertation

by

AVERY ATTICUS ROSE

Submitted to the Office of Graduate and Professional Studies of
Texas A&M University
in partial fulfillment of the requirements for the degree of

DOCTOR OF PHILOSOPHY

| | |
|---|---|
| Chair of Committee, | Charles J. Glover |
| Committee Members, | Carl D. Laird |
| | James C. Holste |
| | Robert L. Lytton |
| Head of Department, | M. Nazmul Karim |

August 2016

Major Subject: Chemical Engineering

## ABSTRACT

Pavement oxidation modeling has been used to predict pavement aging, or more specifically, asphalt oxidation and hardening. A key aspect of such modeling is the transport of oxygen into the asphalt from pavement air voids. To improve upon previous modeling efforts, this work investigated measurement of pavement air void properties and incorporation of air void properties in pavement oxidation modeling.

A method for analyzing x-ray computed tomography (CT) images of pavement cores to determine air void properties relevant to pavement oxidation modeling, which relies on only image processing toolbox enabled MATLAB software, was developed. Method variations are applied in each of the studies presented.

In a first study, x-ray CT image analysis was applied to validate a new method for measuring total air void (TAV) variation over pavement depth. Pavement cores were cut horizontally to create slices, and TAVs were measured following techniques developed for whole cores. Because the slices are insufficient to meet standard method specimen size requirements, precision was evaluated and alternative maximum theoretical specific gravity methods were compared. A vacuum dryer increased efficiency without oxidizing the binder. Air void distributions compared favorably with x-ray CT measurements. This effort represents a step away from reliance on x-ray CT for pavement oxidation modeling.

In a second study, the assumption that only x-ray CT-identified accessible air voids (AAVs) are accessible to oxygen was examined. Analysis of nine field cores

shows TAV and AAV variation with depth to be generally similar; nevertheless, two cores had especially low AAV content in their lower slices. Oxidation in these lower slices was not correspondingly low. These results suggest that a recent diffusion depth ($d_D$) oxidation modeling approach may be improved by defining a new $d_D$ based on TAVs. Use of a TAV $d_D$ provided superior overall predictions.

In a third study, the $d_D$ approach for incorporating pavement air voids in modeling analysis was compared with another recent approach, the cylindrical approach. The two approaches were compared with a multiyear, multisite set of field data. The $d_D$ approach produced field calibration factor values that were closer to theory, and was better able to predict aging variation with pavement depth.

Based upon these studies the following future work is recommended: (1) obtain field cores from a pavement aged approximately to the point of failure and study the ability of oxidation modeling to predict the final state of the binder, (2) improve upon the current oxidation modeling approaches by incorporating an oxygen flux at the pavement surface, (3) image cores or core portions using higher resolution x-ray CT, (4) work toward a means for determining the parameters required for oxidation modeling without the need for x-ray CT, and (5) incorporate air void variation with time into oxidation modeling.

## ACKNOWLEDGEMENTS

I acknowledge my advisor Charles J. Glover. This entire work builds on concepts pioneered by Dr. Glover and his previous graduate students, and would not have been possible without the provided financial support. Dr. Glover worked directly with me and provided necessary individual instruction on countless occasions. His advanced-professor-level mastery of engineering concepts has been an inspiration and a practical support. His guidance has been logical, careful, and patient, and he has gracefully balanced the need to allow me to grow and self-direct with the need to provide appropriate direction. His consistent professionalism coupled with respectful and meaningful feedback cultivated an environment conducive to research progress. Thank you for the hours you dedicated, and for five good years.

I acknowledge my committee members Carl D. Laird, James C. Holste, and Robert L. Lytton. Each of these professors is exemplary and their contributions to my development are recognized and appreciated. I remember time spent with each of you and thank you for giving that time and sharing your insight.

I acknowledge J. Douglas White. I assisted Doug in teaching Unit Operations II for four semesters. Doug, retired from a nearly 30 year DuPont career, allowed me to work alongside him and actively developed a mentoring-style relationship. Thank you for the open interactions and the extra time you committed, which added value far beyond your responsibilities.

I acknowledge my group members Yuanchen Cui and Guanlan Liu. Thank you both for many detailed discussions regarding asphalt oxidation and graduate school obstacles generally. Thank you for your help and support.

I acknowledge Edith Arambula, a research engineer at Texas Transportation Institute. Without her organizational diligence and rare willingness to contribute when not required, this work would not have reached the same height. Thank you for so many x-ray CT images, helping me to bridge technical gaps, and providing the review of an exceptional and seasoned civil engineer.

I acknowledge Amy Epps Martin, a professor in the civil engineering department who allowed me to work under her on a project involving recycling agents. She made several important contributions to my portion of that work. Thank you for the opportunities. It was a pleasure to work under you.

I acknowledge Rick Canatella, a research technician at TTI who oversees the McNew laboratory. Rick cut cores for me, helped me locate equipment and supplies, guided me in equipment operation and supply purchasing, directed proper materials disposal, and kept my access card updated.

I acknowledge Camie Bowie, Tanner Howell, and John Wade, who served as undergraduate assistants and each made large contributions.

I acknowledge Towanna Arnold. She served as the Graduate Program Specialist during nearly my entire time here (retired just prior to my completion), and is the person I remember as my first contact. Thank you for being the reason that so many tasks that could have consumed much more time didn't. I also acknowledge Ashley Stokes who is

taking over Towanna's responsibilities and is helping me complete the final procedures required for graduation.

I acknowledge Joel James and Jeff Polasek for providing excellent IT support.

I acknowledge those who I studied or worked under prior to entering this program who provided references and letters of recommendation for entry into the program and as needed throughout the program: Oregon State University chemical engineering professor Shoichi Kimura, Lewis and Clark law school adjunct professor and intellectual property attorney John McCormack, Pope and Talbot pulp mill engineer Joe Chido, and Pope and Talbot pulp mill engineer Bob Pettit. Thank you to each of you for making particularly strong impacts on my corresponding experiences and helping me move forward.

I acknowledge my wife Karen. She moved to the area with me, found a local position as a bankruptcy attorney, and provided financial and emotional support. She joined me in over-analyzing, provided clarity, and helped me make decisions.

I acknowledge my mom. She has endlessly sacrificed to make me better and to better my circumstances, given solid direction, supported my decisions, and provided lifelong encouragement. Without her long-term effort this work would not have been of the same quality.

Finally, in the style of Michael D. Greenberg, author of *Advanced Engineering Mathematics*, a cornerstone text of my graduate experience, I acknowledge the Lord for bringing me to and through this program: "From whence cometh my help? My help cometh from the Lord, who made heaven and earth." (Psalm 121).

# NOMENCLATURE

## ABBREVIATIONS

| | |
|---|---|
| AV | Air Void |
| AAV | Accessible Air Void |
| AASHTO | American Association of State Highway and Transportation |
| ASTM | American Society for Testing and Materials |
| BSG | Bulk Specific Gravity |
| CA | Carbonyl Area |
| CAMC | Center for Asphalt and Materials Chemistry |
| C | Core |
| CI | Confidence Interval |
| CT | Computed Tomography |
| DSR | Dynamic Sheer Rheometer |
| G-R | Glover Rowe |
| GUI | Graphical User Interface |
| FTIR | Fourier Transform Infrared |
| HS | Hardening Susceptibility |
| HMA | Hot Mix Asphalt |
| LSV | Low Sheer Rate Limiting Complex Dynamic Viscosity |
| MTSG | Maximum Theoretical Specific Gravity |
| NFB | No Flux Boundary |

| | |
|---|---|
| PAV | Pressure Aging Vessel |
| PG | Performance Grade |
| POV | Pressure Oxidation Vessel |
| QA | Quality Assurance |
| QC | Quality Control |
| RTFO | Rolling Thin Film Oven |
| S | Slice |
| SS | Slice Specific |
| TAV | Total Air Void |
| TxDOT | Texas Department of Transportation |
| VS | Vacuum Sealing |
| WC | Whole Core |
| WMA | Warm Mix Asphalt |
| YNP | Yellowstone National Park |
| 2D | Two Dimensional |
| 3D | Three Dimensional |

**SYMBOLS**

| | |
|---|---|
| $\alpha$ | Oxygen Reaction Order |
| $A$ | Viscosity HS relation pre-exponential factor (i.e. $e^{m_{LSV}}$) |
| $A´$ | DSR Function HS relation pre-exponential factor (i.e. $e^{m_{DSR\ function}}$) |
| $A_c$ | Constant-Rate Pre-exponential Factor |
| $A_f$ | Fast-Rate Pre-exponential Factor |
| $c$ | Converts Oxygen Consumed to Carbonyl Produced |
| $d_D$ | Diffusion Depth |
| $d_{D\_AAV}$ | Accessible Air Void Diffusion Depth |
| $d_{D\_TAV}$ | TAV Air Void Diffusion Depth |
| $D_e$ | Effective Diffusivity |
| $D_{O_2}$ | Diffusivity of Oxygen in Asphalt |
| $\delta$ | Angle between Storage Modulus and Loss Modulus |
| $E_{ac}$ | Constant-Rate Activation Energy |
| $E_{af}$ | Fast-Rate Activation Energy |
| $\varepsilon$ | Asphalt Volume Fraction |
| fcf | Field Calibration Factor |
| $G^*$ | Complex Dynamic Modulus |
| $G´$ | Storage Modulus (Real Component of Complex Dynamic Modulus) |
| $G´´$ | Loss Modulus (Imaginary Component of Complex Dynamic Modulus) |

| | |
|---|---|
| $G_b$ | Asphalt Specific Gravity |
| $G_{mm}$ | Maximum Theoretical Specific Gravity |
| $h$ | Solubility Constant for Oxygen in Asphalt |
| $k_c$ | Constant-Rate CA Reaction Constant |
| $k_f$ | Fast-Rate CA Reaction Constant |
| $m_{\text{LSV}}$ | Intercept on Plot of ln(LSV) vs CA |
| $m_{\text{DSR Function}}$ | Intercept on Plot of ln(DSR Function) vs CA |
| $M$ | Maximum Increase in CA Due to Fast Rate Reaction |
| $N_{O_2}$ | Oxygen Flux |
| $\eta_0^*$ | Low Sheer Rate Limiting Complex Dynamic Viscosity |
| $\eta'$ | Real Component of Complex Dynamic Viscosity |
| $O_2$ | Oxygen |
| $\sigma$ | Standard Deviation |
| $P$ | Pressure |
| $P_b$ | Asphalt Content |
| $T$ | Temperature |
| $\tau$ | Tortuosity |

## TABLE OF CONTENTS

Page

## LIST OF FIGURES

Page

## LIST OF TABLES

Page

# CHAPTER I

# INTRODUCTION

## INTRODUCTION

Asphalt pavement, used in road construction, is a flexible material comprising asphalt (aka binder or asphalt binder), aggregate, and air voids. Asphalt binds the aggregate pieces together and imparts flexibility to the pavement. If the asphalt is too soft traffic loading can cause pavement rutting, if the asphalt is too hard traffic and temperature loading can cause cracking.

Asphalt oxidation is a relentless process that ages asphalt and thereby defines the useful life of a pavement. In this work, asphalt aging refers generally to asphalt oxidation and the resultant rheological hardening. Asphalt oxidation is the process of oxygen, from the air, reacting with asphalt and becoming incorporated therein. Oxidation occurs throughout the depth of pavement (Al-Azri et al., 2006). Initially the relatively soft asphalt must be just hard enough to prevent rutting and then, inevitably, after enough aging the asphalt will become too hard and pavement cracking will begin.

When selecting asphalt for inclusion in paving mix field testing is time prohibitive; alternative methods for evaluating asphalts have been developed. An asphalt pavement's lifespan can be 10 years or more, therefore it is impractical to build and evaluate test sections to evaluate proposed binders. To overcome this, one common binder evaluation methodology, SuperPave performance grading, calls for accelerated aging in a pressure aging vessel (PAV) (Asphalt Institute, 1994). Aging is accelerated

using elevated temperature and pressure. The aged binder must meet specific softness-related criteria.

This method of binder evaluation, while widely utilized, assumes that binder properties after accelerated aging correlate well with binder properties after field aging. PAV aging is at a pressure significantly higher than atmospheric (20.7 gauge) and it is not clear that aging rates at pressures other than atmospheric correlate well with aging rates at atmospheric pressure (Domke, 1999). PAV aging does not account for location-specific climatic conditions, which affect pavement temperature and hence binder aging rate. Furthermore, PAV aging does not account for pavement air void variation, which affects oxygen accessibility to the asphalt within the pavement.

A complete method for predicting binder aging in pavement at field locations would be immediately applicable to pavement construction and maintenance activities. Such a model would provide a superior method of pavement-construction binder evaluation. Additionally, accurate prediction of in-field, binder properties could provide a route to predicting changing pavement properties. Improved time-to-pavement-failure estimation would improve life-cycle-cost estimations. Along the same lines, pavement maintenance timing and costs could be more accurately accounted for.

## OXIDATION MODELING

The Center for Asphalt and Materials Chemistry (CAMC) in the chemical engineering department at Texas A&M University has developed an asphalt binder aging model that is intended to predict in-field binder aging (Lunsford, 1994; Prapaitrakul et al., 2009;

Prapaitrakul, 2009; Han, 2011; Jin et al., 2013). As mentioned above, in this dissertation, the term aging refers generally to binder oxidation and the resultant hardening of the binder. Within this context, binder aging is quantified primarily in terms of FTIR measured carbonyl area (CA), a surrogate measurement for binder oxidation (Jemison et al., 1992; Lin et al., 1995; Liu et al., 1996; Liu et al., 1998), and the DSR function, a rheological parameter (Ruan et al., 2003; Juristyarini et al., 2011a; Juristyarini et al., 2011b). The following material overviews the asphalt binder aging model developed by the CAMC and relevant literature.

Figure 1 presents the major components of the asphalt aging model developed by the CAMC in the context of a system of graphical user interfaces (GUIs) developed as part of a recent Texas Department of Transportation (TxDOT) project (Glover et al., 2014a, Ch. 16). As shown in Figure 1, a primary objective of the model is the prediction of CA increase with time. To this end, the following inputs are required: asphalt-specific reaction kinetics parameters from experimental aging data, a location-specific pavement temperature profile, and an oxygen diffusion path length. Determination of the oxygen diffusion path length is discussed extensively in this dissertation. The remainder of this section describes the model in more detail.

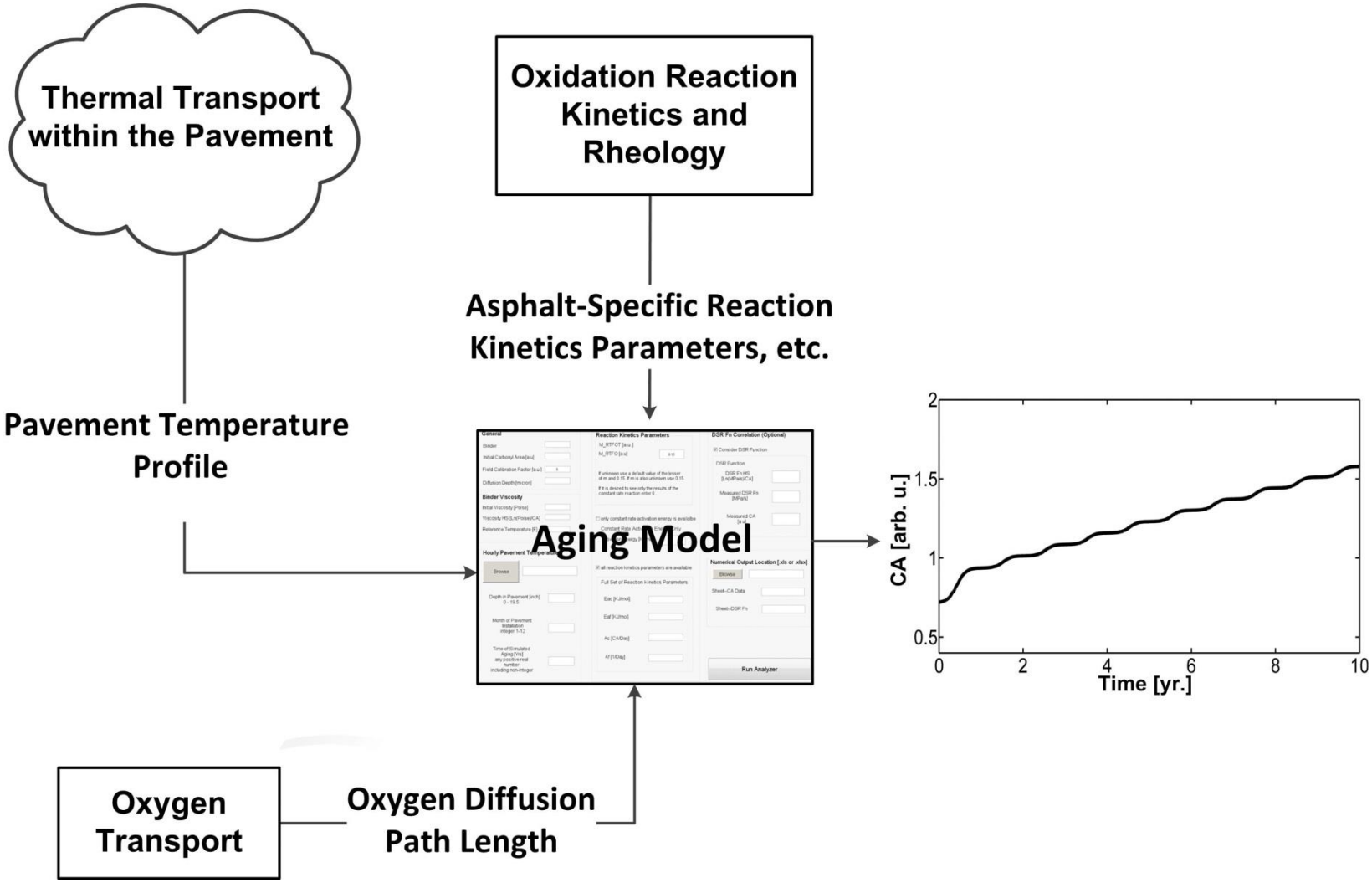


FIGURE 1 Asphalt binder aging modeling approach.

Figure 2 presents the aging model conceptually. Oxygen transport within the air voids is assumed sufficiently fast to permit the assumption that the oxygen partial pressure within the accessible air voids (AAVs) is the same as the oxygen partial pressure in the air (Prapaitrakul et al., 2009; Jin et al., 2013). From the AAVs oxygen diffuses horizontally into the asphalt and reacts with the asphalt to produce carbonyl.

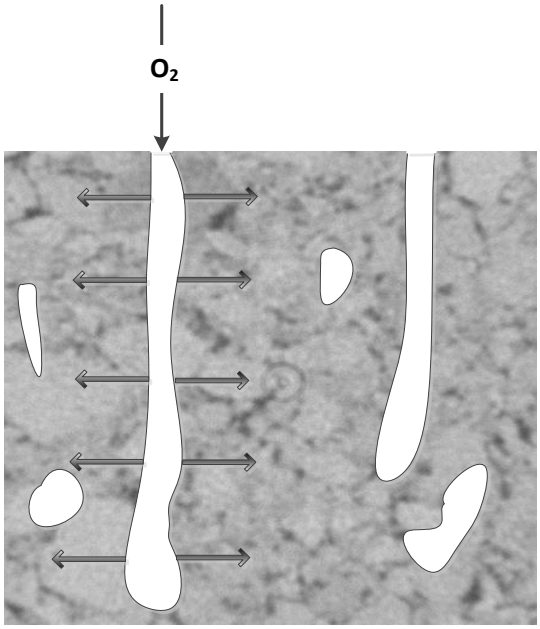


FIGURE 2 Conceptual aging model.

Figure 3 details, conceptually, the oxygen concentration as a function of distance from an air void interface. At the air void interface the asphalt is assumed saturated with oxygen. At some distance from the air void interface it is assumed that there is no longer a flux of oxygen (additional discussion below). The oxygen diffusion path length is the distance between these two boundaries. Between these two boundaries (i.e. along the

oxygen diffusion path) the oxygen concentration decreases as a result of reaction with the asphalt. Lower oxygen concentrations, further from the interface, in turn result in slower CA production rates.

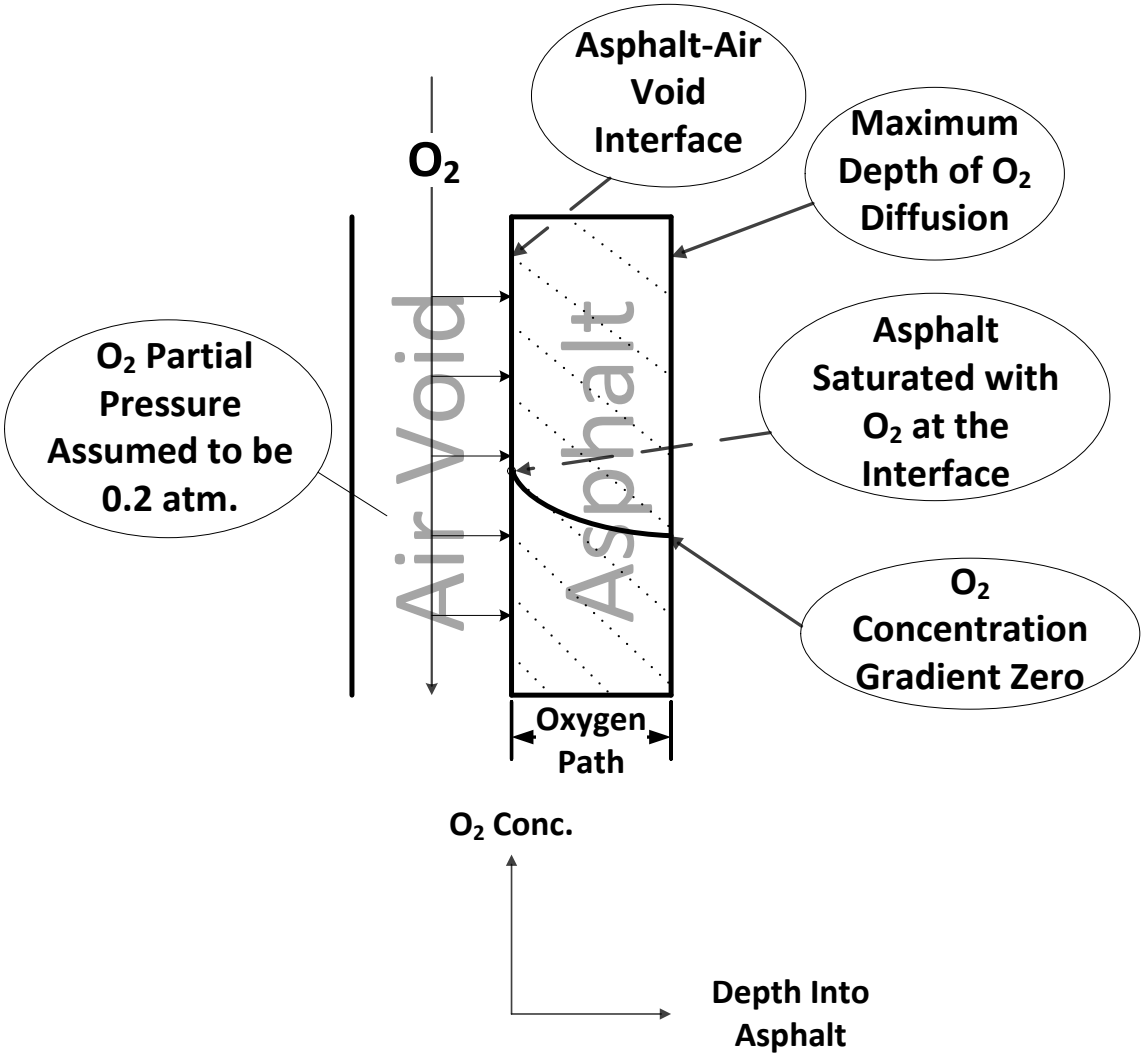


FIGURE 3 Oxygen concentration profile.

Two modeling approaches have been developed to mathematically approximate the physical phenomena described—a cylindrical approach (Prapaitrakul et al., 2009;

Han, 2011) and a diffusion depth ($d_D$) approach (Jin et al., 2013). Each of these approaches relies on specific pavement air void properties. The approaches and the corresponding air void properties are described here. Specific methods of estimating the air void properties, by taking and analyzing x-ray CT images, are described in the next chapter.

A depiction of the cylindrical approach, in the context of a top view of a pavement core, is shown in Figure 4. The air voids are modeled as tall, skinny, vertical cylinders from which oxygen diffuses radially into the surrounding asphalt-aggregate matrix. Each air void cylinder is envisioned as surrounded concentrically by a larger no-flux-boundary (NFB) cylinder. The air voids are assumed equally spaced and the matrix material homogeneous. The aging state of the binder between an air void and its corresponding NFB is assumed representative of the aging state of the binder throughout the pavement (at the same vertical pavement depth). Estimation of air void and NFB sizes is described in the next chapter and throughout this dissertation.

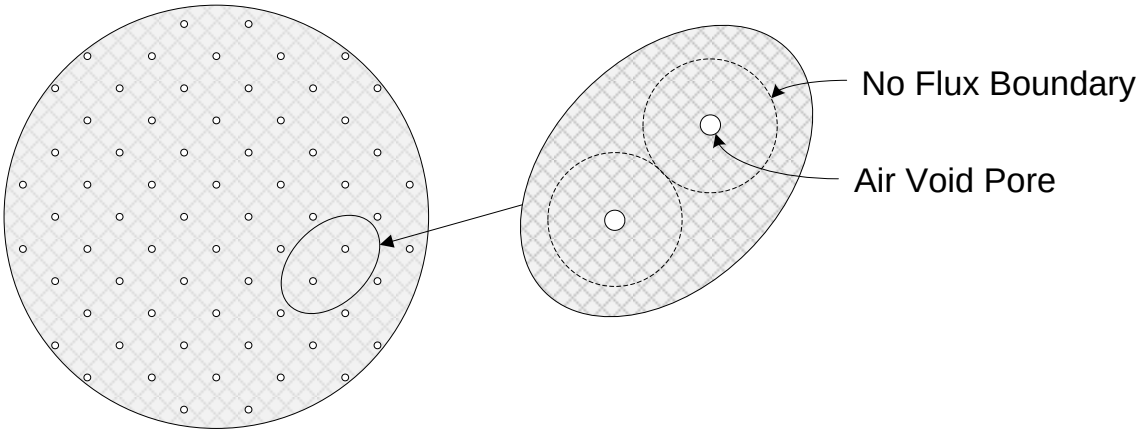


FIGURE 4 Air voids concept in cylindrical approach to oxidation modeling (top view).

The, more recent, $d_D$ approach is somewhat more abstract and is essentially depicted by Figure 3 above. In the $d_D$ approach the air voids are envisioned as being coated by a layer of asphalt. The thickness of this layer is termed the $d_D$ and is calculated as the volume of asphalt in the pavement divided by the surface area of the AAVs. The concept is analogous to that of asphalt film thickness (i.e. the average depth of a theoretical asphalt film coating the aggregate, calculated as asphalt volume divided by aggregate surface area), but rather than coating the aggregates the asphalt is envisioned to coat the air voids. In the $d_D$ approach, rectangular coordinates are imposed, and the oxygen is modeled as diffusing, horizontally, from the air void-asphalt interface into the asphalt out to the $d_D$, which is the no flux boundary. Beyond coordinate systems, the $d_D$ approach is distinguishable from the cylindrical approach in that it is based on asphalt volume alone, while the cylindrical approach considers the entire asphalt-aggregate volume.

Fundamentally oxidation modeling is based on the simultaneous solution of an unsteady-state oxygen continuity equation coupled with a reaction kinetics equation. Furthermore, thermal transport within the pavement must be modeled to determine pavement temperature as a function of time and depth. The continuity equation describes the oxygen concentration profile in the asphalt (as shown in Figure 3). The reaction kinetics equation describes the rate of CA growth as a function of oxygen concentration, pavement temperature, and reaction kinetics parameters. Solution of the coupled equations provides CA as a function of time and distance from the air void. In this work, as done previously, CA is averaged over the oxygen path length and this average value is

the reported CA. Depth-specific CA predictions can be made by supplying depth-specific pavement temperatures and depth-specific oxygen path lengths.

As touched on above, the oxidation modeling approaches assume that the aging state of the binder between an air void and its corresponding no flux boundary is representative of the aging state of the binder at the modeled pavement depth. In effect, each asphalt mixture is modeled as a continuum (i.e. representative aggregate, air void, and asphalt properties replace the properties of the numerous individual components within the mixture). Following this approach, the CA growth in the asphalt, at a given pavement depth, surrounding a single representative air void, can be assumed representative of the CA growth at that pavement depth.

The continuity and reaction kinetics equations are overviewed. Additional model details are provided by Jin et al. (2013).

By generalizing slightly the specific oxygen continuity equations used in the cylindrical (Prapaitrakul et al., 2009; Han, 2011) and $d_D$ (Jin et al., 2013) approaches can be described by a single equation:

$$\frac{\partial P(x,t)}{\partial t} = x^{-m} \cdot \frac{\partial}{\partial x}\left(x^m \cdot \text{fcf} \cdot D_{O_2} \cdot \frac{\partial P(x,t)}{\partial x}\right) - \frac{c}{h} \cdot \frac{\partial \text{CA}(x,t)}{\partial t} \quad (1)$$

where $m$ is 0 for rectangular coordinates and 1 for cylindrical coordinates, $P$ represents (indirectly) oxygen concentration in the asphalt, $t$ represents time, $x$ represents distance from the air void, $D_{O_2}$ is the diffusivity of oxygen in asphalt, fcf is a field calibration

factor, *c* is a factor that converts oxygen consumed to carbonyl produced (Liu et al., 1998), and *h* is the solubility constant of oxygen in asphalt (Dickinson, 1984).

Additional description of this generalized equation aids understanding and application. For the $d_D$ approach (rectangular coordinates) *x* represents distance in the x direction (horizontal) away from the air void-asphalt interface. For the cylindrical approach *x* represents distance in the radial direction (also horizontal) away from the air void-matrix interface. Carbonyl area and *P* relate to an asphalt volume basis for both the cylindrical and $d_D$ approaches. For the $d_D$ approach this result is immediate. For the cylindrical approach the natural volume basis is that of the asphalt-aggregate matrix and this basis must be converted to an asphalt-volume basis.

Conversion to an asphalt-volume basis requires use of an expression for effective diffusivity through the asphalt-aggregate matrix (i.e. porous media) in the oxygen continuity equation, followed by division of the resulting equation by the asphalt volume fraction, $\varepsilon$, in the matrix. The oxygen flux can be expressed using an effective diffusivity (Geankoplis, 1993, Ch. 6):

$$N_{O_2} = -\frac{\epsilon}{\tau} \cdot D_{O_2} \cdot \frac{\partial C_{O_2}}{\partial r} \hat{r} \tag{2}$$

where $C_{O_2}$ is oxygen concentration per volume of asphalt (rather than per volume of asphalt-aggregate matrix), $D_{O_2}$ is the diffusivity of oxygen in asphalt (rather than in the asphalt-aggregate matrix), and $\tau$ is the tortuosity of the oxygen path through the

asphalt-aggregate matrix. After inserting the effective diffusivity expression, the entire continuity equation is divided by the asphalt volume fraction, which converts the remaining terms to an asphalt basis (from the original asphalt-matrix basis) and cancels the volume fraction from the effective diffusivity expression. The remaining $1/\tau$ in front of the diffusivity is absorbed into the fcf and can be thought of as providing an ideal value for the fcf.

Solution of the continuity equation requires two boundary conditions and an initial condition (and, of course, the coupled reaction kinetics equation). The following boundary and initial conditions are applied in both modeling approaches.

Initial Condition: No Oxygen in Binder (3)

Boundary Condition 1: Binder at Binder-Air Void Interface Saturated with Oxygen (4)

Boundary Condition 2: No Oxygen Flux at No Flux Boundary (5)

Asphalt oxidation can be described in terms of a fast-rate reaction and a constant-rate reaction (Jin et al., 2011). The fast-rate reaction is limited in extent and plays a more significant role earlier in pavement life. The constant-rate reaction, on the other hand, continues unabated throughout the life of the pavement. The following reaction kinetics equations, and the corresponding initial condition, are provided by Jin et al. (2013).

$$\frac{\partial \mathrm{CA}}{\partial t} = M_{\mathrm{RTFO}} \cdot k_f \cdot e^{-k_f t} + k_c \quad (6)$$

$$k_f = A_f \cdot P^{\alpha} \cdot e^{\frac{-E_{af}}{R \cdot T}} \quad (7)$$

$$k_c = A_c \cdot P^{\alpha} \cdot e^{\frac{-E_{ac}}{R \cdot T}} \quad (8)$$

Initial Condition: CA equal to $\mathrm{CA}_{\mathrm{RTFO}}$ (9)

where $E_{ac}$ is the constant-rate activation energy, $A_c$ is the constant-rate pre-exponential factor, $E_{af}$ is the fast-rate activation energy, $A_f$ is the fast-rate pre-exponential factor, $M_{\mathrm{RTFO}}$ is the maximum CA growth due to the fast-rate reaction, and $\alpha$ is the reaction order with respect to oxygen. The first term on the right hand side (RHS) of Equation 6 describes the CA growth due to the fast-rate reaction; the second term describes the CA growth due to the constant-rate reaction.

In an earlier work Jin et al. (2011) describe a method for determining the reaction kinetics parameters. Thin films of asphalt are aged in pressure oxidation vessels set to different temperatures. The films are removed according to an aging schedule, and the aged films are FTIR tested to determine CA. The reaction kinetics model described by Jin et al. (2011) is fit to the data by adjusting the reaction kinetics parameters.

As part of the same work Jin et al. (2011) found that all of the reaction kinetics parameters, except $M_{\mathrm{RTFO}}$, are correlated to the constant-rate activation energy.

As mentioned above, solution of the coupled oxygen continuity and reaction kinetics equations requires pavement temperature inputs. Han et al. (2011) provide a method for determining a location-specific pavement temperature profile. The method

uses publicly available weather data and location optimized parameters in a heat transfer model. A generated pavement temperature profile provides hourly temperature values that are specific to time of year and pavement depth.

## LINKING CA WITH BINDER RHEOLOGY AND PAVEMENT PERFORMANCE

Although the above discussion focuses on CA, prediction of CA variation with time requires the simultaneous prediction of viscosity variation with time, and furthermore, simultaneous prediction of the DSR function, which provides a route to pavement-failure prediction, is also possible after establishing the binder-specific relationship between CA and DSR function. Binder viscosity must be predicted simultaneously with CA because the diffusivity of oxygen in binder is a function of binder viscosity (Han et al., 2011).

Lau et al. (1992) showed that the natural log of the low sheer rate limiting complex dynamic viscosity (LSV) is linearly related to CA. The slope is termed the viscosity hardening susceptibility (HS).

$$\eta_0^* = e^{m_{\mathrm{LSV}}} \cdot e^{\text{viscosity HS}\cdot\mathrm{CA}} \tag{10}$$

where $\eta_0^*$ is the LSV, and $m_{\mathrm{LSV}}$ is the intercept on a plot of ln(LSV) vs CA.

Conveniently, the relationship identified between CA and LSV has also been found to apply to the DSR function. The slope is termed the DSR function HS.

$$\text{DSR function} = e^{m_{\text{DSR function}}} \cdot e^{\text{DSR function HS}\cdot\text{CA}} \quad (11)$$

where $m_{\text{DSR function}}$ is the intercept on a plot of ln(DSR Function) vs CA. The DSR function is a rheological property of binder that includes both viscous and elastic terms, and that correlates with ductility (Ruan et al., 2003). Ductility, in turn, has been related to pavement failure (Clark, 1958; Doyle 1958). More recently the relationship between the DSR function and pavement durability has been investigated (Anderson et al., 2011; King et al., 2012).

The DSR function is defined as $G'/(\eta'/G')$ measured using a dynamic sheer rheometer at 15 °C and 0.005 rad/s. Alternatively, the measurement may be made at 44.7 °C and 10 rad/s and the resulting function value shifted to the defined conditions by dividing by the frequency ratio (10/0.005) ($G'$ and $G''$ measured at 44.7 °C and 10 rad/s have been shown to be nearly equivalent to $G'$ and $G''$ measured at 15 °C and 0.005 rad/s, using the time-temperature superposition principle and assuming an average time-temperature shift factor (Ruan et al. (2003); Juristyarini et al. (2011a)), also $\eta'$[Pa·s]=$G''$[Pa]/$\omega$[1/s], therefore the ratio of $G'/(\eta'/G')$ at 15 °C and 0.005 rad/s to the same function at 44.7 °C and 10 rad/s reduces to a ratio of the two frequencies).

Recently, the DSR function has been recast into a different form and the recast form has been named the Glover-Rowe (G-R) parameter (King et al., 2012; Rowe, 2011; Rowe et al., 2014). Rowe (2011), using the fact that the frequency is constant, recast the DSR function as $G^*(\cos^2\delta/\sin\delta)$, which is numerically equal to the DSR function divided by the frequency. This form is intended to appear more familiar, being

somewhat analogous to the SuperPave fatigue cracking parameter (i.e. $G^* \sin \delta$). As indicated, conversion between DSR function values and G-R parameter values simply involves multiplication by a constant, for example, to convert DSR function values reported in MPa/s to G-R parameter values in kPa multiply by $2 \cdot 10^5$.

As mentioned above, DSR function prediction provides a route to pavement failure prediction. The DSR function is correlated to ductility and ductility, in turn, has been found to be correlated with pavement performance. Specifically, experimental results summarized by Kandhal (1977) indicated cracking failure was present when ductility (measured at approximately 15 °C, 1 cm/min) fell to approximately of 3–5 cm, and similarly Halstead (1963) reported raveling when ductility fell to 3 cm. Ruan et al. (2003) identified a correlation between DSR function, measured at 15 °C and 0.005 rad/s and ductility, measured at 15 °C, and 1 cm/min, for unmodified binders:

$$\text{Ductility [cm]} = 0.23 \cdot \text{DSR function} \left[\frac{\text{MPa}}{\text{s}}\right]^{-0.44} \tag{12}$$

Using the correlation and concepts of Ruan et al. (2003), Juristyarini et al. (2011b) defined an explicit "failure point" for the DSR function of $3 \cdot 10^{-3}$ MPa/s, which corresponds to a 3 cm ductility. Anderson et al. (2011) said a 5 cm ductility (DSR function value of $9 \cdot 10^{-4}$) corresponds to the "approaching point where cracking will occur," and a 3 cm ductility corresponds to a pavement that "will exhibit cracking." Rowe et al. (2014) lists a G-R parameter value of 180 kPa (ductility 5 cm; DSR function

$9 \cdot 10^{-4}$ MPa/s) as a "damage onset" value and a G-R parameter value of 450 kPa (ductility 3.4 cm; DSR function $2.2 \cdot 10^{-3}$ MPa/s) as a "significant cracking" value.

The correlation between DSR function and ductility may be shifted for polymer modified binders (Woo et al., 2007, Ch. 3).

## ASPHALT AND ASPHALT OXIDATION CHEMISTRY

For asphalt oxidation modeling, the relationships, described above, between CA and rheological properties are essential; background on asphalt chemistry and the effects of oxidation provides context.

Asphalt is the heaviest component resulting from crude oil distillation and comprises primarily heavy hydrocarbons (saturated chains and rings as well as aromatic rings). Asphalt is commonly divided into four fractions (asphaltenes, naphthene aromatics, polar aromatics, and saturates) by Corbett fractionation (ASTM D4121). Other similar division schemes are not uncommon (Boduszynski, 1981). In addition to carbon and hydrogen, asphalt contains oxygen, nitrogen, and sulfur, which are referred to individually as heteroatoms (Roberts et al., 1996). Corbett fractionation divides asphalts into asphaltenes and maltenes, and further divides maltenes into saturates, naphthene aromatics, and polar aromatics. Asphaltenes are highly polar groups of aromatic rings, polar aromatics are similar but somewhat less polar and show less tendency to associate, napthene aromatics are systems of aromatic and nonaromatic rings and are less polar yet, and saturates, being saturated hydrocarbon chains and rings, are

the least polar (Roberts et al., 1996). All of the fractions have similar molecular weights, averaging around 1000, with an approximate range of 200–1800 (Boduszynski, 1981).

Corbett fractions are defined by a process that sorts primarily based on polarity. Asphaltenes comprise the fraction that does not dissolve in n-heptane (i.e. a non-polar solvent). Heptane-dissolved maltenes are poured through an alumina column. Saturates, which have the lowest polarity, wash through with the heptane. Nathphene aromatics and polar aromatics, which are more polar than saturates but less polar than asphaltenes, adsorb on the alumina. Solvents of increasing polarity are used to separate the napthene aromatics and polar aromatics from the alumina.

In an alternative component division asphalt is again characterized as comprising asphaltenes and maltenes, but the maltenes are divided into resins, and oils; the alternative components can be related roughly to the Corbett fractions, and provide a basis for characterizing asphalt as a colloidal system (Roberts et al., 1996). Resins correlate roughly with polar aromatics, and oils correlate with naphthene aromatics and saturates (aka parrafins). The asphaltenes act as colloidal particles that are dispersed in the oily phase by the resins (Roberts et al., 1996).

Asphalt oxidation produces additional asphaltenes, which act as solid particles dispersed in the asphalt in that they increase the asphalt viscosity. Asphalt oxidation converts naphthene aromatics to polar aromatics, and polar aromatics to asphaltenes (saturates are not affected by oxidation) (Lin et al., 1995). Protective action by the polar aromatics is thought to limit further oxidation of the asphaltenes (Lin et al., 1995). Lin

et. al. (1995) describe the relationship between percent asphaltenes and asphalt viscosity using a modified Pal-Rhodes model.

Lin et al. (1995) also provide insight into the relationship between oxidation and CA. The term carbonyl is used generally to describe a C = O group, and, as mentioned above, the concentration of these groups can be quantified in terms of CA using FTIR. Lin et al. (1995) showed that oxidation is linearly correlated with CA and surmised that the formation rates of all oxygen-containing groups must, therefore, be in nearly constant ratio with each other. Lin et al. (1995) concluded that CA could be used as a surrogate for oxidation.

## FIELD DATA

Ultimately, oxidation modeling is intended to predict properties of pavement or binder aged in the field. Field data obtained using proven techniques serve as a standard and are used to validate new techniques and modeling predictions. Discrepancies provide guidance.

Figure 5 shows a pavement core and pavement core slices. Pavement cores are cylindrical pieces of the pavement that are cut from the pavement for study. The cores can be taken anytime during the life of the pavement, from construction onward. Taking cores over the life of the pavement is particularly useful for research purposes because it allows for monitoring of pavement property evolution with time. In this work, cores are generally 150 mm in diameter and have heights corresponding the thickness of the

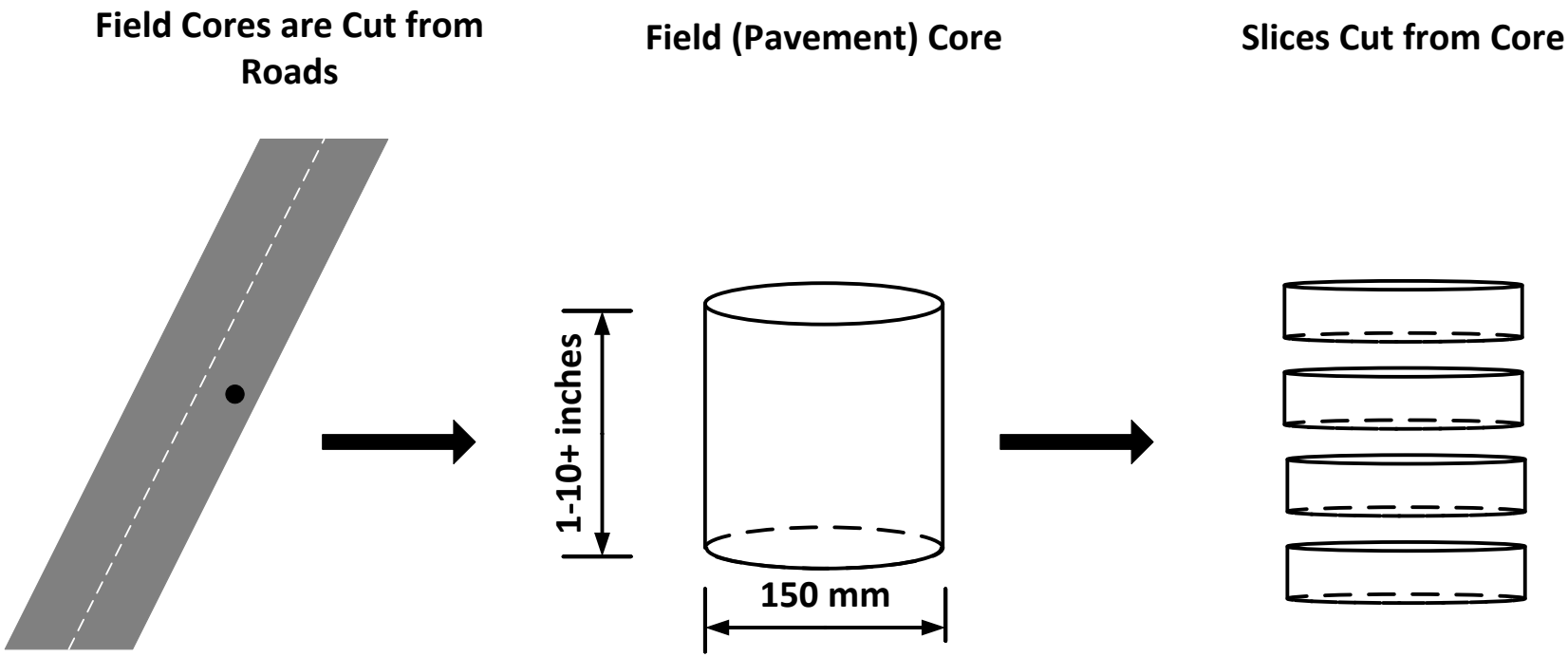


FIGURE 5 Obtaining field core and core slices.

pavement lift (a height of paving mix laid down at a single time, approximately 38–76 mm (1.5–3 inches) in this work). Cores can be taller and can extend through multiple pavement lifts. To study variation with depth, cores are cut horizontally at 12.7 mm (0.5 inch) intervals to create slices.

A multitude of tests are available for evaluating properties of paving mix and the individual components (i.e. asphalt and aggregate) (Roberts et al., 1996). Selected evaluation techniques that are particularly relevant to this work are overviewed here; additional description is provided throughout this dissertation.

Whole core testing includes total air void (TAV) volume fraction measurement and x-ray CT imaging. Although described as a TAV measurement, the property measured is typically the bulk specific gravity (BSG). To calculate the TAV volume fraction, the maximum theoretical specific gravity (MTSG) (i.e. the specific gravity of the material excluding air voids) is also required and standard method measurement techniques call for loose mix (i.e. pavement mix obtained before compaction into a pavement lift). Oftentimes, after construction, loose mix is no longer available, and alternative MTSG values must be obtained from mix design specifications or QA/QC results. In addition to TAV measurements, whole cores are scanned using x-ray CT and the resulting images are analyzed to determine air void properties (discussed next chapter).

As for whole cores, core slices are tested for air void properties, and afterward the binder can be extracted and tested. In addition to BSG measurements, it is also possible to make MTSG measurements on the slices because after TAV measurements

the material can be broken apart into a gravel-like loose mix alternative. Afterward, the binder can be extracted from the gravel-like material using solvent and recovered by evaporation of the solvent (Burr et al., 1990; Burr et al., 1991; Cipione et al., 1991; Burr et al., 1993; Burr et al., 1994; Cui et al., 2015). The recovered binder can be tested for FTIR CA, and for rheological properties including LSV and the DSR function.

As a final note, binder properties immediately after construction are often needed as a starting point for oxidation modeling, and because construction cores are not always available, rolling thin film oven (RTFO) aging is used to approximate the binder aging that occurs during construction (ASTM D2872). Rolling thin film oven aging involves subjecting thin films of binder to elevated temperature (163 °C (325 °F)) for 75 minutes. Afterward, binder properties may be tested and results used to approximate binder properties immediately after construction.

## OBJECTIVES

The pavement oxidation modeling efforts described above have laid out a fundamentals-based approach for predicting pavement property changes in the field over time, and in defining this framework have, at the same time, provided guidance regarding promising focus areas for modeling improvement. As described above, these fundamentals based approaches incorporate asphalt-specific reaction kinetics, location-specific pavement temperature, and other binder and pavement properties into a coupled set of equations that govern the oxygen transport and carbonyl production phenomena. Reviewing this previous work, it is apparent that understanding pavement

air void properties and how these properties influence pavement aging is relevant to accurate oxidation modeling.

The research reported herein focuses on pavement air void property determination and on identifying the best approaches for incorporating air void properties in oxidation modeling. Guided by previous work, areas for study and potential improvement are identified. Specific findings are presented in a manner that is intended to be immediately applicable. Finally, guidance is provided for continuing toward a more complete understanding of the relationship between air voids and pavement oxidation, and simpler implementation.

This work addressed four specific objectives:

1. Develop an x-ray CT image processing method for determining field core air void properties necessary for pavement oxidation modeling. The method should be sufficiently flexible to permit determination of slice-average volume fractions for comparison with volumetric data.

2. Develop a method for measuring TAV variation with pavement depth and validate the method by comparison with x-ray CT image analysis results using the tool developed in objective 1. As part of this objective, determine whether a vacuum dryer can be used to increase efficiency without oxidizing the binder to the extent that it cannot be used for additional testing.

3. Compare the use of x-ray CT identified accessible air voids (AAVs) with x-ray CT identified TAVs for predicting oxidation variation with pavement

depth. Make this comparison in the context of the $d_D$ pavement oxidation modeling approach.

4. Compare the cylindrical and $d_D$ approaches to oxidation modeling with a multiyear, multisite set of field core data to determine if either approach is preferred and to gain insight for future modeling improvement.

Additionally, this work addressed one broad objective: improve the current understanding of pavement air void properties, their measurement, and the relationship between air void properties and pavement aging. To accomplish this objective: study air void property variation with pavement depth and pavement aging variation with both pavement depth and time, focusing on recent pavement oxidation modeling approaches; include comparisons with field data and use field data to guide conclusions; identify overall trends, and suggest improved and simplified methods of incorporating air void properties in pavement oxidation modeling.

## DISSERTATION OUTLINE

The outline of this dissertation follows from the presented objectives. Chapter II describes a method that uses image process toolbox enabled MATLAB software to analyze raw x-ray CT images to determine air void properties needed for pavement oxidation modeling. Chapter III presents a method for measuring air void volume fraction variation with pavement depth, validates the method by comparison with results from x-ray CT image analysis, and shows that a vacuum dryer may be used to increase efficiency. Chapter IV defines a new $d_D$ based on TAVs and shows that oxidation

modeling using the newly defined $d_D$ produces better overall predictions than the previously defined $d_D$ based on AAVs. The work indicates that nearly all pavement air voids may be accessible to oxygen. Chapter V compares the cylindrical and $d_D$ approaches for incorporating air void information in oxidation modeling. Recent improvements are included in both approaches. It is concluded that the $d_D$ approach is better able to predict aging variation with pavement depth and provides more reasonable diffusion path lengths. Chapter VI summarizes the major conclusions of this work and provides guidance for future work.

# CHAPTER II

# PAVEMENT CORE X-RAY CT IMAGE ANALYSIS FOR OXIDATION MODELING

## INTRODUCTION

As described in Chapter I, recent oxidation modeling requires air void properties obtained from x-ray CT images of pavement cores. This chapter describes a method of analysis using image processing toolbox enabled MATLAB software, which method is applied in the following chapters of this dissertation. The method described here builds on previous work (Masad et al., 1999; Masad et al., 2002; Arambula et al., 2007; Prapaitrakul et al., 2009; Han, 2011; Jin et al., 2013). Prior to introducing the imaging and analysis techniques a brief description of pavement air void terminology is provided.

Pavement core air voids can be divided into four categories: total air voids (TAVs), accessible air voids (AAVs), inaccessible air voids, and interconnected air voids. Volumetric techniques and x-ray CT imaging have been used to better understand these categories and the relationships between them. Figure 6 provides visual definitions of the four air void categories.

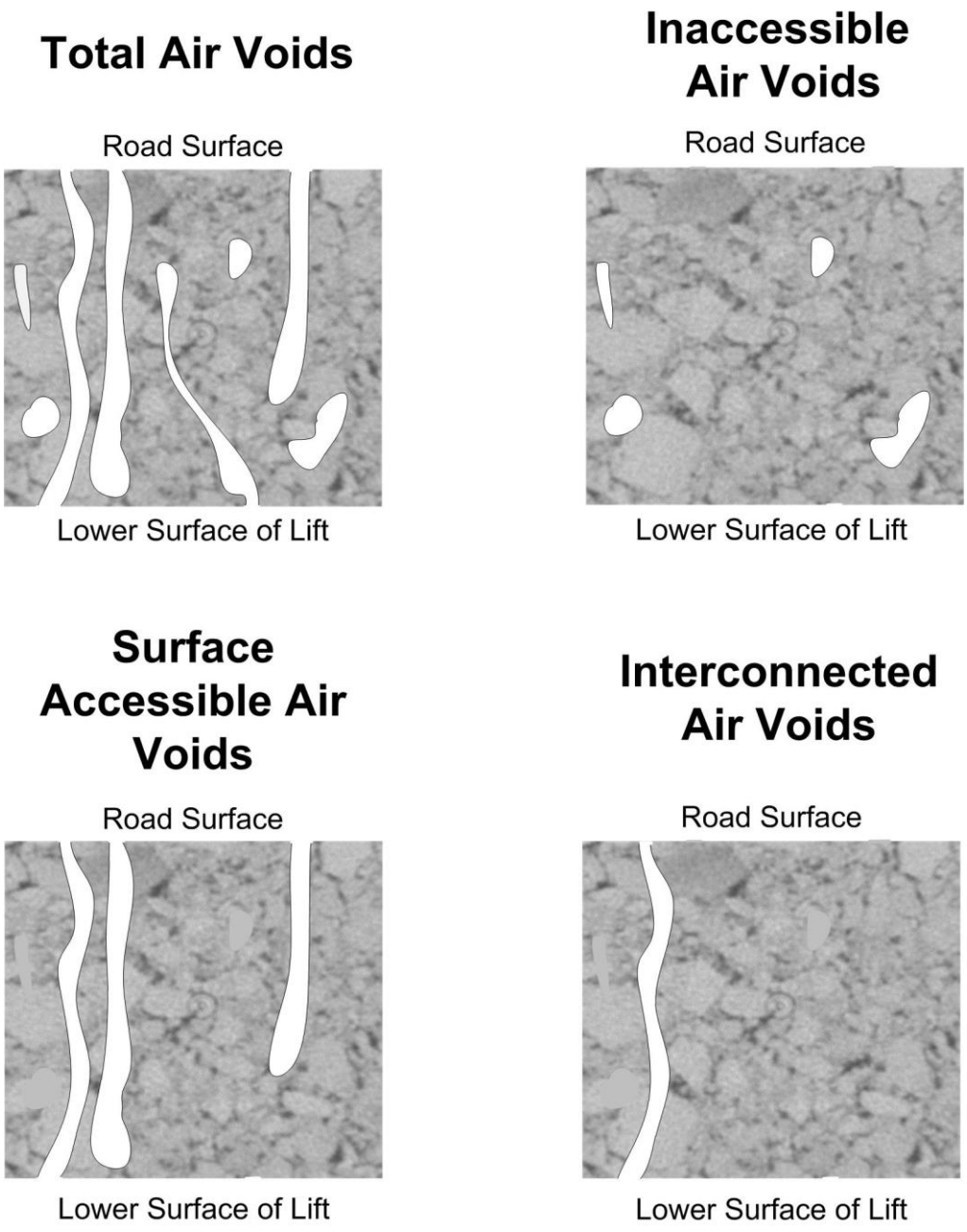


FIGURE 6 Pavement air void categorization.

Although these visual definitions appear straightforward, a brief discussion of the term accessible may help avoid confusion. The term accessible can be understood to

mean accessible to a specific material (e.g. oxygen) from a specific surface (e.g. a surface where the material of interest is present). Common volumetric techniques for measuring AAVs relate to water accessibility from the exposed surfaces of the specimen being tested, which surfaces may not correspond to the original exposed surfaces (ASTM D7063; AASHTO T166). For example, a pavement core has exposed upper, lower, and side surfaces, yet while in service possibly only the upper surface should be considered exposed. Related, some previous work has focused on the ability of water to pass completely through a pavement lift, and has therefore been concerned with voids (termed interconnected air voids) that extend from the upper surface to the bottom surface of a lift and allow for water passage through the lift (Arambula et al., 2007; Glover et al., 2104a, Ch. 13). Oxidation modeling, on the other hand, focuses on the ability of oxygen to enter, rather than pass through, the pavement lift.

X-ray CT scans can be used to compliment volumetric techniques by providing a visualization of a core's interior air void structure. In this work x-ray CT images were taken by and received from collaborators in the Texas A&M civil engineering department. The process is illustrated in Figure 7. Each image represents a horizontal cross section of a pavement core. Core imaging, as used in this work, refers to taking images every 1 mm over the height of an entire core. By assuming each image represents its corresponding 1 mm of core height, the stack of images can be used to represent the three-dimensional (3D) core. Sections of the core can be analyzed by grouping the corresponding images; in Figure 7 the stack has been dividing into four sections.

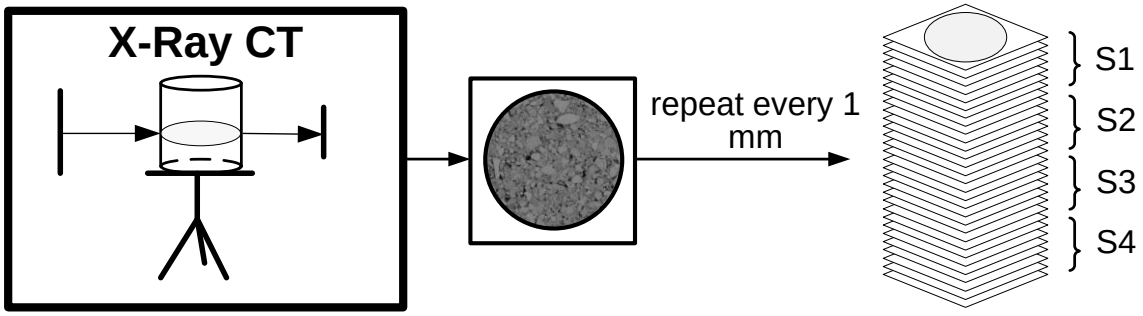


FIGURE 7 Obtaining x-ray CT images of a pavement core.

The raw x-ray CT images are grey-scale intensity type images and the pixels are data class uint16. For this type of image each pixel has a numerical value between 0 and 65,535 (Gonzalez et al., 2004). A value of 0 corresponds to pure black, and a value of 1 corresponds to pure white. Darker pixels represent areas of lower density (i.e. air voids), while lighter pixels represent areas of higher density (i.e. asphalt and aggregate) (Masad et al., 1999; Glover et al., 2104a, Ch. 13). Resolution settings result in pixels widths that correspond to approximately 0.17 mm on the core sample.

After obtaining the stack of images, image processing is performed to determine desired air void properties. Figure 8 illustrates the major processing steps used in this work.

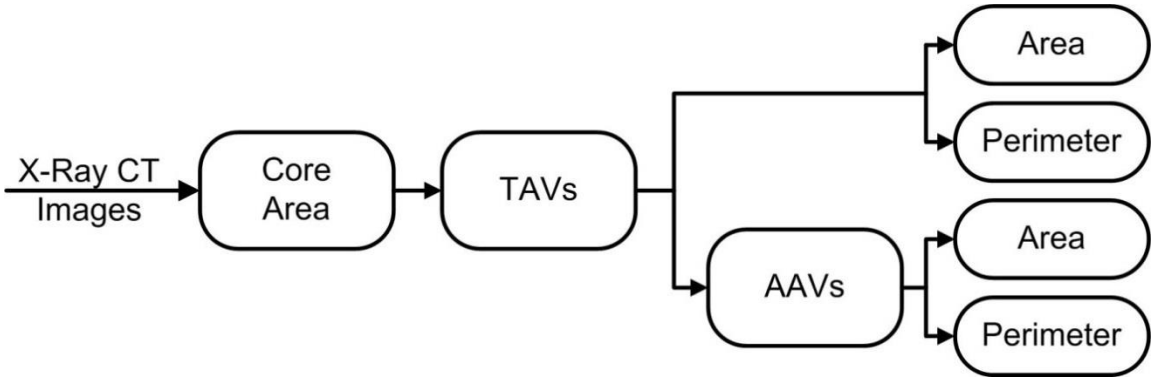


FIGURE 8 Overview of major image processing steps.

A method for determining air void properties necessary for pavement oxidation modeling from raw x-ray CT images using MATLAB software is described below; the method provides several advantages over previous approaches. A first advantage is that the method can be implemented entirely in image processing toolbox enabled MATLAB software, thereby removing the need for multiple or specialized softwares. Closely related, because the method can be implemented entirely in MATLAB software new parameters may be readily obtained by relatively slight modification. Additionally, thresholding, described below, can be performed automatically.

**FINDING THE CORE AREA**

Before beginning any substantial analysis of pavement core images it is necessary to identify the part of each image that corresponds to the core, as distinguished from the background. To do this, first, the image is "shrinkwrapped", and then a convex hull function is applied to the shrinkwrapped image. Figure 9 shows an example raw image, its corresponding shrinkwrapped image, and the final convex hull image, which is used

to approximate the core area (all example images in this chapter are from an FM 973 field core). The steps to obtain these images are described below.

a b c

FIGURE 9 (a) Raw x-ray CT image. (b) Shrinkwrapped image. (c) Convex hull image.

Figure 9(b) shows the shrinkwrapped image obtained using the function *Shrinkwrap*, available through MATLAB Central (De, 2010). In essence this function is detecting the edge of the core. The pixels that are considered part of the background are turned black, and the pixels that are considered part of the core are turned white.

Next, the convex hull of the shrinkwrapped image is created, which includes the air voids on the edge of the core in the core object. In image analysis terminology, the white area in the shrinkwrapped image can be referred to as an object (Gonzalez et al., 2004). In the shrinkwrapped image this object excludes the area corresponding to air voids at the outer edge of the core. The convex hull of an object refers to the area enclosed by drawing straight lines connecting the outermost points. The convex hull for the shrinkwrapped object is shown in Figure 9(c). This image is an approximation of the core area in that the outer edges bridging the air voids are straight lines rather than

curves, but since the air voids tend to be small the approximation is assumed reasonable. The convex hull of an image can be identified using the MATLAB function *regionprops* with the *ConvexHull* or *ConvexImage* argument.

For all further processing the convex hull image defines the location of the core within the original square image.

## IDENTIFYING THE TOTAL AIR VOIDS AND THE ACCESSIBLE AIR VOIDS

After identifying the location of the pavement core within each image, the pixels corresponding to air voids (i.e. the TAVs) are identified by thresholding. Thresholding is the process of separating an image into white and black portions using a threshold value. The pixels with values below the threshold value are turned black and the pixels with values above the threshold value are turned white. In this application the correct threshold value (i.e. a number between 0 and 65,535) is determined by adjusting a test value until the fraction of pixels in the core area below the test value (i.e. darker pixels which represent air voids) matches a lab-measured whole-core TAV volume fraction. This thresholding process must be applied to the entire stack of images since lab measurement is made on a whole core. Automatic adjustment of the test value to determine the threshold value can be accomplished using the *fminbnd* function in MATLAB.

An example TAV image is shown in Figure 10(a). The color scheme has been flipped so that white represents the air void objects and black represents everything else. The air void objects represent air void cross sections. The TAV fraction for an individual

image, representing a specific depth within the pavement core, is calculated as the white area in the TAV image divided by the white area in the convex hull image. Likewise, average TAV fractions for sections (see Figure 7) of a pavement core can be calculated by averaging the TAV fractions for the individual images corresponding to the section.

a b

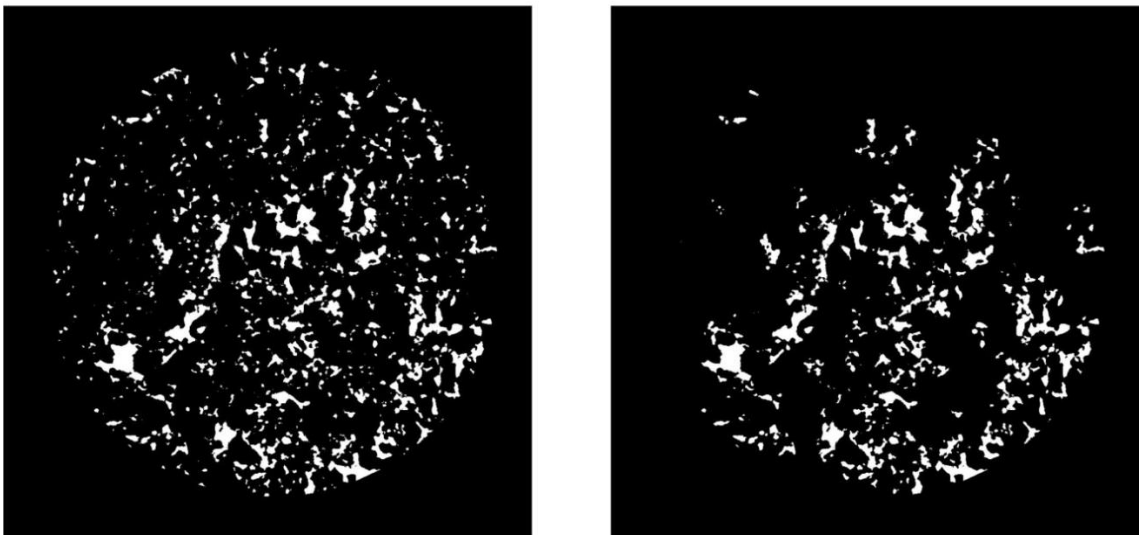

FIGURE 10 Total air voids and accessible air voids.

As part of the image thresholding process edge cleaning may be incorporated. Edge cleaning refers to removal of an air void ring that may appear around the outer edge of the core area in some images. This apparent air void ring is an artifact of the coring process. One simple approach is to define a few layers of outer boundary pixels to be entirely solid material.

After identifying the TAVs, the AAVs are identified. The first step is to identify all of the individual air voids in the pavement core. The TAV images, which are

2-dimensional (2D) arrays (representing pavement core cross sections), are stacked to create a 3D array, and each set of connected air void pixels is defined as an individual air void. A 26-connect connection scheme is employed (Gonzalez et al., 2004). To understand this scheme, consider Figure 11. Two different 2D connection schemes are shown: 4-connect and 8-connect. The difference is that in 8-connect pixels that are only touching at a corner are still considered neighbors (i.e. connected). The natural extension of 8-connect to 3D is 26 connect.

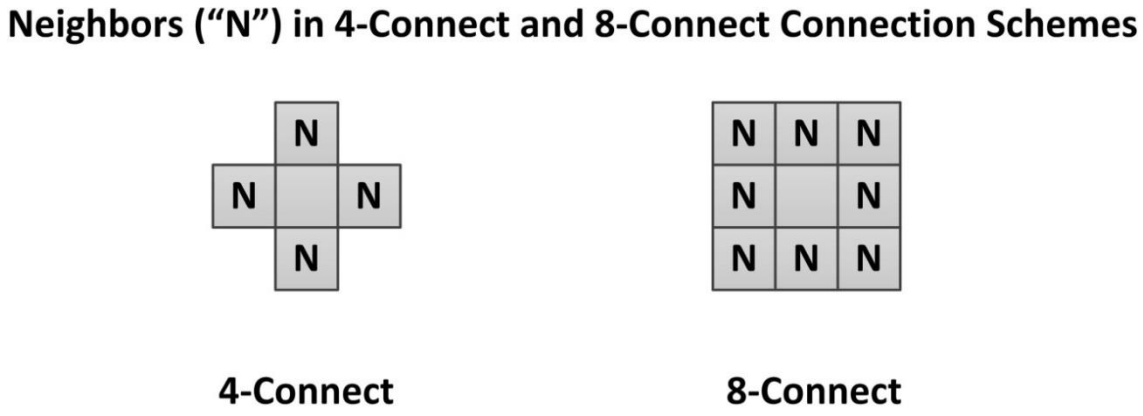


FIGURE 11 Distinguishing 4-connect and 8-connect 2D connection schemes.

After identifying the individual air voids, each air void must be labeled so that it can be distinguished. One approach is to label all of the pixels corresponding to a single air void with the same value. Figure 12(a) illustrates this concept in 2D. For simplicity, only four air voids are shown and pixels size is exaggerated. The natural extension of this concept to 3D is used to label the individual air voids in the 3D array that represents the pavement core. In MATLAB, identification and labeling of the individual air voids

may be done simultaneously using the function *bwlabeln* with 26 for the connectivity argument.

a b

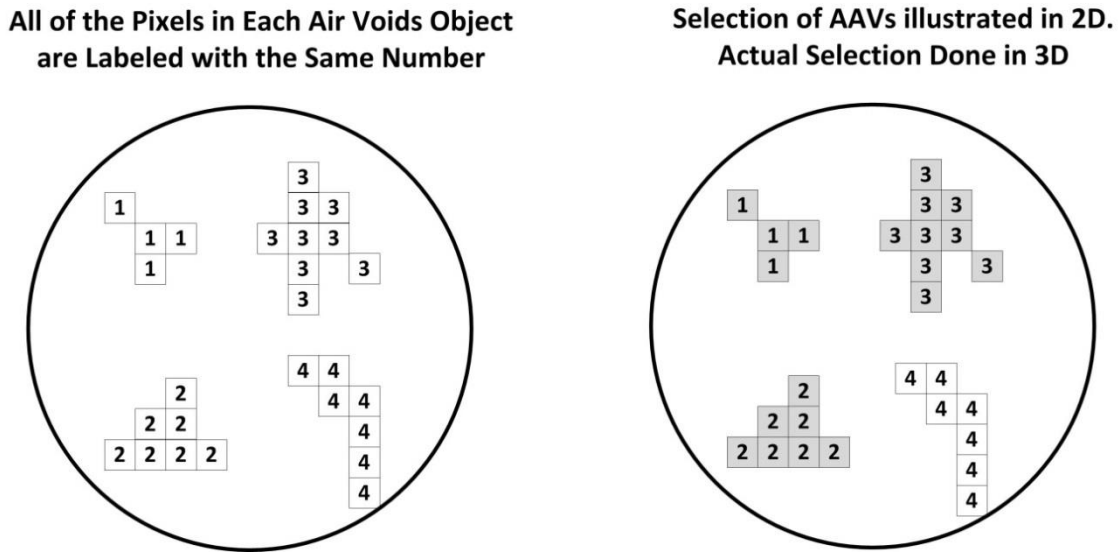


FIGURE 12 (a) Labeling of individual air voids (b) Conceptual identifying of AAVs in 2D.

Once the air voids (i.e. the TAVs) in the core are each identified and labeled, the AAVs are distinguished. Following Jin (2012), in this work accessibility refers to accessibility to the pavement surface because the pavement lifts studied are over consolidated bases (i.e. previously constructed lifts). For simplicity, the method of identifying the AAVs is illustrated in 2D in Figure 12(b). Only the air void labeled with the number 4 forms part of the outer edge and therefore only that air void may be considered accessible in this 2D sense. The 3D application is analogous, but rather than identifying air voids that are part of the outer edge, the air voids that form part of the uppermost image (i.e. the surface image) are identified. Alternative definitions of

accessibility, such as top and bottom surface accessibility would require an appropriately modified selection procedure.

Once the AAVs are identified their corresponding pixels are set to white and all other pixels are set to black to create images such as the one shown in Figure 10(b), above. To determine the fraction of AAVs for a given image divide the number of white pixels in the AAV image by the number of white pixels in the corresponding convex hull image. As for TAVs, average AAV fractions for pavement core sections can be calculated by averaging the fractions from the individual images corresponding to the section.

**DETERMINING AIR VOID OBJECT PERIMETER, AREA, AND NUMBER**

After identifying the TAVs and the AAVs, the perimeter and area of the air void objects (i.e. cross sections), as seen in the 2D images, can be determined. Although the cross sections are referred to here as air void objects, in other parts of this work, and in some previous work, the air void objects are simply referred to as air voids. The techniques used are the same whether applied to TAV images or AAV images.

Determining the perimeter of the air void objects in an image can be accomplished in two steps: first find the boundaries of the air void objects, and second determine the length of the boundaries. The boundaries of the air void objects in a specific image can be found using the MATLAB function *bwboundaries*. Figure 13 shows an example of the boundaries for a TAV image. The length of an individual

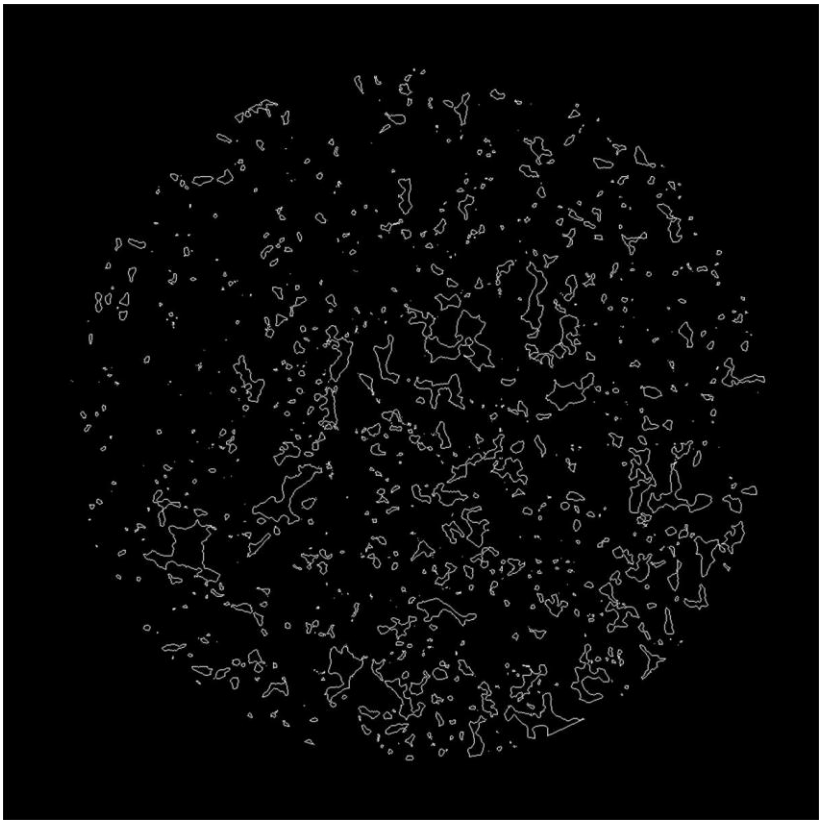

FIGURE 13 Total air void boundaries.

boundary can be determined by using the corresponding boundary chaincode (Gonzalez et al., 2004) in conjunction with the physical length corresponding to the width of a pixel (i.e. 0.17 mm). Chaincodes can be determined using the function *chaincode*, available through MATLAB Central (Mannini, 2010).

One way to determine the number of air void objects in an image is from the output of the function *bwboundaries*. The number of boundaries output corresponds to the number of air void objects. Therefore, the number of air void objects can be determined by taking the length of the *bwboundaries* function output. There are several similar alternatives methods for finding the total number of air void objects.

In addition to the perimeter of each air void object the area of each air void object can be determined. This area represents the cross sectional area of an air void pore. To estimate this area, first, the number of pixels in each air void object is determined. This can be done using the MATLAB function *regionprops* with the argument *area*. The number of pixels can then be converted to an area using the physical area per pixel.

## SUMMARY AND OVERVIEW OF SPECIFIC PARAMETER CALCULATIONS

A method for analyzing x-ray CT images to determine air void fraction, and air void object numbers, areas, and perimeters for both TAVs and AAVs is provided; no additional image analysis methods are required to complete the calculations needed to obtain the oxidation modeling parameters used in this work. Nonetheless, a brief overview of relevant oxidation modeling parameters and their calculation is provided here. Additional discussion is presented, as applicable, in the following chapters.

When depth-specific modeling is performed, as done in this work, average parameter values are calculated by averaging over the images corresponding to each section (recall Figure 7). Core sections, in turn, are often defined to correspond to core slices (typically 12.7 mm (0.5 inch) in height, see Ch. I).

As discussed in Chapter I, the cylindrical oxidation modeling approach requires an average air void pore radius and a NFB. Following Han (2011) and Arambula et al. (2007) the radius of an air void pore is defined as the radius of a circle having an area equal to the area of the air void object that represents the pore. Using this definition and

the air void object areas, the radius for each air void pore, as seen in a given image, can be determined. An average pore radius for each image can be calculated, and finally these averages can be averaged over the images corresponding to a core section. In addition to the average air void pore radius, the radius of the NFB cylinders must also be determined. To determine the radius of the NFB cylinders it is assumed that the total cross sectional area of the NFB cylinders matches the total cross sectional area of the pavement core (Han, 2011). Using this assumption, and the average number of air void pores, the radius of the NFB cylinders is calculated (formula provided in Chapter V). The number of air void pores for an image can be estimated as the number of air void objects in the image, and this estimate can be averaged over any core section.

For the $d_D$ modeling approach, the $d_D$ must be calculated for each core section of interest. The $d_D$ is calculated as the asphalt volume divided by the surface area of the AAVs. Following Jin et al. (2013) the asphalt volume is assumed evenly spread over the height of the pavement lift. The total asphalt volume can be calculated from the core mass, the asphalt weight percent, and asphalt specific gravity (weight percent and specific gravity typically available in mix design). Using the total asphalt volume, the volume of asphalt in a core section is calculated using the ratio of the section height to the total core height. After calculating the asphalt volume the surface area of the AAVs is estimated. The total perimeter for all of the air void objects in an AAV image can be determined by adding the lengths of all of the individual air void object boundaries. Assuming the image represents its corresponding 1 mm of core height, the AAV surface area represented by the image is calculated by multiplying the total boundary length by 1

mm. Then, the AAV surface area for a core section is calculated by summing the surface area contributed by each image in the section. Finally, the $d_D$ can be calculated as the asphalt volume in the section divided by the surface area of the AAVs.

In addition to the specific parameters required for the cylindrical and $d_D$ oxidation modeling approaches several other insightful analyses can be performed using the information gained from image analysis. As an example, both TAV and AAV fraction can be easily plotted as a function of depth below the pavement surface to allow for visual comparison. Similarly, average TAV or AAV fraction for any section of the core can be calculated. Plots showing this type of information are provided in the following chapters. As another example, air void size probability density functions can be plotted to gain understanding of air void size variation (Han, 2011).

# CHAPTER III

# AN X-RAY CT VALIDATED LABORATORY MEASUREMENT METHOD FOR AIR VOIDS DISTRIBUTION OVER DEPTH IN ASPHALT PAVEMENT: A STEP TOWARDS SIMPLIFIED OXIDATION MODELING[*]

## INTRODUCTION

Asphalt pavement oxidation modeling relies on air void information to predict binder oxidation and hardening (Han, 2011; Jin et al., 2013). A key parameter, the diffusion depth ($d_D$), is the ratio of the binder volume to the surface area of the accessible air voids within the pavement (Jin et al., 2013). Accessible air voids are defined as pores that are connected to an oxygen-exposed surface of the asphalt pavement layer and are usually quantified via x-ray computed tomography (CT) on asphalt pavement cores (Jin, 2012). Because x-ray CT is a technique available only in advanced asphalt materials testing facilities, prediction modeling using $d_D$ is often limited.

Although pavement oxidation modeling motivates this work, the need for air void distribution measurements is ubiquitous in asphalt testing, which has led to significant recent research, as well as skepticism regarding traditional approaches. (Masad et al., 1999; Masad et al., 2002; Tashman et al., 2002; Arambula et al., 2007; Alvarez et al, 2009). Tashman et al. (2002) put it bluntly, stating that many research

[*] Reprinted with permission from "An X-ray CT Validated Laboratory Measurement Method for Air Voids Distribution Over Depth in Asphalt Pavement: A Step Toward Simplified Oxidation Modeling" by A. A. Rose, E. Arambula, T. Howell, and C. J. Glover, 2014. *Petroleum Science and Technology*, 32 (24), 3020–3028 , Copyright 2014 by Taylor & Francis.

efforts relying on whole-core average air voids information, because of limited laboratory techniques, produce results that are "not realistic."

Pioneering efforts have been made towards identifying a means for estimating the air void distribution in pavement cores using readily available equipment and familiar techniques, but prototype methods have not been completely defined, statistically evaluated, or compared with x-ray CT. Chehab et al. (2000) recognized that variations in air void distribution affect Superpave test results and presented a reverse solution: prepare and cut samples to have uniform air void distributions. To identify regions of uniformity, researchers cut laboratory-prepared cores into slices and measured the bulk specific gravity (BSG) of each slice. The maximum theoretical specific gravity (MTSG), needed for the total air void (TAV) calculation, was measured on loose mixes and assumed uniform. Because the slices were approximately 0.9 inch thick, the specimen size was insufficient to rely on the BSG precision statement included in the standard method, and no independent precision analysis was presented. Woo et al. (2007) presented a novel method, explained below and partially adopted in this work, for determining the MTSG in core slices, but like Chehab et al. (2000), did not provide precision estimation or comparison to x-ray CT.

This work presents a complete method for determining vertical TAV distributions in asphalt pavement cores using readily available equipment and familiar techniques, and includes statistical evaluation, binder oxidation monitoring, and x-ray CT comparison. TAV distribution determination has multiple independent applications

in asphalt research besides oxidation modeling. Work towards estimating accessible air voids and diffusion depth is ongoing.

## EXPERIMENTAL METHODOLOGY

### Materials

Six field cores, numbered and detailed in Table 1, cut into 0.4 inch (nominal thickness) slices, as well as extracted and recovered binder from replicates of cores 1 through 5, and previous test results on unaged binder (Glover et al., 2014b), were evaluated in this study. Cores 1 through 5 are from FM 973, a road near Austin, TX. Core 6 is from the Yellowstone National Park (YNP); this core is taller, contains larger aggregate, and a binder PG grade suited for colder climate.

### Laboratory TAV Measurement Method

Cores were cut horizontally at vertically-spaced half-inch intervals to create nominal 0.4 inch thick slices. This thickness is the practical minimum for standard core sawing equipment and corresponds to pavement oxidation modeling slice thickness (Han, 2011; Jin et al., 2013). The BSG is determined on each slice three separate times. In addition to providing improved precision, the replicate measurements provide data that can be used to assess precision. Next, guided by the work of Woo et al. (2007), each slice is hammered to separate whole aggregate pieces (without heating that would cause binder oxidation). Approximating the ASTM MTSG test specification (see below), hammering continues until the separated pieces fit through a 0.375 inch sieve. Whole aggregates, too big for the sieve opening, are added to the sieved material without

TABLE 1
Description of Asphalt Field Cores Used in the TAV Measurement Study

| *Core* | *Height [inch]* | *# of 0.4" Slices*[c] | *Nom. Max. Agg. Sz. [inch] (mm)* | *Max. Agg. Sz. [inch] (mm)* | *Warm Mix Technology* | *Construction / Coring* |
|---|---|---|---|---|---|---|
| **1**[a] | 1.3 | 2 | 3/8 (9.5) | 3/4 (19.1) | None | Jan. '12 / Jan. '12 |
| **2**[a] | 1.8 | 3 | 3/8 (9.5) | 3/4 (19.1) | Foamed | Jan. '12 / Jan. '12 |
| **3**[a] | 1.5 | 3 | 3/8 (9.5) | 3/4 (19.1) | None | Jan. '12 / Mar. '13 |
| **4**[a] | 1.5 | 3 | 3/8 (9.5) | 3/4 (19.1) | Foamed | Jan. '12 / Mar. '13 |
| **5**[a] | 1.5 | 3 | 3/8 (9.5) | 3/4 (19.1) | Evotherm | Jan. '12 / Mar. '13 |
| **6**[b] | 4.3 | 8 | 0.75 (19.0) | 0.98 (25.0) | None | '07 / '11 |

[a] FM 973, Austin, TX; Valero PG 70-22; Aggregate: 91 wt.% limestone dolom., 9 wt. % gravel.
[b] E. entrance of YNP; Idaho Asphalt PG 58-34; Aggregate: Greymont lime.
[c] Bottom slice left slightly thicker than other slices if needed to accommodate total core height.

breaking into fragments. The gravel-like material serves as an alternative to loose mix. As with the BSG, the MTSG is measured three times. A vacuum dryer makes repetitive testing practical by reducing the test time, while maintaining a low enough temperature and oxygen pressure that binder oxidation is limited (Instrotek, 2010). TAVs for the slices were calculated from the BSG and MTSG results.

The use of BSG and MTSG measurements to determine TAVs is outlined in ASTM D3203, but several procedural options are presented. For the BSG measurement, the vacuum sealing method (ASTM D6752) was selected, as suggested by Chehab et al. (2000). For the MTSG measurement, both the vacuum sealing (ASTM D6857) and Rice methods (ASTM D2041) were evaluated (Woo et al., 2007), and ultimately the Rice method is recommended.

Deviations from standard procedures are assured when measuring BSG and MTSG on 0.4 inch core slices. The standard method for BSG, ASTM D6752, requires the sample height be at least 1.5 times the maximum aggregate size. Even for the FM 973 cores, this means the minimum specimen height requirement is more than 1.1 inches (almost 3 times slice thickness). The MTSG procedures give rise to additional reasons for uncertainty: analogous to the BSG issue, the mass of the gravel-like material obtained from a 0.4 inch slice is significantly less than required by the standard MTSG test methods, additionally, the MTSG methods are intended for use on loose mix asphalt. Even if original loose mix were tested, a single MTSG value is not sufficient to evaluate variation with pavement depth.

**X-ray CT Comparison**

Prior to destructive testing, x-ray CT images of the field cores were analyzed to calculate TAVs through the core depth; comparison was made to the TAVs of the cut slices. An image processing code was developed using image-processing-toolbox enabled MATLAB® software. Following previous techniques (Masad et al., 2002; Han, 2011; Jin et al., 2013), a TAV threshold value was determined from a whole core measurement of the BSG and an available MTSG value (construction loose mix MTSG measurement for FM 973 cores and design MTSG for YNP core). Slice BSG and MTSG values are shifted so their average values match their corresponding whole core values prior to calculating slice TAVs and comparing with x-ray CT.

**Vacuum Drying Oxidative Aging**

Significant oxidation from vacuum drying could preclude the use of extracted binder for oxidation model calibration and evaluation. Jin et al. (2011) developed a fast-rate–constant-rate oxidation model that can be used to estimate the oxidation caused by vacuum drying, in terms of carbonyl area (CA):

$$\Delta\mathrm{CA} = M\left(1 - e^{k_f \cdot t}\right) + k_c \cdot t \tag{13}$$

$$k_f = A_f \cdot e^{\frac{-E_{af}}{R \cdot T}} \tag{14}$$

$$k_c = A_c \cdot e^{\frac{-E_{ac}}{R \cdot T}} \tag{15}$$

where $M$ is the total possible field increase in CA resulting from the fast-rate reaction, $k_f$ and $k_C$ are reaction constants, and $E_{af}$, $E_{ac}$, $A_f$, and $A_c$ are asphalt-specific reaction kinetics parameters. As an example, Valero 70-22, the base binder in the FM 973 road sections, was considered. Model calculations assumed 1-atm air (significantly higher than in a vacuum dryer), an asphalt film that is thin enough to provide a uniform oxygen concentration through its depth, a higher-than-average $M$ value of 0.20 (tends to overestimate effect of fast-rate reaction), 2 hours of drying time (longer than would be needed for numerous vacuum drying cycles on 0.4 inch slices), and a temperature of 120 °F (the maximum for the vacuum dryer). The reaction kinetics parameters for the FM 973 asphalt were reported by Glover et al. (2014b).

To compare with model estimates, CA was measured on extracted and recovered field-core binders (Cui et al., 2015), with and without vacuum drying. Binder from the FM 973 core slices (subjected to at least 6 vacuum drying cycles) and replicate FM 973 cores was extracted and recovered. Whole core average FTIR CA measurements and original binder CA values reported by Glover et al. (2014b) were compared.

## RESULTS AND DISCUSSION

### Statistical Evaluation and X-ray CT Comparison

Because procedural deviations are assured, standard method precision statements cannot be relied upon and precision must be evaluated. The standard deviation of the BSG test method and the MTSG test methods were evaluated following common techniques from control chart theory for applications where the precision of a test method is unknown (Vining, 1998).

As an example, consider the BSG test method (analogous for MTSG). All 22 slices, from all 6 cores, were treated as independent samples (with no particular relation to their parent core). Each slice was tested three times; from these three tests it is possible to estimate the variance (standard deviation squared) of the test method. Repeating on all 22 slices provides 22 method variance estimates (note that while the measured BSG values for each slice, even from a single core, are expected to vary, the BSG measurement method variance is not expected to vary, regardless of whether slices come from one or several cores). A best estimate of the method variance is determined

by averaging the 22 estimates from the individual slice tests. A 90% confidence interval is estimated using a chi-squared distribution (Vining, 1998).

Total air voids are calculated using the BSG and MTSG values:

$$\mathrm{TAV} = 1 - \frac{\mathrm{BSG}}{\mathrm{MTSG}} \tag{16}$$

Applying error propagation to the TAV formula, the result presented in ASTM D3203 is derived (Taylor, 1982):

$$\sigma_{\mathrm{TAV}} = \sqrt{\frac{\mathrm{MTSG}^2 \cdot \sigma_{\mathrm{BSG}}^2 + \mathrm{BSG}^2 \cdot \sigma_{\mathrm{MTSG}}^2}{\mathrm{MTSG}^4}} \tag{17}$$

where $\sigma$ indicates the standard deviation of the respective measurement method.

Figure 14(a) shows the standard deviations for the BSG and MTSG methods applied to 0.4 inch core slices compared to σ reported in the ASTM method precision statements. The BSG vacuum sealing method and the MTSG Rice method performed well, yielding $\sigma$ nearly equivalent to the ASTM values. The MTSG vacuum sealing method, on the other hand, resulted in considerably worse precision. Confidence intervals (90 %) for $\sigma$, are relatively small, making it reasonable to use the mean values as the true population $\sigma$ for the purpose of calculating only the BSG and MTSG Rice confidence intervals, although it is done below for all three cases.

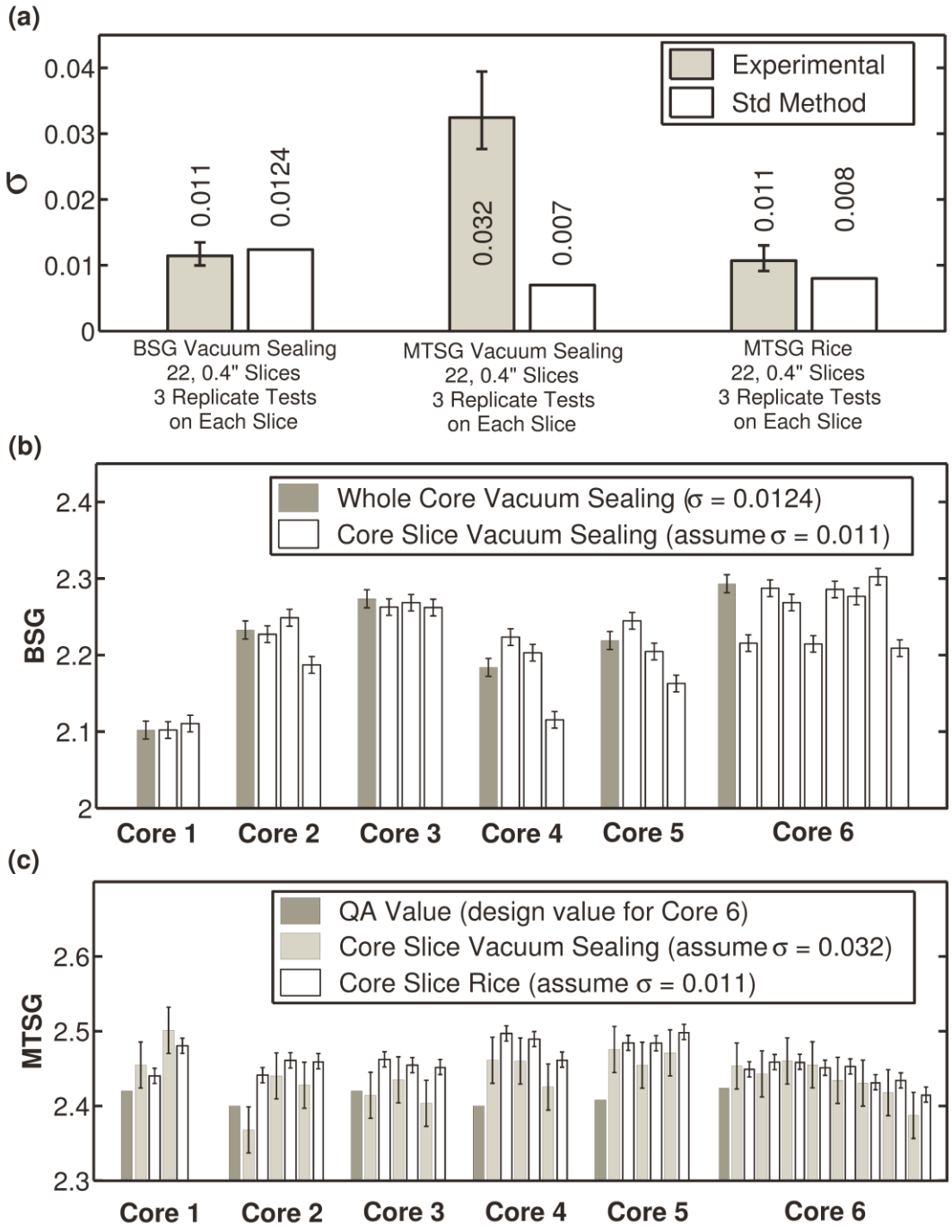


FIGURE 14 (a) Experimentally determined standard deviation (σ) for test methods on 0.4 inch core slices compared with standard method precision statement σ (BSG Vac. Seal.: ASTM D6752; MTSG Vac. Seal.: ASTM D6857; MTSG Rice: ASTM D2041). (b) BSG mean and 90% CI (n=3); (c) MTSG mean and 90% CI (n=3). Slice depth increases from left to right for both figures (b) and (c).

The whole core and slice BSG values are shown in Figure 14(b). For each core, depth below the surface increases left to right. Error bars represent 90% confidence intervals on the mean (three replicate tests). Whole core confidence intervals are based on $\sigma$ reported in ASTM D6752; slice intervals are calculated using the estimated $\sigma$ values from Figure 14(a). The precision of the BSG vacuum sealing method is sufficient to identify slice-to-slice differences in many cases (as a rule of thumb, statistical significance can be inferred when the distance between means is at least 1.4 times the length of a single error bar). Noting that BSG is inversely related to TAVs, the results for core 6 are particularly revealing: two lifts are seen.

Analogously, Figure 14(c) shows MTSG results. The whole-core values for the FM 973 cores are from construction loose mix measurements (i.e. QA values). The whole-core value for the YNP core is the design value. The results for both the vacuum sealing and Rice MTSG tests are shown for each slice. The precision of the MTSG vacuum sealing method is significantly less than the precision of the Rice method. As a result, in general, it is not possible to identify slice-to-slice differences using the vacuum sealing method, while, in many cases, it is possible using the Rice method.

Slice TAV values, calculated from the BSG and MTSG (Rice) measurements, are compared to x-ray CT in Figure 15(a and b). Figure 15(a) presents a detailed comparison for cores 5 and 6. Figure 15(b) presents cores 1 through 4 in a more compact format. Error bars, representing 90% confidence intervals (n=3), were calculated using error propagation. Both figures show that slice TAVs trend well with x-ray CT.

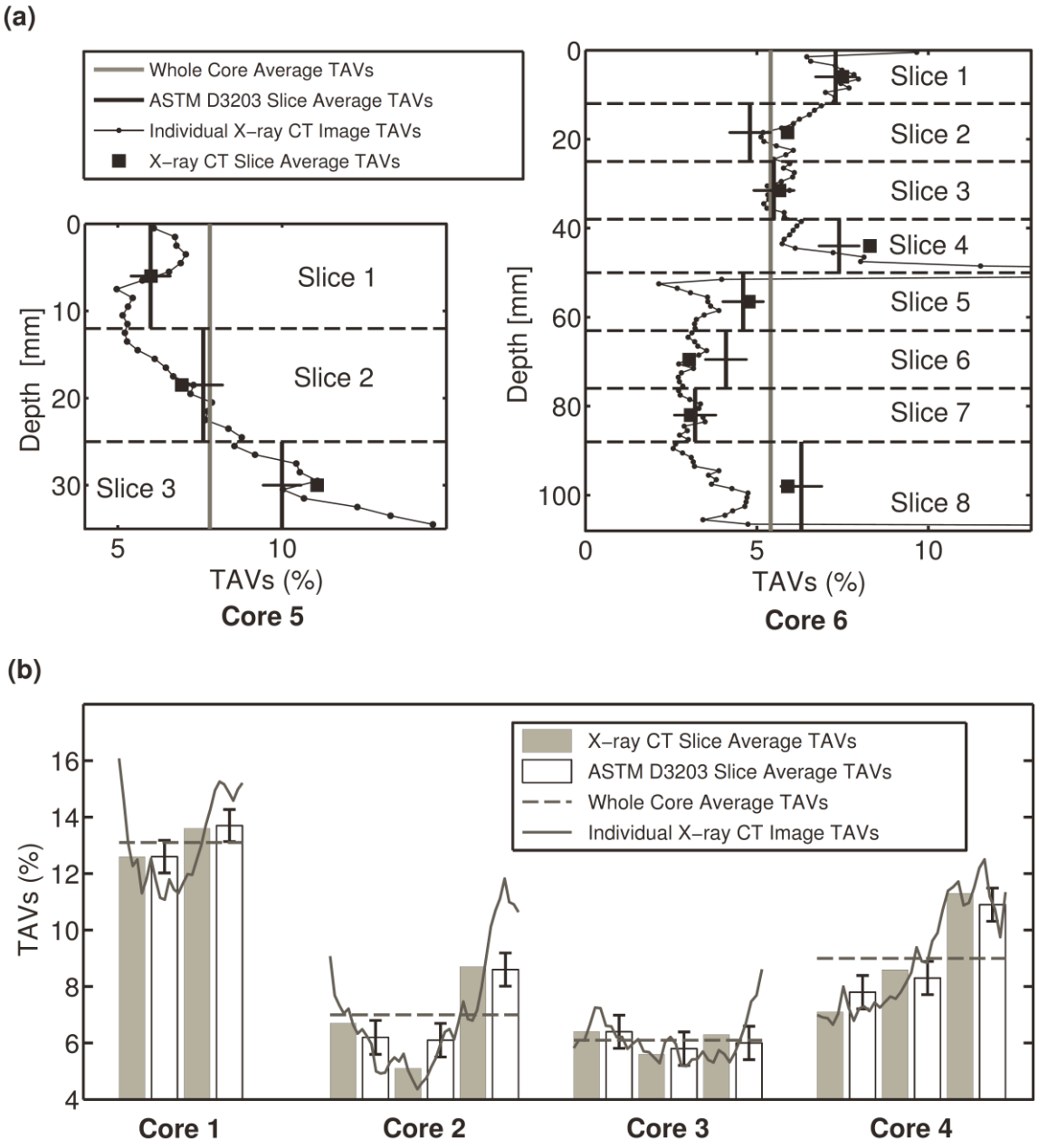


FIGURE 15 Comparison of ASTM D3203 TAVs on 0.4 inch slices with x-ray CT (a) Detailed presentation of cores 5 and 6; horizontal error bars on ASTM D3203 slice TAVs represent 90% CI on mean (n=3) (b) Compact presentation of cores 1–4; error bars represent 90% CI on mean (n=3).

Considering Figure 15(a) more closely, core 5 has a strong increase in air voids from the top of the core to the bottom of the core (similar to core 4); slice measurements did an excellent job identifying the trend. Core 6 has two dominant qualitative characteristics and slice measurements made both unmistakable: (1) two lifts each lift having a C-shaped air void distribution, and (2) a lower average air void content in the lower lift.

Table 2 provides a quantitative comparison of three different methods for approximating the TAV distribution when x-ray CT is not available. The three possibilities considered are: (1) slice-specific BSG (vacuum sealing) measurement and slice-specific MTSG (Rice) measurement ($SS_{vs}$ & $SS_{Rice}$), (2) slice-specific BSG measurement and a whole core average MTSG measurement ($SS_{vs}$ & WC), and (3) both BSG and MTSG whole core averages (WC & WC). Table 2 errors are expressed as percentage points in relation to x-ray CT results (e.g. 0.4 % error could mean x-ray CT TAVs: 10 %; measured TAVs: 10.4 %). The average error is defined as the average difference between the approximation and the x-ray CT value, averaged over all slices. The maximum error is the maximum difference between the approximate and the x-ray CT value for any slice in the core. The final row "Average" shows that $SS_{vs}$ & $SS_{Rice}$ provides the best estimate overall (average error one-third of WC & WC), but that $SS_{vs}$ & WC is almost as good (and is actually slightly better for cores 2 and 4). Based on these limited results, one might conclude that MTSG is fairly consistent within a single lift, meaning that TAVs distribution is primary determined by BSG variation. In a multiple-lift situation (e.g. core 6) MTSG variation is more important.

TABLE 2
Slice TAV Percentage Point Error when Compared to X-ray CT

| | | Total Air Void Measurement Technique (BSG & MTSG) | | |
|---|---|---|---|---|
| ***Core*** | ***Error Type*** | $SS_{VS}$ & $SS_{Rice}$[a] | $SS_{VS}$ & $WC$[b] | $WC$ & $WC$[c] |
| **Core 1** | Avg. Error | 0.1 % | 0.7 % | 0.5 % |
| | Max. Error | 0.1 % | 0.8 % | 0.6 % |
| **Core 2** | Avg. Error | 0.5 % | 0.3 % | 1.3 % |
| | Max. Error | 1.0 % | 0.7 % | 1.9 % |
| **Core 3** | Avg. Error | 0.2 % | 0.3 % | 0.3 % |
| | Max. Error | 0.3 % | 0.3 % | 0.5 % |
| **Core 4** | Avg. Error | 0.4 % | 0.3 % | 1.5 % |
| | Max. Error | 0.7 % | 0.5 % | 2.3 % |
| **Core 5** | Avg. Error | 0.6 % | 0.8 % | 2.0 % |
| | Max. Error | 1.1 % | 1.5 % | 3.3 % |
| **Core 6** | Avg. Error | 0.5 % | 1.0 % | 1.4 % |
| | Max. Error | 1.1 % | 1.7 % | 2.9 % |
| **Average** | Avg. Error | 0.4 % | 0.6 % | 1.2 % |
| | Max. Error | 0.7 % | 0.9 % | 1.9 % |

[a] Slice specific (SS) BSG using vacuum sealing (vs) & SS MTSG using Rice.
[b] SS BSG using vacuum sealing & Whole Core (WC) average MTSG.
[c] WC average BSG using vacuum sealing & WC average MTSG.

## Vacuum Drying Oxidative Aging

Having identified a generally-practicable method of determining TAV distributions, it remains to be shown that any resulting vacuum-dryer-caused oxidation does not prevent the use of the binder for oxidation model calibration. Applying the fast-rate–constant-rate model of Jin et al. (2011) and the assumptions described above, an upper limit on the expected carbonyl increase for Valero 70-22 is only 0.002. Figure 16, provides both perspective and validation. The CA increase during the first 14 months in the field was

approximately 0.15. Therefore, the vacuum-dryer-induced oxidation is less than 1% of field aging. From Figure 16 it is clear that the trend is dominated by field aging and variability, with little or no detectable oxidation resulting from vacuum drying.

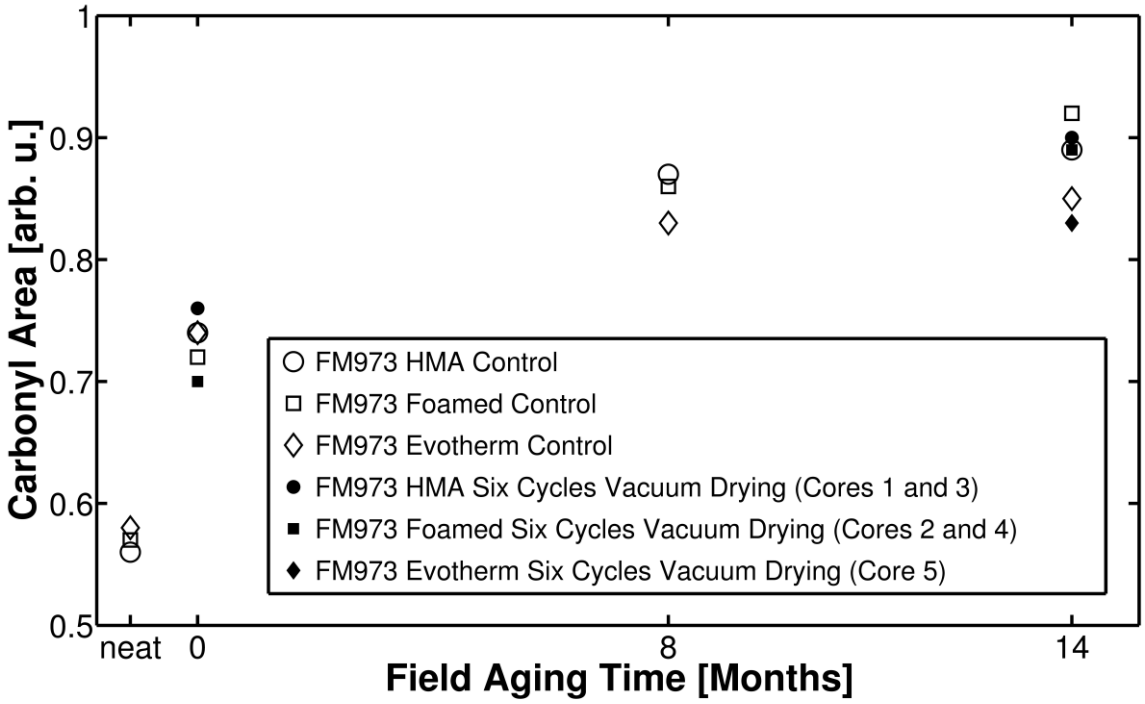


FIGURE 16 Carbonyl area comparison: field core material subjected to at least 6 cycles of vacuum drying, replicate field core material not subjected to vacuum drying, and neat binder.

**SUMMARY**

This work presented a complete method for determining TAV distributions in asphalt pavement field cores using readily available asphalt-testing equipment. Statistical precision evaluation supported the use of the BSG vacuum sealing method and the MTSG Rice method on 0.4 inch slices. Slice TAVs were validated by direct comparison with x-ray CT. Quantitative results showed that slice measurement average percentage

point errors are one-third of whole core approximation errors. BSG appears to control TAV distributions with MTSG playing a more critical role for multi-lift cores. A vacuum dryer allows for efficient repetition without damaging the asphalt by oxidation. Ongoing work focuses on linking TAVs and diffusion depth, a parameter needed for pavement oxidation modeling.

# CHAPTER IV

# USE OF A TOTAL AIR VOID DIFFUSION DEPTH TO IMPROVE PAVEMENT OXIDATION MODELING WITH FIELD VALIDATION*

## INTRODUCTION

Pavement oxidation modeling can be used to predict binder hardening and pavement failure (Prapaitrakul et al., 2009; Han, 2011; Jin et al., 2013). The reaction of oxygen with asphalt produces carbonyl, thereby increasing FTIR measured carbonyl area (CA), which has a positive correlation with the DSR function (a.k.a. the Glover-Rowe parameter) (Juristyarini et al., 2011a). The DSR function is further correlated with ductility, which, in turn, has been related to pavement failure (for discussion see Ruan et al., 2003). The diffusion depth ($d_D$), defined as the binder volume divided by the accessible air void (AAV) surface area, is a key modeling parameter. Pavement core AAV data have been determined via x-ray CT.

Previous oxidation models use analysis of x-ray CT images to identify air voids that have a connected path to the pavement surface, and assume that air voids identified in this manner are the air voids that are accessible to oxygen (i.e. the AAVs). The need to distinguish AAVs from TAVs arises from the assumption that a significant portion of TAVs are inaccessible to oxygen. These assumptions may have been guided by similar work that focused on the related but distinct concepts of water accessibility, water

* Reprinted with permission from "Use of a Total Air Void Diffusion Depth to Improve Pavement Oxidation Modeling with Field Validation" by A. A. Rose, E. Arambula, G. Liu, and C. J. Glover, 2015. *Petroleum Science and Technology*, 33 (11), 1198–1207, Copyright 2015 by Taylor & Francis.

permeability, and interconnected air voids (i.e. air voids that pass all the way from the top surface of a lift to the bottom surface) (e.g. Arambula et al., 2007; Glover et al., 2014a).

Usage of x-ray CT image analysis to distinguish AAVs from TAVs, by identifying connected paths, has intuitive appeal, but length-scale considerations cast doubt on the approach. In the works cited above (and in this work) x-ray CT resolution settings result in pixel widths of approximately 0.17 mm. Resolution settings can be increased, but whole-core scans become prohibitively resource consuming, and even then, resolution remains on a similar scale (Das et al., 2014). Smaller air voids may go undetected by x-ray CT, and could provide passageways for oxygen molecules, which have a mean free path on the order of 100 nm (Deen, 2012).

The herein reported work takes a more empirical approach and attempts to improve upon previous work by using x-ray CT identified TAVs, rather than x-ray CT identified AAVs, for oxidation modeling. To avoid confusion, the term AAVs continues to mean x-ray CT identified AAVs, yet this work examines the possibility that TAVs may, in fact, be almost entirely accessible to oxygen. Experimental results from nine field cores are analyzed to compare variation over depth of TAVs, AAVs, and field oxidation. A new $d_D$ based on x-ray CT TAVs ($d_{D\_TAV}$, i.e. TAV diffusion depth) is proposed. The $d_{D\_TAV}$ is defined as asphalt volume divided by TAV surface area. Oxidation modeling is performed using the $d_{D\_TAV}$ and the original $d_D$ based on AAVs (now designated as $d_{D\_AAV}$, i.e. AAV diffusion depth).

## MATERIALS AND METHODS

### Materials

This study includes nine field cores, numbered and detailed in Table 3, from four Texas locations. Cores 1–6 and 7–9 are, respectively, part of two separate studies funded by the Texas Department of Transportation (TxDOT); substantial background information can be found in the corresponding reports (Glover et al., 2014a; Glover et al., 2014b). All of the cores were obtained approximately 15 to 20 months after overlay construction.

### X-ray CT Image Analysis

Prior to destructive testing, greyscale x-ray CT images, representing horizontal core cross sections, were taken every 1 mm over the height of each core. These 2D images are stacked vertically to create a 3D representation of the core. Each 2D image is assumed to represent its respective 1 mm of core height. Researchers developed image analysis code, using Image Processing Toolbox enabled MATLAB software, to identify TAVs and AAVs, and to calculate their $d_D$ values. Methods built on previous works; key details are discussed below (Arambula et al., 2007; Prapaitrakul et al., 2009; Han, 2011; Jin et al., 2013; Rose et al., 2014).

TABLE 3
Description of Asphalt Field Cores Used in the TAV Diffusion Depth Study

**Pavement and Coring**

| *Core* | *Location (all TX)* | *Road* | *Lane Position* | *Construction* | *Coring* |
|---|---|---|---|---|---|
| **1** | Del Rio | US 277 | Wheel Path | Apr. 2008 | Dec. 2009 |
| **2** | Del Rio | US 277 | Shoulder | Apr. 2008 | Dec. 2009 |
| **3** | Lubbock | US 82 | Wheel Path | Jul. 2008 | Dec. 2009 |
| **4** | Lubbock | US 82 | Shoulder | Jul. 2008 | Dec. 2009 |
| **5** | Childress | US 83 | Wheel Path | Jun. 2008 | Oct. 2009 |
| **6** | Childress | US 83 | Shoulder | Jun. 2008 | Oct. 2009 |
| **7** | Austin | FM 973 | Btw. Wheel Path | Jan. 2012 | Mar. 2013 |
| **8** | Austin | FM 973 | Btw. Wheel Path | Jan. 2012 | Mar. 2013 |
| **9** | Austin | FM 973 | Btw. Wheel Path | Jan. 2012 | Mar. 2013 |

**Diffusion Depth: Binder Characteristics**

| *Core* | *Core Volume*[a] *[cm$^3$]* | *Core Mass [gm]* | $G_{mm}$ [b] | $P_b$ [c] | $G_b$ [c] | *AV* [d] *(%)* |
|---|---|---|---|---|---|---|
| **1** | 876 | - | 2.497 | 4.5 | 1.041 | 6.3 |
| **2** | 1058 | - | 2.497 | 4.5 | 1.041 | 6.4 |
| **3** | 821 | - | 2.264 | 6.2 | 1.021 | 7.5 |
| **4** | 949 | - | 2.264 | 6.2 | 1.021 | 7.9 |
| **5** | 711 | - | 2.420 | 5.3 | 1.020 | 6.2 |
| **6** | 1076 | - | 2.420 | 5.3 | 1.020 | 7.7 |
| **7** | - | 1525.6 | 2.420 | 5.2 | 1.033 | 6.1 |
| **8** | - | 1453.9 | 2.400 | 5.2 | 1.033 | 9.1 |
| **9** | - | 1482.6 | 2.408 | 5.2 | 1.033 | 7.8 |

**Oxidation Modeling: Binder Characteristics**

| *Core* | *Manufacturer* | *PG Grade* | $E_{ac}$ [e] *[kJ/mol]* | *Viscosity HS* [e] | $m_{LSV}$ [e, f] | *Initial Field CA* [e, g] |
|---|---|---|---|---|---|---|
| **1** | Valero | 70-22 | 75.2 | 3.97 | 8.14 | 0.74 |
| **2** | Valero | 70-22 | 75.2 | 3.97 | 8.14 | 0.74 |
| **3** | SemMaterial | 70-28 | 69.6 | 3.33 | 8.34 | 0.81 |
| **4** | SemMaterial | 70-28 | 69.6 | 3.33 | 8.34 | 0.81 |
| **5** | SemMaterial | 70-28 | 72.5 | 4.53 | 7.89 | 0.73 |
| **6** | SemMaterial | 70-28 | 72.5 | 4.53 | 7.89 | 0.73 |
| **7**[h] | Valero | 70-22 | 64.1 | 3.17 | 8.52 | 0.75 |
| **8**[h] | Valero | 70-22 | 65.8 | 3.96 | 7.71 | 0.72 |
| **9**[h] | Valero | 70-22 | 72.1 | 3.07 | 8.33 | 0.74 |

[a] Estimated from height and diameter (core mass not available).
[b] Cores 1–6 from mix design; cores 7–9 measured on plant loose mix.
[c] Mix design values.
[d] Cores 1–6 reported by Glover et al., 2014a; cores 7–9 calculated using measured BSG (ASTM D6752) and $G_{mm}$.
[e] Cores 1–6 reported by Jin, 2012; cores 7–9 reported by Glover et al., 2014b.
[f] Corresponds to form: Viscosity [poise] = $e^{m_{LSV}} \cdot e^{\text{Viscosity HS} \cdot \text{CA}}$
[g] Cores 1–6 are RTFO values; cores 7–9 are average values from binder extracted from construction cores.
[h] Core 7 pavement installed as HMA; core 8 pavement installed as WMA by foaming; core 9 pavement installed as WMA by adding Evotherm.

First, image pixels representing TAVs and AAVs are identified. TAV pixels are identified by thresholding—the process of adjusting a threshold value so that the fraction of pixels with values below the threshold matches the lab-measured TAV volume fraction for the whole core (see Table 3). For pavement overlays, AAV are defined as those with a connected path to the surface of the pavement (Jin, 2012). An aggressive, 26-connect scheme was employed to identify the air void pixels connected to the surface (Gonzalez et al., 2004).

After AAVs are identified, $d_{D\_AAV}$ values are determined for each core slice (Jin et al., 2013). Core slices are sections created by physically cutting the cores horizontally at vertical intervals of approximately 12.7 mm (0.5 in). The $d_{D\_AAV}$ is a function of pavement depth. Average $d_{D\_AAV}$ values are calculated for each core slice, and in keeping with previous usage these slice-average values are simply referred to as $d_{D\_AAV}$ values, unless the more specific term is necessary for clarity. To determine the $d_{D\_AAV}$ for a given core slice, the binder volume and AAV surface area for that slice are determined. Core binder volume is assumed to be evenly distributed over core height. The slice AAV surface area is determined by summing the surface area contributed by each image within the slice. The surface area contributed by each image is found by multiplying the total perimeter of the AAVs in the image by 1 mm (i.e. the height an image represents). Perimeter pixels are found using the MATLAB function *boundaries*, and lengths are calculated using the physical pixel width (approximately 0.17 mm) and standard chain code techniques (Gonzalez et al., 2004).

Calculation of the $d_{D\_TAV}$ is done by determining the surface area of the TAVs, rather than the AAVs, contributed by each image and substituting in the subsequent calculations.

**Cutting Cores into Slices, Binder Extraction, Recovery, and FTIR Testing**

After X-ray CT scanning and whole-core TAV measurements, the cores were cut horizontally into approximately 12.7 mm thick slices, binder was extracted and recovered from each slice, and FTIR CA measurements were made. Details can be found in the cited TxDOT reports and supporting literature (Glover et al., 2014a; Glover et al., 2014b; Cui et al., 2015).

**Pavement Oxidation Modeling**

Recent pavement oxidation modeling has assumed free vertical travel of oxygen through AAVs, and horizontal diffusion resistance through the asphalt adjacent to the AAVs (Prapaitrakul et al.; 2009, Jin et al., 2013). Jin et al. (2013) supply a specific embodiment of the equation of continuity to describe the oxygen concentration gradient, and consequent oxidation rate, within the asphalt adjacent to an AAV. The same model is applied in this work:

$$\frac{\partial P(x,t)}{\partial t} = \frac{\partial}{\partial x}\left(\text{fcf} \cdot D_{O_2} \frac{\partial P}{\partial x}\right) - \frac{c}{h} \cdot \frac{\partial \text{CA}(x,t)}{\partial t} \quad (18)$$

Initial Condition: No Oxygen in Binder (19)

Boundary Condition 1: Binder Adjacent to Air Void Saturated with Oxygen (20)

Boundary Condition 2: No Flux at $x = d_D$ (21)

In this equation, $P$ represents (indirectly) the oxygen concentration within the asphalt. The two independent variables are time ($t$), and position ($x$) (i.e. the distance from the air void-binder interface). The field calibration factor, fcf, is used to adjust the oxygen diffusivity ($D_{O_2}$) so that the model CA prediction for core material selected for calibration matches the measured CA value for that material. The second boundary condition identifies the maximum distance that oxygen diffuses from the interface into the binder (i.e. the $d_D$). In this work, model predictions using the two $d_D$ definitions discussed above—the $d_{D\_AAV}$ and the newly defined $d_{D\_TAV}$ — and their whole-core averages, are compared to field values.

Required asphalt binder kinetics parameters, except $M_{RTFO}$, which is estimated, have been reported, and are compiled in Table 3 (Jin, 2012; Glover et al., 2014b). The $M_{RTFO}$ value is the total possible field increase in CA due to the fast-rate reaction. Liu (1996) studied ten asphalts using POV aging after rolling thin film oven (RTFO) testing. $M_{RTFO}$ values can be calculated from the reported data, and the average value (0.16) is used in this work.

Pavement temperature profiles for each pavement location were built following the method described by Han et al. (2011).

## RESULTS AND DISCUSSION

### TAV Content, AAV Content, Diffusion Depth, and CA Variation with Depth

Figure 17 displays an x-ray CT image analysis graph and a CA data graph for each of the nine study cores. The lower right portion of the figure provides the legend for the graph

and identifies each figure with its core number. The horizontal dotted lines on each graph reflect the depths at which the cores were cut horizontally to create slices (labeled S1, S2, etc.). The image analysis graphs show TAV and AAV content variation with depth, along with the $d_{D\_TAV}$ and $d_{D\_AAV}$ values. The CA data graphs show that oxidation occurred throughout the pavement depth, even below 2 inches, in agreement with previous work (Al-Azri et al., 2006).

Figure 17 provides motivation for development of a $d_{D\_TAV}$. Excepting cores 4 and 7, TAVs and AAVs follow similar trends from the top to the bottom of each core. Cores 4 and 7 are distinct in that the AAV content falls to very low levels in the bottom two slices of each core, while TAV content displays no similar strong decline. Despite the strong decline in AAV content in cores 4 and 7, and the corresponding abnormally-large increases in the $d_{D\_AAV}$ values, there is no corresponding strong decline in CA growth. In fact, there is a relatively strong increase in the bottom slice of core 4, which seems to correspond to the TAV trend. Therefore, it appears that in general TAVs and AAVs follow a similar trend, but when they deviate, oxidation more closely follows the TAV trend. Since the influence of air void content is accounted for in the model by the $d_D$, these results indicate a $d_D$ based on TAVs may be preferred to a $d_D$ based on AAVs.

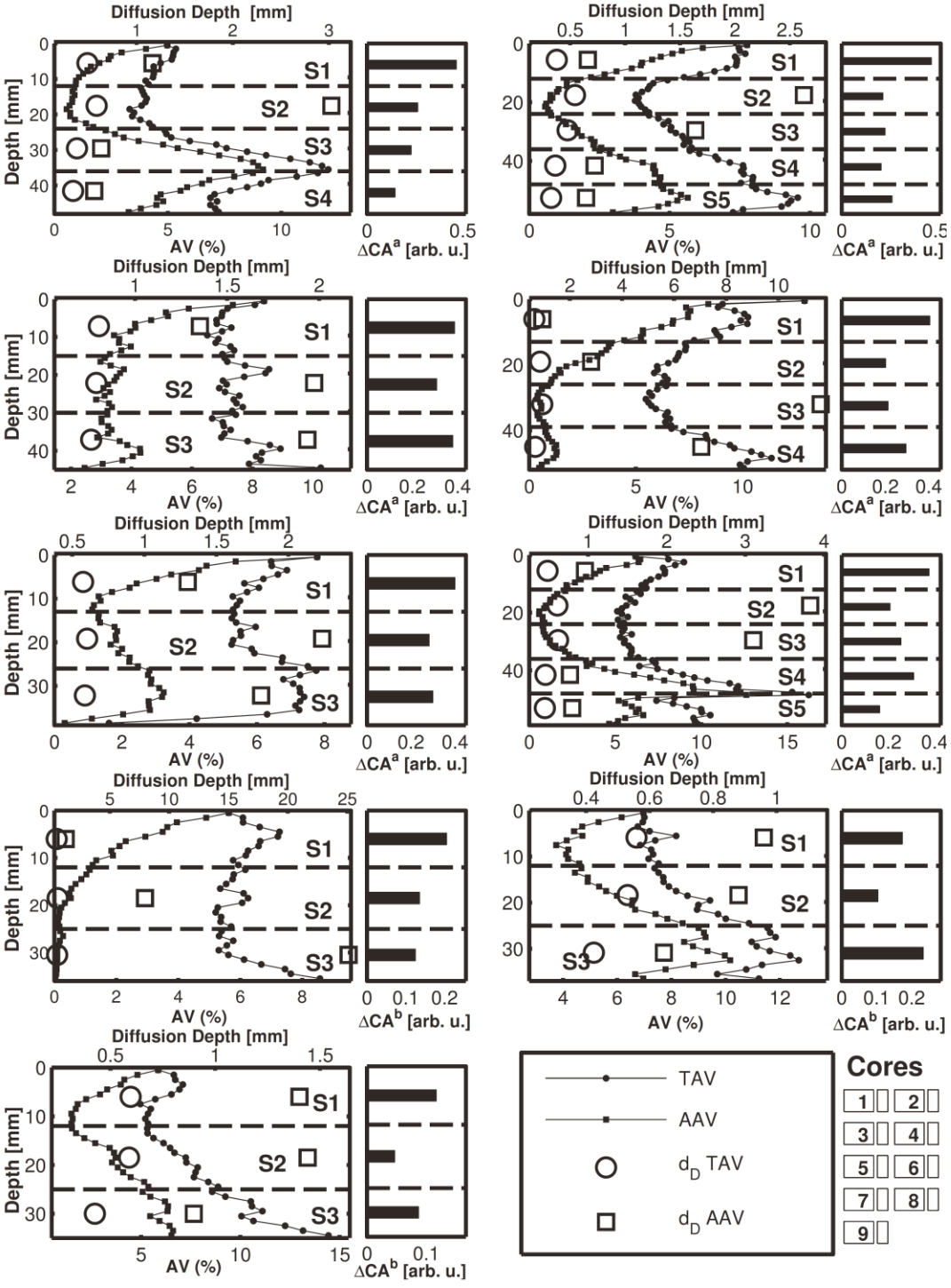


FIGURE 17 X-ray CT analysis results and field CA increase (ΔCA) for all nine cores.
[a] ΔCA = (measured – RTFO value).
[b] ΔCA = (measured – construction core value).

The above results simultaneously imply that oxygen accessibility to air voids within pavements may be greater than previously thought, and not limited to only AAVs. Oxygen must reach asphalt for oxidation to occur. Therefore, it makes sense that AAVs will influence oxidation rates while inaccessible air voids should have little effect. Yet, experimental results indicate that oxidation correlates more closely with TAV content. Possibly, oxygen is able to permeate air voids that are smaller than are detected by x-ray CT and can thereby reach practically all of the detectable air voids.

Considering Figure 17 more generally, the graphs provide continued evidence of the impact of air voids on pavement oxidation. Without air void content variation with depth, oxidation variation with depth would be expected to depend primarily on temperature variation. Specifically, oxidation would be expected to decrease with depth because of attenuated daytime temperature peaks (Han et al., 2011; Jin et al., 2011). Most of the cores (i.e. 2, 3, 4, 6, 8, and 9) actually have one or more lower slices that have oxidized more heavily than one or more respective higher slices. This makes sense because, even for field cores, it is relatively common for TAVs to show some increase with depth below the midpoint (e.g. Glover et al., 2014a). Core 4 provides a clear example. Cores 8 and 9 show strong increases in air void content with depth and a clear reflection in bottom-slice CA growth. Core 6 is particularly illustrative because there is an air void peak well below the surface and a corresponding oxidation peak in the fourth slice.

Core 1 has been retained in this study for completeness but the results appear anomalous. First, there is a strong air void peak below the surface and no corresponding

increase in CA. Second, an earlier coring (only 3-months aging) of the same pavement produced a core that actually showed slightly higher aging in the 3rd and 4th slices (Glover et al., 2014a). Third, as will be seen below, this is the only core where the model performed worse, in both cases, using slice-average $d_D$ values rather than whole-core averages. It is speculated that that the fourth slice of core 1 is partly or completely from an underlying pavement lift having different properties.

**Pavement Oxidation Modeling**

For each of the nine cores, Figure 18 shows field CA growth compared to model predictions using four $d_D$ variations: $d_{D\_TAV}$, $d_{D\_AAV}$, whole-core average $d_{D\_TAV}$, and whole-core average $d_{D\_AAV}$. For each core and $d_D$ variation, the field calibration factor (fcf) was adjusted until the predicted CA value for the second slice matched the field CA value for the second slice (within +/- 0.002). The $d_D$ values were shown Figure 17, and, for reference, numerical values, are provided in Table 4.

Figure 18 confirms that use of $d_{D\_TAV}$ values is superior to use of a $d_{D\_AAV}$ values for cores 4 and 7. Recall, from Figure 17, that cores 4 and 7 showed strong declines in AAV content with pavement depth, which resulted in abnormally large $d_{D\_AAV}$ values for the lower slices. CA growth, surprisingly, appeared to more closely follow TAV trends. Model results, shown in Figure 18, confirm this analysis. Considering core 4, results using $d_{D\_AAV}$ values heavily underestimate oxidation in slices 3 and 4, while $d_{D\_TAV}$ values perform much better, actually predicting the increase in oxidation in slice 4—a direct result of the C-shaped TAV distribution. Core 7 tells a similar story. AAV content drops heavily by slice 2 and continues to drop to almost zero in slice 3. Since the fcf is

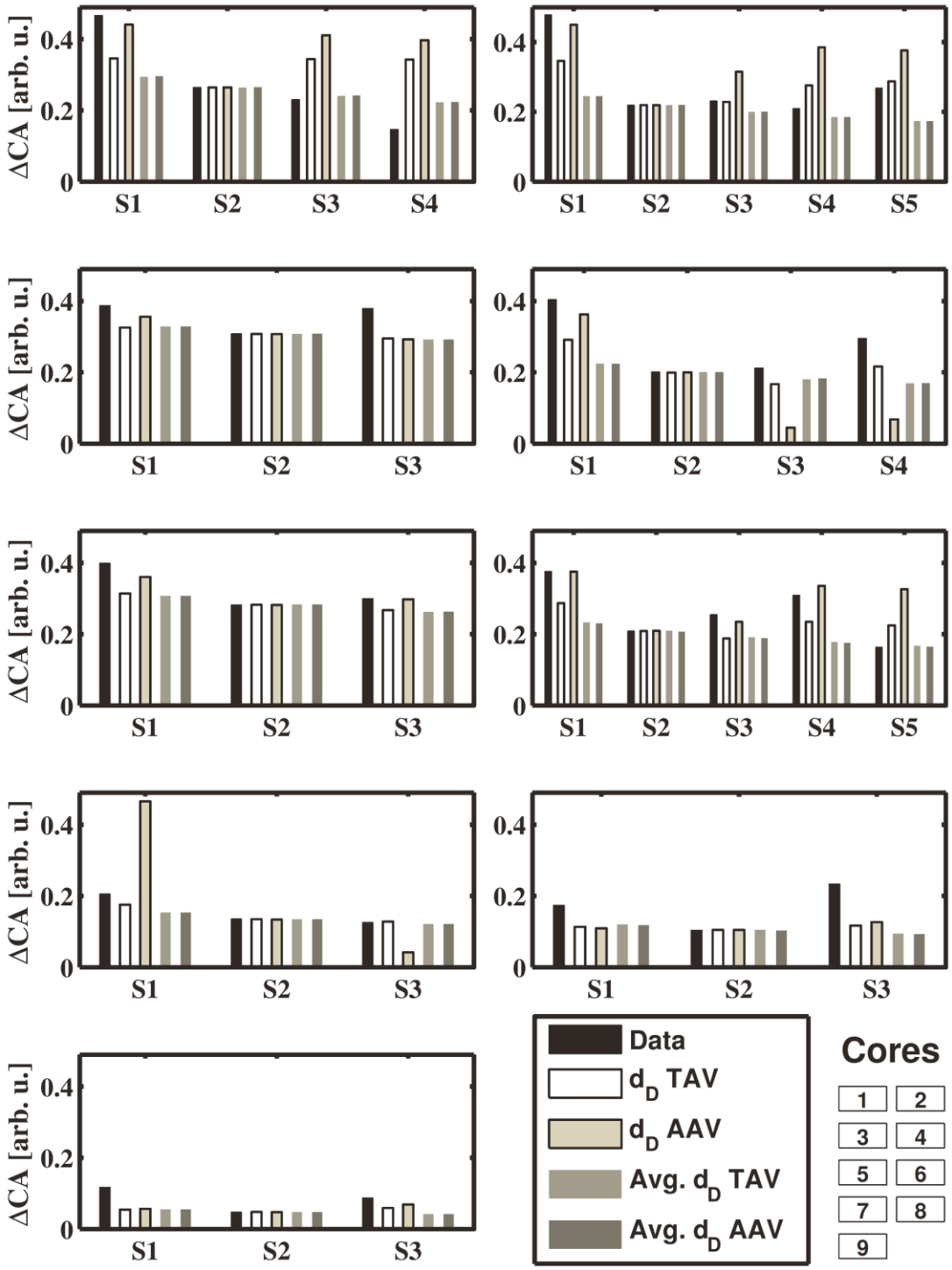


FIGURE 18 Oxidation model predictions of CA variation over pavement depth using four $d_D$ variations, compared with field data, for all nine cores.

TABLE 4

Oxidation Model Diffusion Depths, Average Errors, and Field Calibration Factor Values

**Diffusion Depths [mm]**

| | $d_{D\_TAV}$ [mm] | | | | | | $d_{D\_AAV}$ [mm] | | | | | |
|---|---|---|---|---|---|---|---|---|---|---|---|---|
| **Core** | ***S1*** | ***S2*** | ***S3*** | ***S4*** | ***S5*** | ***Avg.*** | ***S1*** | ***S2*** | ***S3*** | ***S4*** | ***S5*** | ***Avg.*** |
| **1** | 0.49 | 0.58 | 0.38 | 0.34 | - | 0.45 | 1.17 | 3.02 | 0.63 | 0.56 | - | 1.35 |
| **2** | 0.38 | 0.54 | 0.48 | 0.37 | 0.33 | 0.42 | 0.66 | 2.63 | 1.64 | 0.72 | 0.65 | 1.26 |
| **3** | 0.80 | 0.79 | 0.76 | - | - | 0.79 | 1.35 | 1.97 | 1.94 | - | - | 1.75 |
| **4** | 0.64 | 0.86 | 0.94 | 0.67 | - | 0.78 | 0.94 | 2.82 | 11.62 | 7.04 | - | 5.61 |
| **5** | 0.58 | 0.60 | 0.59 | - | - | 0.59 | 1.30 | 2.23 | 1.81 | - | - | 1.78 |
| **6** | 0.49 | 0.61 | 0.62 | 0.46 | 0.52 | 0.53 | 0.96 | 3.82 | 3.10 | 0.77 | 0.80 | 1.89 |
| **7** | 0.53 | 0.61 | 0.57 | - | - | 0.57 | 1.28 | 7.96 | 25.11 | - | - | 11.45 |
| **8** | 0.56 | 0.53 | 0.42 | - | - | 0.50 | 0.96 | 0.88 | 0.64 | - | - | 0.83 |
| **9** | 0.60 | 0.59 | 0.43 | - | - | 0.54 | 1.40 | 1.44 | 0.90 | - | - | 1.25 |

**Model Average CA Errors (abs. values) [arb. u.] and FCF Values**

| | **Average Error** | | | | **fcf Value**[a] | | | |
|---|---|---|---|---|---|---|---|---|
| **Core** | $d_{D\_TAV}$ | $d_{D\_AAV}$ | $d_{D\_TAV}$ ***Avg.*** | $d_{D\_AAV}$ ***Avg.*** | $d_{D\_TAV}$ | $d_{D\_AAV}$ | $d_{D\_TAV}$ ***Avg.*** | $d_{D\_AAV}$ ***Avg.*** |
| **1**[b] | 0.14 | 0.15 | 0.09 | 0.09 | 0.47 | 12.5 | 0.275 | 2.5 |
| **2** | 0.06 | 0.10 | 0.10 | 0.10 | 0.28 | 6.5 | 0.165 | 1.5 |
| **3** | 0.07 | 0.06 | 0.07 | 0.07 | 3.4[H] | 21 | 3.4[H] | 17 |
| **4** | 0.08 | 0.15 | 0.11 | 0.11 | 1.3 | 14 | 1.07 | 55[H] |
| **5** | 0.06 | 0.02 | 0.06 | 0.06 | 1.25 | 17 | 1.2 | 11 |
| **6** | 0.07 | 0.05 | 0.09 | 0.09 | 0.67 | 26[H] | 0.5 | 6.3 |
| **7** | 0.02 | 0.18 | 0.03 | 0.03 | 0.125 | 21 | 0.11 | 44 |
| **8** | 0.09 | 0.09 | 0.10 | 0.10 | 0.055 | 0.15 | 0.05 | 0.13 |
| **9** | 0.04 | 0.04 | 0.05 | 0.05 | 0.017[L] | 0.10[L] | 0.014[L] | 0.075[L] |
| **Avg.**[c] | **0.07** | **0.10**[d] | **0.08** | **0.08** | 0.90 | 13.16 | 0.48 | 11.78 |

[a] Optimized to satisfy: Abs. Value(Slice 2 predicted CA – Slice 2 reported CA) < 0 .002.
[b] Experimental results anomalous, see discussion.
[c] Average errors without core 1: 0.06, 0.09, 0.08, 0.08.
[d] Average error without cores 4 and 7: 0.08; average without cores 1, 4, and 7: 0.06.
[H] Designates highest fcf for $d_D$ variation.
[L] Designates lowest fcf for $d_D$ variation.

adjusted so that predicted results match slice 2 field results, the oxidation model using the $d_{D\_AAV}$ values makes a strong over prediction of the oxidation in the first slice, while

heavily under predicting oxidation in the third slice. Again, the model using $d_{D\_TAV}$ values performs much better.

For the remaining cores, TAV and AAV distributions are more closely matched, and correspondingly, model results are also closely matched, although there are some distinctions. AAV content appears to vary more strongly than TAV content. As a result, $d_{D\_AAV}$ values vary more than $d_{D\_TAV}$ values. In some cases, such as core 2, the greater variation appears to be a slight disadvantage, while in others, such as core 6, the greater variation appears to be a slight advantage. It is noted that the greater variation between the upper two slices improves prediction of surface-slice oxidation, although surface-slice oxidation is still under-predicted.

As mentioned above, predictions using two additional $d_D$ variations, a whole-core-average $d_{D\_TAV}$ and a whole-core-average $d_{D\_AAV}$, are also displayed. Since, for this average calculation, $d_D$ is constant over pavement depth, the results show the predicted effect of temperature variation on oxidation: oxidation simply decreases with depth because of attenuated daytime temperature peaks.

A numerical comparison of average errors resulting from modeling with each of the four $d_D$ variations is shown in the lower-left portion of Table 4. The average error is calculated as the average of the absolute difference between the field CA value and the predicted CA value for all of the core slices, except slice 2, which was used for field calibration. The lowest overall-average error (average of individual core averages) results from use of $d_{D\_TAV}$ values. Use of $d_{D\_AAV}$ values produces the highest overall-average error, which results from the especially large average errors for cores 1, 4, and 7

(see footnotes c and d for comparisons using alternative averages). Comparing use of $d_{D\_TAV}$ values to use of a whole-core average $d_{D\_TAV}$ values, the whole-core-average values produces a lower average error only for core 1 (the anomalous core), while usage of slice-average $d_{D\_TAV}$ values produces a lower average error for cores 2, 4, 6, 7, 8, and 9 (and cores 3 and 5 had equal errors).

Adjusted fcf values are reported in Table 4 on the lower right. Although, in general, use of $d_{D\_TAV}$ values results in fcf values closer to one than use of $d_{D\_AAV}$ values, the resulting fcf order-of-magnitude range spans are comparable. Cores 8 and 9 required particularly low fcf values; the reason is not known, but it is hypothesized that the estimated $M_{RTFO}$ value (see above) is too large for these asphalts and is playing a significant role because coring was relatively early and overall oxidation is relatively low.

**SUMMARY**

Comparison of field core air void information with core slice oxidation levels motivated the development of a $d_{D\_TAV}$, which outperformed the previously used $d_{D\_AAV}$ and whole-core average $d_D$ values. Oxidation was found to occur throughout the pavement depth, and in many cases oxidation increased with depth, which was correlated with TAV content. Comparison of TAV and AAV trends showed general similarity, resulting in similar $d_D$ trends. Two field cores stood out because AAV content dropped heavily in their lower slices, which resulted in abnormally high $d_{D\_AAV}$ values. Oxidation did not show a correspondingly strong decline and seemed to correspond better with TAV

trends. Since AAV trends and TAV trends were generally similar, and oxidation seemed to follow TAV trends when AAV and TAV trends deviated, a new $d_D$ based on TAVs was defined. Use of $d_{D\_TAV}$ and $d_{D\_AAV}$ values in an oxidation model showed that the $d_{D\_TAV}$ values resulted in much better oxidation predictions for the cores that had especially low AAV content in their lower slices. Model predictions using average diffusion depth values showed, as expected, that if air void variation is not taken into account, predicted oxidation will simply decrease with pavement depth because of attenuated daytime temperature peaks.

# CHAPTER V

# A COMPARISON OF TWO APPROACHES FOR INCORPORATING AIR VOIDS IN ASPHALT PAVEMENT OXIDATION MODELING WITH A MULTIYEAR, MULTISITE SET OF FIELD CORE DATA[*]

## INTRODUCTION

Asphalt pavement oxidation modeling predicts binder hardening with time, and provides a route to pavement life estimation (Prapaitrakul et al., 2009; Han, 2011; Jin et al., 2013; Rose et al., 2015). Asphalt oxidation produces carbonyl, quantifiable as FTIR measured carbonyl area (CA). Carbonyl area can be correlated with the DSR function, a rheological property of binder that accounts for both viscous and elastic properties, which has been further correlated with ductility (Ruan et al., 2003). Ductility, in turn, correlates with pavement failure (Clark, 1958; Doyle, 1958). More recent work has investigated the relationship between the DSR function and pavement durability (Anderson et al., 2011; King et al., 2012).

The oxidation modeling contributions referenced above are based on fundamental oxygen transport and reaction kinetics principles. The models assume sufficiently-fast, intra-air-void oxygen transport to justify approximating the oxygen partial pressure within the accessible air voids as constant (i.e. at atmospheric

[*] Part of this chapter is reprinted with permission from "A Comparison of Two Approaches for Incorporating Air Voids in Asphalt Pavement Oxidation Modeling with a Multi-year, Multi-site Set of Field Core Data" by Avery A. Rose, Yuanchen Cui, and Charles J. Glover, 2016. *Petroleum Science and Technology*, 34 (3), 223–231, Copyright 2016 by Taylor & Francis.

conditions). From the air voids, oxygen diffuses into and reacts with the binder. Asphalt reaction kinetics govern CA production rate (Jin et al., 2011).

While conceptually similar, these modeling efforts divide into two approaches for incorporating pavement air voids. One approach, termed here the cylindrical approach, models the air voids as skinny, vertical, cylindrical pores from which oxygen diffuses radially into the surrounding asphalt-aggregate matrix (Prapaitrakul et al., 2009; Han, 2011). The second, more recent approach, is termed here the diffusion depth ($d_D$) approach (Jin et al., 2013; Rose et al., 2015). A rectangular coordinate system is imposed and oxygen is modeled as simply diffusing horizontally into the asphalt, from the air voids, out to a maximum distance—the $d_D$. The $d_D$ is the average depth of a theoretical asphalt film coating the air voids, and is calculated as asphalt volume divided by air voids surface area (analogous to the concept of asphalt film thickness, which is calculated as asphalt volume divided by aggregate surface area).

In this work, the cylindrical and $d_D$ approaches are compared to each other and to field data. Binders from a multiyear, multisite set of field cores are extracted and evaluated. Recent modeling improvements are incorporated into both the cylindrical and $d_D$ approaches. The objective of this work is to compare these different modeling approaches to each other and to field oxidation data so as to better understand pavement air void distributions and their impact on oxidation and hardening rates.

## MATERIALS AND METHODS

### Materials

This study includes 22 field cores from six pavement sections. The six sections include wheel path and shoulder sections from three Texas roads. Table 5 provides construction and coring times along with relevant binder properties. Of note, final corings from US 277 and US 83 were field-aged approximately 3.5 years, and final corings from US 82 were field-aged over 2 years. These road sections were originally part of a Texas Department of Transportation (TxDOT) research study (Glover et al., 2014a; Cui, 2014; Rose et al., 2015).

### Field DSR Function Data

The field cores were cut horizontally to create 12.7 mm thick slices, and binder from each slice was extracted, recovered, and tested for DSR function (Jin et al., 2011; Cui et al., 2015). The DSR function is defined as $G'/(\eta'/G')$ measured at 15 °C, and 0.005 rad/s (Ruan et al., 2003). This function can be approximated by measuring properties at 44.7 °C and 10 rad/s and dividing the resulting function value by the frequency ratio (10/0.005) if asphalt-specific time-temperature superposition shift factors are not available. For reference, other recent work has recast the DSR function as $G^*(\cos^2\delta/\sin\delta)$ (equal to the DSR function divided by the frequency), and termed this new form the Glover-Rowe (G-R) parameter (King et al., 2012; Rowe et al., 2014).

TABLE 5
Description of Asphalt Field Cores Used in the Approach Comparison Study

**Construction and Coring**

| | | Coring Times[a] | | | |
|---|---|---|---|---|---|
| ***Section***[b] | ***Construction***[c] | ***Core 1*** | ***Core 2*** | ***Core 3*** | ***Core 4*** |
| **US 277 WP** | Apr. 2008 | Jul. 2008 | Dec. 2009 | Dec. 2010 | Jan. 2012 |
| **US 277 SH** | Apr. 2008 | Jul. 2008 | Dec. 2009 | Dec. 2010 | Jan. 2012 |
| **US 82 WP** | Jul. 2008 | Aug. 2008 | Dec. 2009 | Aug. 2010 | -- |
| **US 82 SH** | Jul. 2008 | Aug. 2008 | Dec. 2009 | Aug. 2010 | -- |
| **US 83 WP** | Jun. 2008 | Aug. 2008 | Oct. 2009 | Aug. 2010 | Nov. 2011 |
| **US 83 SH** | Jun. 2008 | Aug. 2008 | Oct. 2009 | Aug. 2010 | Nov. 2011 |

**Binder Properties and Pavement Air Voids**

| | | Viscosity-CA Relation[c,d] | | DSR Fn-CA Relation[a,e] | | |
|---|---|---|---|---|---|---|
| ***Section*** | ***Eac***[c] ***[kJ/mol]*** | ***Viscosity HS*** | ***A [Pa·s]*** | ***DSR Fn HS*** | ***A´ [MPa/s]*** | ***AV***[a] ***[%]*** |
| **US 277 WP** | 75.2 | 3.97 | 343.8 | 3.48 | $1 \cdot 10^{-5}$ | 6.3 |
| **US 277 SH** | 75.2 | 3.97 | 343.8 | 3.48 | $1 \cdot 10^{-5}$ | 6.4 |
| **US 82 WP** | 69.6 | 3.33 | 419.9 | 4.59 | $4 \cdot 10^{-6}$ | 7.5 |
| **US 82 SH** | 69.6 | 3.33 | 419.9 | 4.59 | $4 \cdot 10^{-6}$ | 7.9 |
| **US 83 WP** | 72.5 | 4.53 | 267.0 | 3.39 | $4 \cdot 10^{-6}$ | 6.2 |
| **US 83 SH** | 72.5 | 4.53 | 267.0 | 3.39 | $4 \cdot 10^{-6}$ | 7.7 |

[a]Reported by Glover et al. (2014a), US 82 values measured at the same time but not previously reported.
[b]US 277, US 82, and US 83 located in or near Laredo, TX, Lubbock, TX, and Childress, TX, respectively. The abbreviations WP and SH stand for wheel path and shoulder, respectively.
[c]Reported by Jin (2012).
[d]Corresponds to form: Viscosity [Pa·s] = $A \cdot e^{\text{Viscosity HS} \cdot CA}$.
[e]Corresponds to form: DSR Fn [MPa/s] = $A' \cdot e^{\text{DSR Fn HS} \cdot CA}$.

## Pavement Oxidation Modeling

Fundamentally, oxidation modeling requires simultaneous solution of an oxygen continuity equation and a reaction kinetics equation to determine CA growth as a function of time and distance from an asphalt-air void interface. The continuity equation describes the oxygen concentration in the asphalt (assumed to vary only with horizontal distance from the air void). The reaction kinetics equation describes the rate of production of CA as a function of oxygen concentration, temperature, and reaction kinetics parameters. Depth-specific pavement calculations are made by supplying

depth-specific pavement temperature profiles, and depth-specific boundary conditions for the continuity equation (discussed below). In this work, as done previously, for a given pavement depth, average CA predictions are reported (averaged over the oxygen path length at the pavement depth, discussed below). Average CA values are converted to DSR function values using hardening susceptibility (HS) relationships (Table 5).

The set of equations utilized by Jin et al. (2013), including fast-rate kinetics, is adopted here in a more generalized form, which allows for cylindrical or rectangular application.

*Oxygen Continuity Equation*:

$$\frac{\partial P(x,t)}{\partial t} = x^{-m} \cdot \frac{\partial}{\partial x}\left(x^{m} \cdot \text{fcf} \cdot D_{O_2} \cdot \frac{\partial P(x,t)}{\partial x}\right) - \frac{c}{h}\frac{\partial \text{CA}(x,t)}{\partial t} \quad (22)$$

Initial Condition: No Oxygen in Binder (23)

Boundary Condition 1: Binder at Binder-Air Void Interface Saturated with Oxygen (24)

Boundary Condition 2: No Oxygen Flux at Some Distance From Air Void (25)

The *m* value is zero for rectangular coordinates and 1 for cylindrical coordinates. *P* represents (indirectly) oxygen concentration in the asphalt, *t* represents time, and *x* represents distance. Specifically, for the $d_D$ approach (rectangular coordinates) *x* represents the distance from the air void-binder interface, and for the cylindrical approach (cylindrical coordinates) *x* represents the distance, in the radial direction, from

the center of the cylindrical air void pore. The fcf term is the field calibration factor (discussed below). Additional details are provided by Jin et al. (2013).

*Reaction Kinetics Equation*:

$$\frac{\partial \mathrm{CA}(x,t)}{\partial t} = M_{\mathrm{RTFO}} \cdot k_f \cdot e^{-k_f \cdot t} + k_c \quad (26)$$

Initial Condition: CA equal to $\mathrm{CA}_{\mathrm{RTFO}}$ (27)

The reaction constants $k_f$ and $k_c$ take the Arrhenius form and are functions of oxygen concentration, reaction kinetics parameters, and temperature. All of the reaction kinetics parameters can be estimated from the constant-rate activation energy (Table 5) (Jin et. al., 2011). $M_{\mathrm{RTFO}}$ represents the maximum field CA increase due to the fast-rate reaction, and as done by Rose et al. (2015), an average value of 0.16 is used. Pavement temperature profiles were built following the procedure of Han et al. (2011).

The continuity equation is used in both the cylindrical and $d_D$ approaches, but the boundary conditions are distinct, despite conceptual similarity. In the cylindrical approach the air voids are modeled as vertical, cylindrical pores from which oxygen diffuses radially (i.e. horizontally). The size and spacing of the pores is estimated using field core image analysis (next section). The average pore radius defines the location of the air void-binder interface, and half the distance between two pores defines the no flux boundary (NFB). Thus, oxygen diffuses from each pore radius to its NFB and we term this region the *pore reaction region*, which conceptually is associated with each pore but calculated as an average over the entire slice. In the $d_D$ approach the concept of an

asphalt film coating the air voids leads naturally to defining $x = 0$ to be the location of the air void-binder interface, and to defining the $d_D$ to be the no flux boundary (following prior terminology the abbreviation NFB is reserved to the cylindrical approach).

Beyond coordinate systems and physical boundary conditions, there is one key conceptual difference between the cylindrical and $d_D$ approaches, which relates to the oxygen diffusion path length. The oxygen diffusion path length is here defined, for either approach, as the distance between the air-void binder interface and the no flux boundary. The oxygen path length is expected to be shorter for the $d_D$ approach than for the cylindrical approach, because for the $d_D$ approach oxygen is modeled as diffusing through an asphalt film, whereas for the cylindrical approach diffusion is through the asphalt-aggregate matrix.

Oxygen path length differences cause fcf differences. The fcf is a model parameter that is adjusted until the model CA prediction matches the CA measured in field material that is selected for model calibration. When oxygen diffusion path lengths are shorter, as expected for the $d_D$ approach, model calibration requires reduced fcf values.

**X-ray CT Image Analysis for Determining Boundary Conditions**

Prior to cutting the second corings from each section into slices, x-ray CT images were taken and analyzed to determine the air void properties needed to define the continuity-equation boundary conditions. Images, representing horizontal core cross sections, were taken every 1 mm over the height of each imaged core (an image is

assumed to represent its corresponding 1 mm of core height). The resulting stack of 2D images is used to represent the 3D pavement core. Image analysis was performed using custom code, developed using MATLAB software; techniques build on previous work (Arambula et al., 2007; Prapaitrakul et al., 2009; Han, 2011; Jin et al., 2013). All analysis is done using TAVs as identified by x-ray CT, rather than x-ray CT identified accessible air voids (AAVs) (Rose et al., 2015). The second coring from each pavement section is assumed representative of the section for air void purposes. When another coring from the same section results in more slices than the second coring (i.e. a taller core) deeper slice air-void properties are assumed identical to the deepest slice of the second coring.

Determination of $d_D$ values is described by Rose et al. (2015). In brief, the volume of asphalt in each slice is divided by the surface area of the TAVs in the corresponding slice to determine an average asphalt coating thickness—the $d_D$.

Boundary condition determination for the cylindrical approach is intended to follow the techniques described by Han (2011) (excepting of the use of TAVs rather than AAVs, and the use of a single, average, air void radius as done by Prapaitrakul et al. (2009)); to reduce uncertainty, and for convenience, methods are overviewed.

First, a cylindrical average pore radius for each slice is defined and determined. The concept of a radius is not directly applicable because air void cross sections (seen in 2D images) are not, in general, circular. As an approximation, the radius of an air void is defined as the radius of a circle that has an area equal to the air void (Arambula et al., 2007). With this definition, the average air void radius in each image is determined from

the individual air voids in the image. The image-average values are used to determine an overall average air void radius for each slice.

The radial location of the NFB for each slice must also be determined. The approach assumes the cylindrical air void pores are equally spaced and surrounded concentrically by a pore reaction region, the outermost point being the NFB, whose position (relative to the center of the pore) is calculated as:

$$\text{NFB} = \left(\frac{\text{Core Cross Sectional Area}}{\text{Average Number of Air Voids in Slice} \cdot \pi}\right)^{0.5} \quad (28)$$

This calculation relies on the assumption that the total cross sectional area of cylinders defined by the NFBs is equal to the cross sectional area of the core.

## RESULTS AND DISCUSSION

### Pore Radii, Pore Reaction Regions, $d_D$ Values, and fcf Values

Figure 19 shows slice-specific average pore radii, pore reaction regions, and $d_D$ values, as well as fcf values for each of the six study sections. Slices are designated S1, S2, etc. The pore radii bars are stacked with the pore reaction regions to indicate visually that, for the cylindrical approach, the oxygen diffusion path is through the pore reaction region from the pore wall to the NFB (e.g. the US 277 S1 average pore radius is 310 µm and the NFB is 1840 µm, therefore the reaction region extends from 310 to 1840 µm). Diffusion depth values are represented by a single dark bar, indicating that for the $d_D$

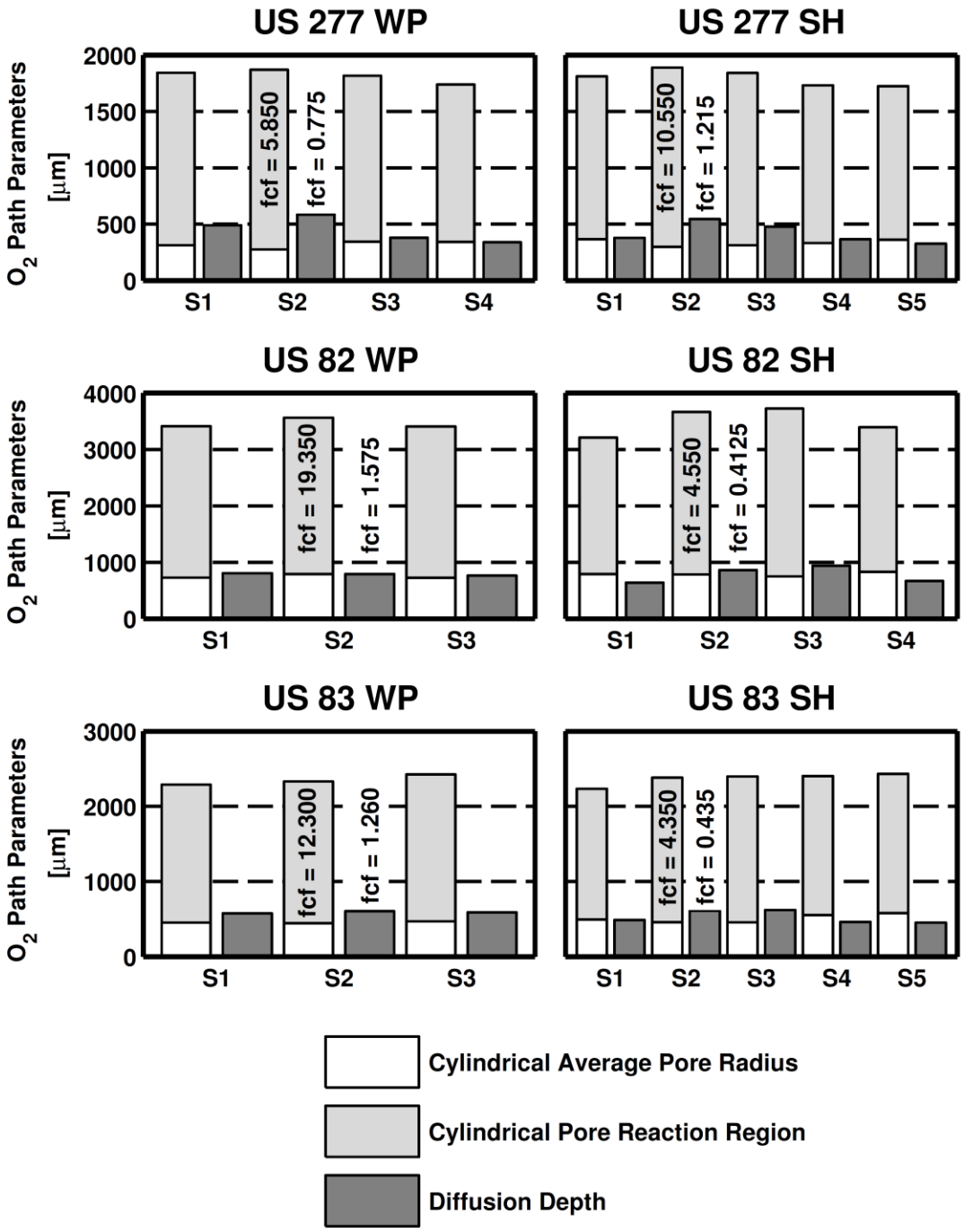


FIGURE 19 Pore radii, pore reaction regions, diffusion depths, and fcf values. Based on the second coring for each pavement section. Fcf determination based on DSR function measurements, except for US 83 WP for which calibration was based on CA measurements. Fcf values optimized using MATLAB function *fminsearch* to satisfy: abs. value (slice 2 predicted CA – Slice 2 field CA) < 0.001.

approach the diffusion path is from $x = 0$, the air void-asphalt interface, to the $d_D$. Guided by previous work, the models are calibrated using material from the second slice of each representative core; resulting fcf values are placed above the corresponding bars (Jin et al., 2013; Rose et al., 2015). Comparison of the fcf values with theory is discussed below and suggests that oxygen path lengths determined following the $d_D$ approach may be more reasonable than those determined using the cylindrical approach.

As expected, cylindrical approach diffusion paths are longer than $d_D$ paths and as a result cylindrical approach fcf values are larger than $d_D$ fcf values. Cylindrical model diffusion path lengths are in the neighborhood of 1500, 2500, and 2000 μm, for US 277, US 82, and US 83 respectively, while $d_D$ path lengths (i.e. the $d_D$ values) are always less than 1000 μm. Shorter $d_D$ path lengths spotlight the use of an asphalt (rather than asphalt-aggregate matrix) volume in the $d_D$ calculation. Wheel path and shoulder differences appear less significant than roadway differences. Cylindrical approach fcf values range from approximately 4–19, while $d_D$ approach fcf values range from approximately 0.4–1.6.

While it is not surprising that cylindrical approach fcf values are larger than $d_D$ fcf values, theory, possibly surprisingly, predicts fcf values closer to the $d_D$ fcf values, indicating the $d_D$ approach results in more realistic oxygen path lengths. Jin et al. (2013) introduced the fcf to account for factors not considered by their model (they proffered oxygen path tortuosity, micro crack development, and asphalt absorption by aggregate), and stated that the fcf could be more or less than unity. Prior to the work of Jin et al.

(2013), Prapaitrakul et al. (2009) suggested calculation of an effective oxygen diffusivity using the following theoretical form:

$$D_e = \frac{\epsilon}{\tau} \cdot D_{O_2} \tag{29}$$

where $D_e$ is the effective diffusivity, $\varepsilon$ is the asphalt volume fraction, and $\tau$ is the tortuosity. The effective diffusivity is intended to relate the oxygen flux through the asphalt-aggregate matrix to the oxygen concentration gradient in the asphalt material within the matrix. As discussed in Chapter I, use of this form in the cylindrical approach (recall that the oxygen flux is through the asphalt-aggregate matrix) results in a $1 / \tau$ term remaining in front of the oxygen diffusivity term. The asphalt volume fraction, $\varepsilon$, is canceled when the continuity equation is divided by the asphalt volume fraction to relate the other terms in the equation to an asphalt volume basis. The remaining term, $1/ \tau$, could be thought of as providing an ideal value for the fcf. Since the tortuosity is greater than unity, the term $1 / \tau$ is less than unity, which corresponds better to the fcf values determined using the $d_D$ approach.

Better agreement of the $d_D$ fcf values with theory could indicate the presence of smaller air voids that were undetected by x-ray CT, in agreement with the work of Rose et al. (2015). Rose et al. (2015) hypothesized that there may be significant networks of air voids that are too small to be detected by x-ray CT (resolution in that work, and the work reported herein, yields pixel widths of approximately 0.2 mm), but that nonetheless provide passageways for oxygen. Assuming this is true, the air void size distribution

would be shifted towards smaller air voids (the TAV volume fraction is separately measured for image thresholding). Higher numbers of smaller air voids replacing fewer larger air voids would reduce air void spacing, and hence NFBs in the cylindrical approach, and in the $d_D$ approach would result in greater air void surface area thereby reducing the $d_D$ values. Ultimately fcf values for both approaches would be reduced, possibly resulting in cylindrical approach fcf values closer to theory.

**Field Data and Model Predictions**

Figure 20 shows field data and model results in terms of both DSR function and CA (for reference, DSR function values [MPa/s] can be converted to G-R parameter values [kPa] by multiplying by $2 \cdot 10^5$). Within each section, corings are designated C1, C2, etc. For each coring, results for the $d_D$ modeling approach, the cylindrical modeling approach, and for field data are distinguished by marker shading. The field data come from measured DSR function values (excepting the RTFO values, which come from measured CA values). The CA scale on the secondary ordinate axis is defined by the DSR function HS relationship (Table 5). Wherever deeper-slice data markers overlap with shallower-slice data markers the deeper-slice markers are shifted slightly to the right for better visibility.

Considering the field data (clear markers), DSR function values generally increase with time for all sections, as expected, but final DSR function values for the US 83 sections are lower than the corresponding values for the US 277 and US 82 sections. Lower initial DSR function values contribute, but DSR function values are also

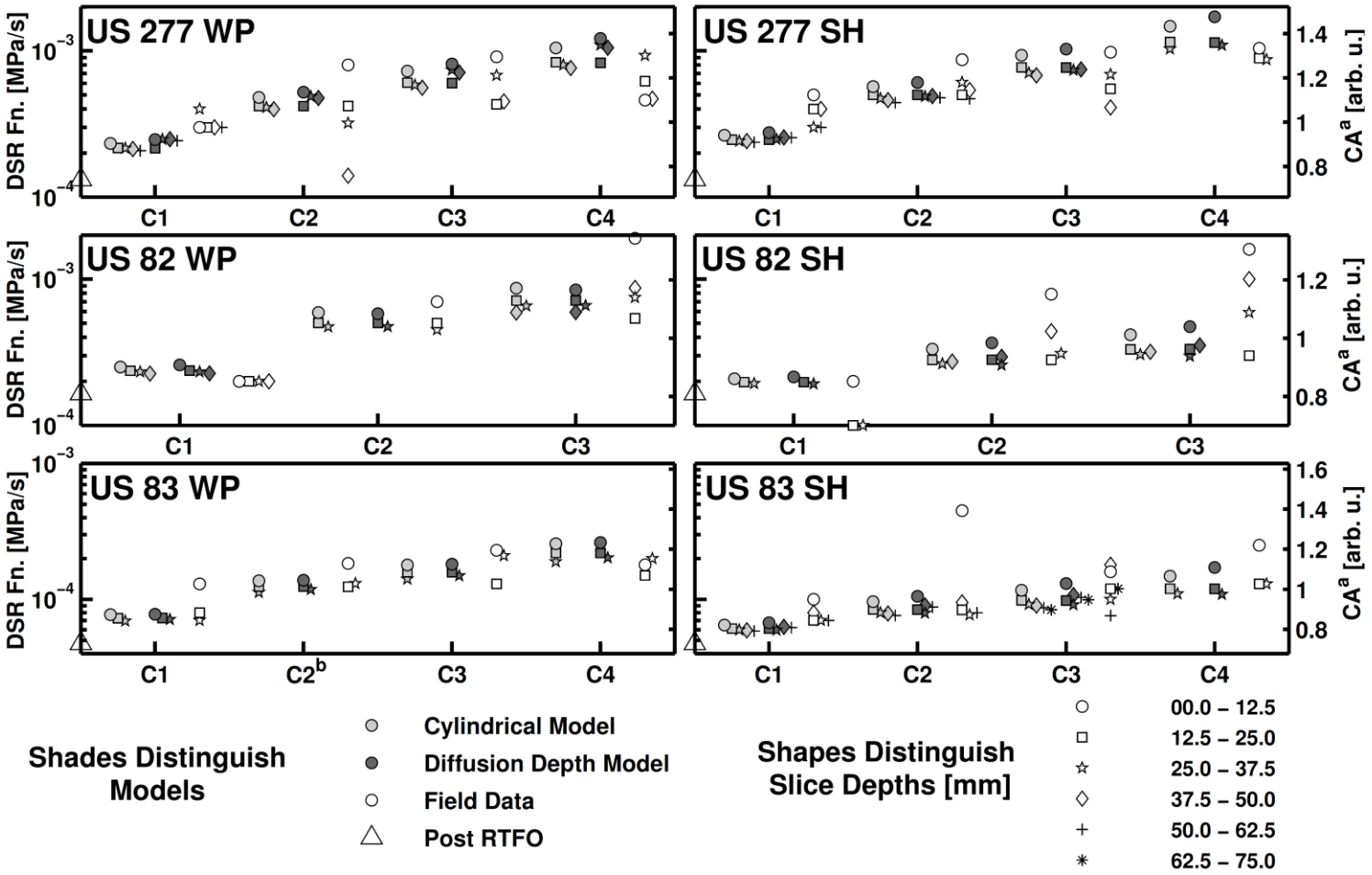


FIGURE 20 Model predictions of DSR function and CA compared with field data. All field data based on measured DSR function values, except RTFO values and the values for US 83 WP core 2, which are based on measured CA values. [a]CA scale based on DSR function hardening susceptibility relationship. [b]Field data based on measured CA values, as noted.

increasing more slowly for these cores. In part this can be explained by US 83 having the highest viscosity HS and yet the lowest DSR function HS (see Table 5). Due to high viscosity HS, produced CA causes a relatively rapid viscosity increase, which decreases oxygen diffusivity and thereby retards oxidation rate. Concomitantly, a lower DSR function HS means CA produced causes a relatively small increase in DSR function.

Further considering the field data, the importance of oxygen path length variation with pavement depth is evident. As discussed briefly above, oxidation variation with pavement depth is expected to be influenced primarily by temperature variation and oxygen path length variation (resulting largely from air void fraction variation). Daytime pavement temperature peaks are attenuated with depth, resulting in reduced oxidation with depth (Rose et al., 2015). However, air void volume fraction can increase with depth (Glover et al., 2014a, appendix F), resulting in reduced oxygen diffusion path lengths and increased oxidation. Each study section provides examples of deeper slices that are more heavily aged than respective shallower slices. To see an example, notice that squares represent the second slice, stars the third slice, and diamonds the fourth slice, and look at US 82 SH corings 2 and 3 where both the star and the diamond are above the square (other field data where a star or diamond is above a square: US 277 WP C1, C3, C4; US 277 SH C2, C3; US 82 WP C3; US 83 WP C2, C3, C4; US 83 SH C1, C2, C3).

Comparison of the model predictions with the field data indicates that the $d_D$ approach is better able to account for the coupled effects of temperature and oxygen path length variation with pavement depth. The cylindrical approach tends not to predict any

increase in aging with pavement depth; the $d_D$ approach produces several examples where a deeper slice is predicted to age more than a respective shallower slice. Section US 83 SH provides a clear example; for corings 1, 2, and 3 the forth slice aged more heavily than the second slice, and the $d_D$ approach accurately predicts this, but the cylindrical approach simply predicts a decrease in aging with pavement depth for all slices. Similarly, section US 277 WP corings 1, 3, and 4 all show higher aging in the third slice than in the second slice, which is predicted by the $d_D$ approach (the data for coring two appear anomalous, the fourth slice being a clear outlier).

## SUMMARY

Cylindrical and $d_D$ oxidation modeling approaches were compared with data collected from a multiyear, multisite set of field cores. Conceptually similar, the approaches differ in the way they account for air voids, i.e. how the boundary conditions in the oxygen continuity equation are specified. Recent modeling improvements (fast-rate kinetics, the assumption of TAV accessibility, and fcf usage) were incorporated in both approaches. The $d_D$ approach results in fcf values that are closer to theory. The $d_D$ approach also has superior ability to predict aging variation with pavement depth, indicating better accounting of the coupled effects of temperature and air void variation with pavement depth. The results indicate that future modeling efforts could benefit from an air void analysis technique that accounts for air voids that are undetectable by current x-ray CT methods. Improved x-ray CT resolution could provide additional understanding of these results and of air void distributions in pavements.

# CHAPTER VI

# CONCLUSIONS AND RECOMMENDATIONS FOR FUTURE WORK

Pavement oxidation modeling is intended to predict in-field pavement aging, or, more specifically, binder oxidation and rheological hardening. Previous modeling efforts laid a framework and, in doing so, indicated that the effect of pavement air voids is an important factor. The work reported herein built on previous work and investigated measurement of pavement air void properties and incorporation of pavement air void properties in oxidation modeling.

As a first step, a method was developed for analyzing x-ray CT images of pavement cores using MATLAB software. The method follows previously documented techniques and permits determination of the air void properties required for oxidation modeling. The method is sufficiently flexible to permit determination of modified, and additional, air void properties.

The x-ray CT image analysis method was applied in three studies. Specific conclusions from each study and overall conclusions are reviewed below. Based upon the insights gained, recommendations for future research are provided.

## CONCLUSIONS

In a first study, a method for measuring total air void (TAV) volume fraction variation with pavement depth was developed, and the method was validated using x-ray CT image analysis. Although validated by x-ray CT, the method relies on only conventional

testing equipment and thereby provides a means for asphalt testing laboratories to measure air void variation with pavement depth. As discussed below, this result suggests a path away from reliance on x-ray CT for oxidation modeling. As part of this work, it was determined that a vacuum dryer can be used to reduce testing time without oxidizing the binder by an amount that would prevent further testing.

In a second study, a comparison of TAVs, x-ray CT identified accessible air voids (AAVs), and oxidation in nine field cores led to the development of a revised diffusion depth ($d_D$) definition based on TAVs. Previous work assumed that the air voids that are accessible to oxygen could be identified by analysis of x-ray CT images. This work showed that generally TAV fraction and AAV fraction follow the same trend with pavement depth, but when they deviate oxidation appears to follow the TAV trend. This experimental evidence suggested a revised $d_D$ based on total air voids. Oxidation modeling using the revised definition produced superior overall predictions. It was hypothesized that a network of smaller air voids, not detected using x-ray CT, provide passageways for oxygen molecules. As part of the same study, the expected decrease in oxidation with pavement depth due to temperature variation alone was investigated using whole-core-average $d_D$ values.

In a third study, a comparison of the cylindrical and $d_D$ modeling approaches with a multiyear, multisite set of field data revealed that the $d_D$ approach results in field calibration factor (fcf) values closer to theory and is better able to account for oxidation variation with pavement depth. The cylindrical approach assumes oxygen diffuses radially (i.e. horizontally), from vertically oriented air void cylinders, through the asphalt

matrix. The $d_D$ approach also assumes horizontal oxygen diffusion, but that diffusion is through a theoretical asphalt layer abutting the air voids, which has a thickness, termed the $d_D$, defined as the asphalt volume divided by the air void surface area. Possibly surprisingly, modeling using the $d_D$ approach resulted in fcf values closer to theory. Additionally, the $d_D$ approach was better able to incorporate the coupled effects of air void variation and pavement temperature variation with pavement depth, which was evidenced by superior ability to predict oxidation variation with pavement depth. These results could indicate the presence of undetected smaller air voids as hypothesized in the second study.

Overall, in addition to improving the current understanding of pavement air void properties and their measurement, this work improved the current understanding of the relationship between pavement air void properties and pavement aging. This work adds to the mounting evidence that asphalt within pavement oxidizes continuously (i.e. over the entire pavement life) throughout the pavement depth. Oxidation rate variation with pavement depth is influenced by pavement temperature and air void properties. Total air void and x-ray CT-identified AAV fractions vary with pavement depth. Also, daytime temperature peaks attenuate with pavement depth. Depth attenuation of daytime temperature peaks coupled with the non-linear effect of temperature on carbonyl production rate tends to result in slower oxidation rates at greater pavement depths. Air void fraction, on the other hand, can, and often does, increase with pavement depth, which tends to increase oxidation rates at greater pavement depths. Field data reveal that is not uncommon for the effect of increasing air void fraction with depth to partially

overcome the effect of attenuated temperature peaks, resulting in deeper asphalt portions being more heavily oxidized than some, respective, shallower portions.

Furthermore, this work provides an improved and simplified approach for incorporating air void properties in oxidation modeling. As mentioned above, field data indicate that pavement oxidation relates more closely to TAVs than to x-ray CT identified AAVs. It is hypothesized that nearly all air voids are accessibly to oxygen being connected by networks of air voids too small to detect using x-ray CT. This hypothesis is further supported by modeling results showing that the $d_D$ approach requires fcf values that are closer to theory and is better able to predict oxidation variation with pavement depth. Taken together, these studies provide evidence that, in general, oxidation modeling based on TAVs is preferred to modeling based on x-ray CT identified AAVs (e.g. a $d_{D\_TAV}$ is preferred to an $d_{D\_AAV}$). In addition to providing superior overall results, modeling based on TAVs is simpler because there is no longer a need to distinguish AAVs. A preference for modeling based on TAVs also represents a second step away from reliance on x-ray CT since it was already shown that TAVs can be measured using conventional volumetric techniques.

## RECOMMENDATIONS FOR FUTURE WORK

The following future work is recommended:

1. Obtain field cores from a pavement aged approximately to the point of failure (see DSR function failure limit discussion in Chapter I) and study the ability of oxidation modeling to predict the final state of the binder. Ideally, these

cores would come from a road that had been previously cored and studied so that a model's ability to predict the evolution of the binder aging state with time could be evaluated. Studies of whole core trends, in addition to more detailed slice-by-slice studies, may be instructive.

2. Improve upon the current oxidation modeling approaches by incorporating an oxygen diffusion flux into the asphalt at the pavement surface. The current models assume that oxygen travels vertically through the air voids and diffuses horizontally in the asphalt. Oxygen can also diffuse directly into the asphalt at the pavement surface. Additionally, daytime temperature peaks are highest at the pavement surface, which causes faster oxidation rates at the surface.

3. Image cores or core portions using a higher resolution x-ray CT machine and investigate air voids properties, in particular air void size distributions.

4. Work toward a means for determining the oxygen continuity equation boundary condition values (i.e. $d_D$ values or pore radius and no flux boundary values) without the need for x-ray CT. The work reported herein showed that TAV fraction variation with pavement depth can be measured using standard asphalt laboratory equipment. It was further shown that basing oxidation modeling on TAVs is preferred to basing modeling on x-ray CT identified AAVs. There remains a need to connect the TAV fraction to the required oxygen continuity equation boundary condition values without the use of x-ray CT. One approach is to attempt to relate mixture properties to air void size distributions

and then use the air void size distributions to estimate the required boundary condition values. The method of Luo and Lytton (2011) could be used to determine air void size distributions that account for air voids below x-ray CT resolution limits. This approach combines x-ray CT with a repeated direct tension test to determine more realistic air void size distributions than those determined directly from x-ray CT images (Luo and Lytton, 2011).

5. Incorporate air void variation with time into oxidation modeling. Air void fraction may decrease because of traffic loading and may increase because of cracking. Furthermore, air voids may tend to coalesce as pavement ages thereby changing air void size distributions.

## REFERENCES


AASHTO Standard T166. (2005). *Bulk Specific Gravity of Compacted Bituminous Mixtures Using Saturated Surface Dry Specimens*. Washington D.C: American Association of State Highway and Transportation Officials.

Al-Azri, N. A., Jung, S. H., Lunsford, K. M., Ferry, A., Bullin, J. A., Davison, R. R., and Glover C. J. (2006). Binder oxidative aging in Texas pavements: hardening rates, hardening susceptibilities, and impact of pavement depth. *Transportation Research Record: Journal of the Transportation Research Board* 1962:12–20.

Alvarez, A. E., Martin, A. E., Estakhri, C. (2009). Connected air voids content in permeable friction course mixtures. *Journal of Testing and Evaluation* 37:254–263.

Anderson, R. M., King, G. N., Hanson, D. I., and Blankenship, P. B. (2011). Evaluation of the relationship between asphalt binder properties and non-load related cracking. *Journal of the Association of Asphalt Paving Technologists* 80:615–664.

Arambula, E., Masad, E., Martin, A. E. (2007). Influence of air void distribution on moisture susceptibility of asphalt mixes. *Journal of Materials in Civil Engineering* 19:655–664.

Asphalt Institute. (1994). *SuperPave performance graded asphalt binder specification and testing*. Superpave Series No. 1 (SP–1). Lexington, Kentucky: Asphalt Institute.

ASTM Standard D2041. (2011). *Standard test method for theoretical maximum specific gravity and density of bituminous paving mixtures*. West Conshohocken,

Pennsylvania: ASTM International. DOI: 10.1520/D2041_D2041M-11, www.astm.org.

ASTM Standard D2872. (2012). *Standard test method for effect of heat and air on a moving film of asphalt (rolling thin-film oven test)*. West Conshohocken, Pennsylvania: ASTM International. DOI: 10.1520/D2872–12E01, www.astm.org.

ASTM Standard D3203. (2005). *Standard test method for percent air voids in compacted dense and open bituminous paving mixtures*. West Conshohocken, Pennsylvania: ASTM International. DOI: 10:1520/D3202-05, www.astm.org.

ASTM Standard D4121. (2009). *Standard test method for separation of asphalt into four fractions*. West Conshohocken, Pennsylvania: ASTM International. DOI: 10.1520/D4124-09, www.astm.org.

ASTM Standard D6752. (2011). *Standard test method for bulk specific gravity and density of compacted bituminous mixtures using automatic vacuum sealing method*. West Conshohocken, Pennsylvania: ASTM International. DOI: 10.1520/D6752_D6752M-11, www.astm.org.

ASTM Standard D6857. (2011). *Standard test method for maximum specific gravity and density of bituminous paving mixtures using automatic vacuum sealing method*. West Conshohocken: Pennsylvania: ASTM International. DOI: 10.1520/D6857_D6857M-11, www.astm.org.

ASTM Standard D7063, 2011, *Standard Test Method for Effective Porosity and Effective Air Voids of Compacted Bituminous Paving Mixture Samples*, ASTM

International, West Conshohocken, Pennsylvania, 2011, DOI: 10.1520/D7063_ D7063M-11, www.astm.org.

Boduszynski, M. M. (1981). Asphaltenes in petroleum asphalts: composition and formation. In *Chemistry of asphaltenes*, advancement in chemistry series 195 edited by J. W. Bunger, and N. C. Li, pp. 120–135. Washington, D.C.: American Chemical Society.

Burr B. L., Davison, R. R., Glover C. J., Bullin J. A. (1990). Solvent removal from asphalt. *Transportation Research Record: Journal of the Transportation Research Board* 1269:1–8.

Burr B. L., Davison R. R., Jemison H. B., Glover C. J., Bullin J. A. (1991). Asphalt hardening in extraction solvents. *Transportation Research Record: Journal of the Transportation Research Board* 1323:70–76.

Burr B. L., Glover C. J., Davision R. R., Bullin J. A. (1993). New apparatus and procedure for the extraction and recovery of asphalt binder from pavement mixtures. *Transportation Research Record: Journal of the Transportation Research Board* 1391:20–29.

Burr B. L., Davison R. R, Glover C. J., Bullin J. A. (1994). Softening of asphalts in dilute solutions at primary distillation conditions. *Transportation Research Record: Journal of the Transportation Research Board* 1436:47–53.

Chehab, G. R., O'Quinn, E. and Kim, Y. R. (2000). Specimen geometry study for direct tension test based on mechanical tests and air void variation in SGC-compacted

asphalt concrete specimens. *Transportation Research Record: Journal of the Transportation Research Board* 1723:125–132.

Cipione C. A., Davison R. R., Burr B. L., Glover C. J., Bullin J. A. (1991). Evaluation of solvents for the extraction of residual asphalt from aggregates. *Transportation Research Record: Journal of the Transportation Research Board* 1323:47–52.

Clark, R. C. (1958). Practical results of asphalt hardening on pavement life. In *Association of Asphalt Paving Technologists* 27:196–208.

Cui, Y. (2014). *Exploration of Pavement Oxidation Model Applications and Field Validation*. Ph.D. dissertation. College Station, Texas: Texas A&M University.

Cui, Y., Jin, X., Liu, G., and Glover, C. J. (2015). An oxidative aging study of seal coat treated pavement. *Petroleum Science and Technology* 33:23–30.

Das, P. K., Kringos, N., and Birgisson, B. (2014). Numerical study on the effect of mixture morphology on long-term asphalt mixture aging. *International Journal of Pavement Engineering* ahead-of-print:1–11.

De, S. (2010). *Shrinkwrap*. MATLAB Central, File Exchange, updated 08 Feb 2011. http://www.mathworks.com/matlabcentral/fileexchange/29175-shrinkwrap.

Deen, W. M. (2012). *Analysis of transport phenomena*. 2nd ed. New York, New York: Oxford University Press.

Dickinson, E. J. (1984). The diffusion controlled reaction of oxygen with films of bituminous binders. *Australian Road Research* 14:121–132.

Domke, C., Davison, R. R., and Glover, C. J. (1999). Effect of oxidation pressure on asphalt hardening susceptibility. *Transportation Research Record: Journal of the Transportation Research Board* 1661:114–121.

Doyle, P. C. (1958). Cracking characteristics of asphalt cement. *Proceedings of the Association of Asphalt Paving Technologists* 27:581–597.

Geankoplis, C. J. (1993). *Transport processes and unit operations*. 3rd ed. Englewood Cliffs, New Jersey: P T R Prentice-Hall, Inc.

Glover, C. J., Han, R., Jin, X., Prapaitrakul, N., Cui, Y., Rose, A., Lawrence, J. J., Padigala, M., Arambula, E., Park, E. S., and Martin, A. E. (2014a). *Evaluation of binder aging and its influence in aging of hot mix asphalt concrete.* Publication FHWA/TX-14/0-6009-2. College Station, Texas: Texas Transportation Institute, Texas A&M University System.

Glover, C. J., Liu, G., Rose, A. A., Tong, Y., Gu, F., Ling, M., Arambula, E., Estakhri, C., Lytton, R. (2014b). *Evaluate Binder and Mixture Aging for Warm Mix Asphalt: Technical Report*. Publication FHWA/TX-13/0-6613. College Station, Texas: Texas Transportation Institute, Texas A&M University System.

Gonzalez, R. C., Woods, R. E., and Eddins, S. L. (2004). *Digital image processing using MATLAB.* Upper Saddle River, New Jersey: Pearson Education, Inc.

Halstead, W. J. (1963). The relation of asphalt ductility to pavement performance. *In Association of Asphalt Paving Technologists* 32:247–270.

Han, R. (2011). *Improvement to a transport model of asphalt binder oxidation in pavements: pavement temperature modeling, oxygen diffusivity in asphalt binders*

*and mastics, and pavement air void characterization*. Ph.D. dissertation. College Station, Texas: Texas A&M University.

Han, R., Jin, X., and Glover, C. J. (2011). Modeling pavement temperature history for use in binder oxidation models and pavement performance prediction. *Journal of Materials in Civil Engineering* 23:351–359.

Instrotek Incorporated. (2010). *Coredry operator's guide*, version 7. Raleigh, North Carolina: Instrotek Incorporated.

Jemison, H. B., Burr, B. L., Davison, R. R., Bullin, J. A., and Glover, C. J. (1992) Application and use of the ATR, FT-IR method to asphalt aging studies. *Fuel Science and Technology International* 10:795–808.

Jin, X. (2012). *Asphalt Oxidation Kinetics and Pavement Oxidation Modeling*. Ph.D. dissertation. College Station, Texas: Texas A&M University.

Jin, X., Han, R., Cui, Y., and Glover, C. J. (2011). Fast-rate–constant-rate oxidation kinetics model for asphalt binders. *Industrial and Engineering Chemistry Research* 50:13373–13379.

Jin, X., Cui, Y., and Glover, C. J. (2013). Modeling asphalt oxidation in pavement with field validation. *Petroleum Science and Technology* 31:1398–1405.

Juristyarini, P., Davison, R. R., and Glover, C. J. (2011a). Oxidation hardening kinetics of the rheological function G′/(η′/G′) in asphalts. *Petroleum Science and Technology* 29:2027–2036.

Juristyarini, P., Davison, R. R., and Glover, C. J. (2011b). Development of an asphalt aging procedure to assess long-term binder performance. *Petroleum Science and Technology* 29:2258–2268.

Kandhal, P. S. (1977). Low-temperature ductility in relation to pavement performance. *ASTM STP* 628:95–106.

King, G. N., Anderson, R. M., Hanson, D. I., and Blankenship, P. B. (2012). Using black space diagrams to predict age-induced cracking. In *7th RILEM International Conference on Cracking in Pavements*, pp. 453–463. Springer, Netherlands.

Lau C. K., Lunsford, K. M., Glover C. J., Davison, R. R., and Bullin, J. A. (1992). Reaction rates and hardening susceptibilities as determined from POV aging of asphalts. *Transportation Research Record: Journal of the Transportation Research Board* 1342:50–57.

Lin, M. S., Lunsford, K. M., Glover, C. J., Davison, R. R., and Bullin, J. A. (1995). The effects of asphaltenes on the chemical and physical characteristics of asphalt. In *Asphaltenes*, pp. 155–176. Springer, US.

Liu, M., Lunsford, K. M., Davison, R. R., Glover, C. J., and Bullin, J. A. (1996). The kinetics of carbonyl formation in asphalt. *AIChE Journal*, 42:1069–1076.

Liu, M., Ferry, M. A., Davison, R. R., Glover, C. J., and Bullin, J. A. (1998). Oxygen uptake as correlated to carbonyl growth in aged asphalts and asphalt Corbett fractions. *Industrial and Engineering Chemistry Research* 37:4669–4674.

Liu, M. (1996). *The effects of asphalt fractional compositions on properties*. Ph.D. dissertation. College Station, Texas: Texas A&M University.

Lundsford, K. M. (1994). *The effect of temperature and pressure on laboratory oxidized asphalt films with comparison to field aging*. Ph.D. dissertation. College Station, Texas: Texas A&M University.

Luo, R., and Lytton, R.L. (2011). Determination of crack size distribution in asphalt mixtures. *Transportation Research Record: Journal of the Transportation Research Board* 2210:113–121.

Mannini, Alessandro. (2010). *Freeman Chain Code*. MATLAB Central, File Exchange. http://www.mathworks.com/matlabcentral/fileexchange/29175-shrinkwrap.

Masad, E., Muhunthan, B., Shashidhar N., and Harman, T. (1999). Internal structure characterization of asphalt concrete using image analysis. *Journal of Computing in Civil Engineering* 13:88–95.

Masad, E, Jandhyala V. K., Dasgupta, N., Somadevan, N., and Shashidhar, N. (2002). Characterization of air void distribution in asphalt mixes using x-ray computed tomography. *Journal of Materials in Civil Engineering* 14:122–129.

Prapaitrakul, N. (2009). *Toward an improved model of asphalt binder oxidation in pavements*. Ph.D. dissertation. College Station, Texas: Texas A&M University.

Prapaitrakul, N., Han, R., Jin, X., and Glover, C. J. (2009). A transport model of asphalt binder oxidation in pavements. *Road Materials and Pavement Design* 10: 95-113.

Roberts, F. L., Kandhal, P. S., Brown E. R., Lee, D. Y., Kennedy, T. W. (1996). *Hot mix asphalt materials, mixture, design, and construction*. 2nd ed. Lanham, Maryland: NAPA Research and Education Foundation.

Rose, A. A., Arambula, E., Howell, T., and Glover, C. J. (2014). An x-ray CT validated laboratory measurement method for air voids distribution over depth in asphalt pavement: a step toward simplified oxidation modeling. *Petroleum Science and Technology* 32:3020–3028.

Rose, A. A., Arambula, E., Liu, G., and Glover, C. J. (2015). Use of a total air void diffusion depth to improve pavement oxidation modeling with field validation. *Petroleum Science and Technology* 33:1198-1207.

Rowe, G. M. (2011). Prepared discussion following the Anderson paper cited above. *Journal of the Association of Asphalt Paving Technologists* 80:649–662.

Rowe, G. M., King, G., and Anderson, M. (2014). The influence of binder rheology on cracking of asphalt mixes in airport and highway projects. *Journal of Testing and Evaluation* 42:1–10.

Ruan, Y., Davison, R. R., and Glover, C. J. (2003). An investigation of asphalt durability: relationships between ductility and rheological properties for unmodified asphalts. *Petroleum Science and Technology* 21:231–254.

Tashman, L., Masad, E., D'Angelo, J., Bukowski, J., Harman, T. (2002). X-ray tomography to characterize air void distribution in superpave gyratory compacted specimens. *International Journal of Pavement Engineering* 3:19–28.

Taylor, J. R. (1982). *An introduction to error analysis*. Mill Valley, California: University Science Books, Oxford University Press.

Vining, G.G. (1998). *Statistical methods for engineers*. Pacific Grove, California: Duxbury Press, Brooks/Cole Publishing Company.

Woo W. J., Ofori-Abebresse E., Chowdhury A., Hilbrich J., Kraus Z., Martin A. E., and Glover C. J. (2007) *Polymer modified asphalt durability in pavements*. Publication FHWA/TX-07/0-4688-1. College Station, Texas: Texas Transportation Institute, Texas A&M University System.

# APPENDIX A

## DATA FOR DETERMINING BSG[+] AND MTSG[±] FOR CHAPTER III CORES

[+] Bulk Specific Gravity
[±] Maximum Theoretical Specific Gravity

SECTION I: DATA FOR VACUUM SEALING METHOD BSG DETERMINATION (ASTM 6752)

**Table A.1: Core 1 (FM 973, HMA, 0 Months Aging, TxDOT 6613 ID: 1-16)**

| | Whole Core | | | Slice 1 | | | Slice 2 | | | Slice 3 | | |
|---|---|---|---|---|---|---|---|---|---|---|---|---|
| **Measurement** | **Rep. 1** | **Rep. 2** | **Rep. 3** | **Rep. 1** | **Rep. 2** | **Rep. 3** | **Rep. 1** | **Rep. 2** | **Rep. 3** | **Rep. 1** | **Rep. 2** | **Rep. 3** |
| **Sample in Air [g]** | 1192.1 | 1192.9 | 1194.2 | 644.6 | 645.3 | 645.3 | 394.2 | 395.0 | 395.3 | -- | -- | -- |
| **Bag in Air [g]** | 27.0 | 26.7 | 26.9 | 25.5 | 25.7 | 26.7 | 25.7 | 27.5 | 26.6 | -- | -- | -- |
| **Sealed Sample in Air [g]** | 1219.0 | 1219.5 | 1221.2 | 670.1 | 670.8 | 672 | 419.7 | 422.2 | 422.0 | -- | -- | -- |
| **Sealed Sample under Water [g]** | 621.0 | 623.1 | 625.6 | 335.1 | 336.7 | 336.1 | 204.7 | 206.0 | 205.5 | -- | -- | -- |
| **BSG** | 2.096 | 2.102 | 2.108 | 2.0971 | 2.107 | 2.102 | 2.106 | 2.119 | 2.106 | -- | -- | -- |

**Table A.2: Core 2 (FM 973, Foamed, 0 Months Aging, TxDOT 6613 ID: 1-17)**

| | Whole Core | | | Slice 1 | | | Slice 2 | | | Slice 3 | | |
|---|---|---|---|---|---|---|---|---|---|---|---|---|
| **Measurement** | **Rep. 1** | **Rep. 2** | **Rep. 3** | **Rep. 1** | **Rep. 2** | **Rep. 3** | **Rep. 1** | **Rep. 2** | **Rep. 3** | **Rep. 1** | **Rep. 2** | **Rep. 3** |
| **Sample in Air [g]** | 1747.9 | 1751.4 | 1751.7 | 549.9 | 550.5 | 550.1 | 333.2 | 333.5 | 334.3 | 529.8 | 531.8 | 531.1 |
| **Bag in Air [g]** | 26.7 | 27.3 | 26.7 | 25.7 | 27.2 | 26.7 | 26.0 | 27.0 | 26.8 | 25.8 | 27.5 | 26.7 |
| **Sealed Sample in Air [g]** | 1774.6 | 1778.7 | 1778.3 | 575.5 | 577.4 | 577 | 358.9 | 360.3 | 361 | 555.7 | 559 | 557.9 |
| **Sealed Sample under Water [g]** | 961.0 | 964.5 | 966.8 | 300.8 | 301.0 | 300.8 | 182.4 | 182.7 | 183.5 | 285.2 | 287.1 | 285.4 |
| **BSG** | 2.228 | 2.232 | 2.238 | 2.228 | 2.229 | 2.225 | 2.246 | 2.248 | 2.252 | 2.184 | 2.197 | 2.180 |

**Table A.3: Core 3 (FM 973, HMA, 14 Months Aging, TxDOT 6613 ID: 1-3-12)**

| | Whole Core | | | Slice 1 | | | Slice 2 | | | Slice 3 | | |
|---|---|---|---|---|---|---|---|---|---|---|---|---|
| **Measurement** | **Rep. 1** | **Rep. 2** | **Rep. 3** | **Rep. 1** | **Rep. 2** | **Rep. 3** | **Rep. 1** | **Rep. 2** | **Rep. 3** | **Rep. 1** | **Rep. 2** | **Rep. 3** |
| **Sample in Air [g]** | 1524.2 | 1526.4 | 1526.1 | 348.9 | 348.7 | 349.1 | 337.6 | 338 | 337.7 | 505.1 | 505.2 | 505.2 |
| **Bag in Air [g]** | 27.1 | 26.1 | 25.5 | 26.6 | 26.8 | 23.1 | 27.1 | 24 | 21.7 | 27.1 | 24.8 | 21.6 |
| **Sealed Sample in Air [g]** | 1550.2 | 1550.9 | 1550.8 | 375.5 | 375.1 | 372.1 | 364.6 | 361.8 | 359.2 | 532.5 | 529.1 | 526.6 |
| **Sealed Sample under Water [g]** | 850.1 | 852 | 851.5 | 192.7 | 192.1 | 192.4 | 186.7 | 185.9 | 187.4 | 279.6 | 278.9 | 280.1 |
| **BSG** | 2.272 | 2.276 | 2.272 | 2.266 | 2.265 | 2.257 | 2.273 | 2.255 | 2.277 | 2.260 | 2.262 | 2.264 |

**Table A.4: Core 4 (FM 973, Foamed, 14 Months Aging, TxDOT 6613 ID: 7-3-13)**

| | Whole Core | | | Slice 1 | | | Slice 2 | | | Slice 3 | | |
|---|---|---|---|---|---|---|---|---|---|---|---|---|
| **Measurement** | **Rep. 1** | **Rep. 2** | **Rep. 3** | **Rep. 1** | **Rep. 2** | **Rep. 3** | **Rep. 1** | **Rep. 2** | **Rep. 3** | **Rep. 1** | **Rep. 2** | **Rep. 3** |
| **Sample in Air [g]** | 1451.8 | 1455.1 | 1454.7 | 415.4 | 416 | 415 | 315.1 | 314.6 | 315.2 | 404.5 | 404.8 | 404.1 |
| **Bag in Air [g]** | 26.2 | 25.7 | 25.7 | 26 | 19.9 | 17.9 | 26.1 | 23.5 | 22 | 25.9 | 23 | 19.5 |
| **Sealed Sample in Air [g]** | 1477 | 1480.4 | 1479.6 | 441.2 | 435.4 | 433 | 341.1 | 338.3 | 335.8 | 430 | 427.3 | 424 |
| **Sealed Sample under Water [g]** | 783.4 | 786.3 | 786.1 | 226.9 | 226.7 | 226.3 | 169.8 | 169.6 | 169.3 | 211.8 | 210.7 | 211.1 |
| **BSG** | 2.182 | 2.184 | 2.185 | 2.232 | 2.223 | 2.216 | 2.203 | 2.196 | 2.209 | 2.127 | 2.112 | 2.107 |

**Table A.5: Core 5 (FM 973, Evotherm, 14 Months Aging, TxDOT 6613 ID: 8-3-5)**

| | Whole Core | | | Slice 1 | | | Slice 2 | | | Slice 3 | | |
|---|---|---|---|---|---|---|---|---|---|---|---|---|
| **Measurement** | **Rep. 1** | **Rep. 2** | **Rep. 3** | **Rep. 1** | **Rep. 2** | **Rep. 3** | **Rep. 1** | **Rep. 2** | **Rep. 3** | **Rep. 1** | **Rep. 2** | **Rep. 3** |
| **Sample in Air [g]** | 1480.1 | 1483.2 | 1484.5 | 437.2 | 437 | 437.4 | 285.6 | 285.7 | 285.7 | 432.4 | 431.8 | 432.4 |
| **Bag in Air [g]** | 26.5 | 26 | 25.9 | 25.6 | 24 | 20.9 | 26.5 | 24.6 | 27.2 | 27.2 | 25.5 | 26.5 |
| **Sealed Sample in Air [g]** | 1506.3 | 1508.1 | 1509.8 | 463 | 461.4 | 458.4 | 311.4 | 310.2 | 312 | 459.1 | 457.6 | 458.6 |
| **Sealed Sample under Water [g]** | 810.5 | 811.8 | 812.7 | 240.7 | 241 | 240.4 | 153.6 | 152.2 | 154.2 | 230.1 | 230.4 | 229.5 |
| **BSG** | 2.219 | 2.220 | 2.219 | 2.247 | 2.248 | 2.239 | 2.212 | 2.175 | 2.226 | 2.167 | 2.163 | 2.158 |

**Table A.6, Part I: Whole Core and Slices 1–3: Core 6 (YNP, HMA, 4 Years Aging)**

| **Measurement** | **Whole Core** | | | **Slice 1** | | | **Slice 2** | | | **Slice 3** | | |
|---|---|---|---|---|---|---|---|---|---|---|---|---|
| | **Rep. 1** | **Rep. 2** | **Rep. 3** | **Rep. 1** | **Rep. 2** | **Rep. 3** | **Rep. 1** | **Rep. 2** | **Rep. 3** | **Rep. 1** | **Rep. 2** | **Rep. 3** |
| **Sample in Air [g]** | 4055.5 | 4067.4 | 4068 | 421.8 | 422 | 421.9 | 258.4 | 258.1 | 258.4 | 302.9 | 302.6 | 302.8 |
| **Bag in Air [g]** | 25.9 | 53.9 | 59.1 | 31.7 | 30.7 | 33.6 | 26.8 | 27 | 26.7 | 27.3 | 27.3 | 27.35 |
| **Sealed Sample in Air [g]** | 4080.3 | 4115 | 4124.6 | 453.5 | 452.6 | 455.7 | 285.2 | 285.4 | 285 | 330 | 329.9 | 329.5 |
| **Sealed Sample under Water [g]** | 2281.9 | 2286.2 | 2284.8 | 228.8 | 229.1 | 228.6 | 143.1 | 143.4 | 143.1 | 167 | 168.2 | 165 |
| **BSG** | 2.291 | 2.297 | 2.291 | 2.216 | 2.218 | 2.212 | 2.285 | 2.289 | 2.287 | 2.270 | 2.290 | 2.245 |

**Table A.6, Part II: slices 4–7**

| | Slice 4 | | | Slice 5 | | | Slice 6 | | | Slice 7 | | |
|---|---|---|---|---|---|---|---|---|---|---|---|---|
| **Measurement** | **Rep. 1** | **Rep. 2** | **Rep. 3** | **Rep. 1** | **Rep. 2** | **Rep. 3** | **Rep. 1** | **Rep. 2** | **Rep. 3** | **Rep. 1** | **Rep. 2** | **Rep. 3** |
| **Sample in Air [g]** | 375.9 | 375.6 | 375.7 | 288.7 | 289.1 | 288.6 | 388.7 | 388.9 | 388.6 | 293.1 | 293.1 | 292.6 |
| **Bag in Air [g]** | 26.5 | 26.9 | 26.8 | 26.5 | 26.2 | 26.7 | 26.6 | 26.1 | 27.25 | 27 | 26.8 | 26.5 |
| **Sealed Sample in Air [g]** | 402.4 | 402.6 | 402.4 | 315.4 | 315.5 | 315 | 415.3 | 416 | 415.5 | 320.1 | 319.1 | 319.4 |
| **Sealed Sample under Water [g]** | 203.6 | 205.2 | 202.7 | 161.4 | 161 | 158.4 | 216.8 | 215.8 | 215.3 | 163.3 | 163.3 | 163.3 |
| **BSG** | 2.210 | 2.232 | 2.201 | 2.304 | 2.292 | 2.260 | 2.291 | 2.262 | 2.277 | 2.298 | 2.312 | 2.297 |

**Table A.6 Part III: slice 8**

| **Measurement** | **Slice 8** | | | -- | | | -- | | | -- | | |
|---|---|---|---|---|---|---|---|---|---|---|---|---|
| | **Rep. 1** | **Rep. 2** | **Rep. 3** | **Rep. 1** | **Rep. 2** | **Rep. 3** | **Rep. 1** | **Rep. 2** | **Rep. 3** | **Rep. 1** | **Rep. 2** | **Rep. 3** |
| **Sample in Air [g]** | 577.1 | 578.4 | 578.7 | -- | -- | -- | -- | -- | -- | -- | -- | -- |
| **Bag in Air [g]** | 31.1 | 30.5 | 31.3 | -- | -- | -- | -- | -- | -- | -- | -- | -- |
| **Sealed Sample in Air [g]** | 608.4 | 609 | 609.9 | -- | -- | -- | -- | -- | -- | -- | -- | -- |
| **Sealed Sample under Water [g]** | 313.1 | 314.5 | 314 | -- | -- | -- | -- | -- | -- | -- | -- | -- |
| **BSG** | 2.206 | 2.212 | 2.209 | | | | | | | | | |

**Notes**

1. For additional discussion regarding the ASTM method see Woo W. J., Ofori-Abebresse E., Chowdhury A., Hilbrich J., Kraus Z., Martin A. E., and Glover C. J. (2007) *Polymer modified asphalt durability in pavements*, Chapter 5. Publication FHWA/TX-07/0-4688-1. College Station, Texas: Texas Transportation Institute, Texas A&M University System.

2. BSG Formula:

$$\text{BSG} = \frac{\text{Sample}}{\text{Sealed Sample} - \text{Sealed Sample Submerged} - \frac{\text{Bag}}{\text{Bag Specific Gravity}}}$$

3. Specific gravity of bag material (Provided by Instrotek Inc.): 0.923.

SECTION II: DATA FOR VACUUM SEALING AND RICE MTSG DETERMINATIONS (ASTM 6857 AND ASTM 2041)

**Table A.7: Core 1 (FM 973, HMA, 0 Months Aging, TxDOT 6613 ID: 1-16)**

| | Slice 1 | | | Slice 2 | | | Slice 3 | | |
|---|---|---|---|---|---|---|---|---|---|
| **Measurement** | **Rep. 1** | **Rep. 2** | **Rep. 3** | **Rep. 1** | **Rep. 2** | **Rep. 3** | **Rep. 1** | **Rep. 2** | **Rep. 3** |
| **Sample in Air [g]** | 641.5 | 638.0 | 634.6 | 386.6 | 388.9 | 387.1 | -- | -- | -- |
| **Bags in Air [g]** | 69.5 | 75.4 | 75.8 | 75.2 | 74.8 | 75.3 | -- | -- | -- |
| **Sample and Bags in Air [g]** | 710.3 | 712.7 | 709.8 | 461.9 | 463.8 | 462.3 | -- | -- | -- |
| **Sample and Bags (opened) under Water [g]** | 371.9 | 372.5 | 369.5 | 228.7 | 225.3 | 225.0 | -- | -- | -- |
| **Bowl Under Water [g]** | 1371.5 | 1572.7 | 212.0 | 1371.5 | 1572.7 | 1371.5 | -- | -- | -- |
| **Sample and Bowl Under Water [g]** | 1749.7 | 1949.2 | 587.0 | 1601.9 | 1805.4 | 1602.3 | -- | -- | -- |
| **MTSG Vacuum Sealing** | 2.438 | 2.468 | 2.458 | 2.548 | 2.470 | 2.486 | -- | -- | -- |
| **MTSG Rice** | 2.436 | 2.440 | 2.445 | 2.475 | 2.490 | 2.477 | -- | -- | -- |

**Table A.8: Core 2 (FM 973, Foamed, 0 Months Aging, TxDOT 6613 ID: 1-17)**

| | Slice 1 | | | Slice 2 | | | Slice 3 | | |
|---|---|---|---|---|---|---|---|---|---|
| **Measurement** | **Rep. 1** | **Rep. 2** | **Rep. 3** | **Rep. 1** | **Rep. 2** | **Rep. 3** | **Rep. 1** | **Rep. 2** | **Rep. 3** |
| **Sample in Air [g]** | 547.3 | 543.9 | 541.5 | 332.2 | 329.5 | 328.1 | 525.6 | 521.6 | 520.2 |
| **Bags in Air [g]** | 68.6 | 68.7 | 75.7 | 68.0 | 67.9 | 74.6 | 69.5 | 76.1 | 74.8 |
| **Sample and Bags in Air [g]** | 616.0 | 612.3 | 615.5 | 400.5 | 397.4 | 402.8 | 595.5 | 597.6 | 595.1 |
| **Sample and Bags (opened) under Water [g]** | 310.0 | 300.7 | 312.3 | 189.6 | 189.4 | 188 | 297.8 | 302.8 | 302.9 |
| **Bowl Under Water [g]** | 1572.7 | 1572.7 | 213.0 | 1371.5 | 1371.5 | 1371.5 | 1572.7 | 1371.5 | 1572.7 |
| **Sample and Bowl Under Water [g]** | 1895.9 | 1894 | 532.4 | 1568.3 | 1567.4 | 1566.4 | 1883.5 | 1681.6 | 1882 |
| **MTSG Vacuum Sealing** | 2.362 | 2.293 | 2.448 | 2.421 | 2.451 | 2.449 | 2.363 | 2.456 | 2.464 |
| **MTSG Rice** | 2.442 | 2.443 | 2.438 | 2.453 | 2.466 | 2.463 | 2.447 | 2.466 | 2.467 |

**Table A.9: Core 3 (FM 973, HMA, 14 Months Aging, TxDOT 6613 ID: 1-3-12)**

| | Slice 1 | | | Slice 2 | | | Slice 3 | | |
|---|---|---|---|---|---|---|---|---|---|
| **Measurement** | **Rep. 1** | **Rep. 2** | **Rep. 3** | **Rep. 1** | **Rep. 2** | **Rep. 3** | **Rep. 1** | **Rep. 2** | **Rep. 3** |
| **Sample in Air [g]** | 334.3 | 332.2 | 332.2 | 326.5 | 324.1 | 323.6 | 479.2 | 477.5 | 476.2 |
| **Bags in Air [g]** | 27.2 | 27.5 | 27.2 | 27.2 | 27.9 | 27.6 | 27.3 | 27.0 | 26.5 |
| **Sample and Bags in Air [g]** | 361.2 | 360.5 | 359.3 | 353.6 | 352.1 | 350.2 | 506.3 | 504.7 | 503.0 |
| **Sample and Bags (opened) under Water [g]** | 193.2 | 192.6 | 192.8 | 190.5 | 188.2 | 187.5 | 281.7 | 279.0 | 269.3 |
| **Bowl Under Water [g]** | 1372.4 | 1574.0 | 1574.0 | 1574.0 | 1372.4 | 1574.0 | 1574.0 | 1574.0 | 1372.4 |
| **Sample and Bowl Under Water [g]** | 1570.4 | 1771.4 | 1771.7 | 1766.7 | 1565.0 | 1766.0 | 1859.5 | 1858.4 | 1651.0 |
| **MTSG Vacuum Sealing** | 2.413 | 2.405 | 2.424 | 2.443 | 2.425 | 2.437 | 2.457 | 2.4314 | 2.323 |
| **MTSG Rice** | 2.453 | 2.464 | 2.470 | 2.440 | 2.465 | 2.459 | 2.474 | 2.473 | 2.410 |

**Table A.10: Core 4 (FM 973, Foamed, 14 Months Aging, TxDOT 6613 ID: 7-3-13)**

| | Slice 1 | | | Slice 2 | | | Slice 3 | | |
|---|---|---|---|---|---|---|---|---|---|
| **Measurement** | **Rep. 1** | **Rep. 2** | **Rep. 3** | **Rep. 1** | **Rep. 2** | **Rep. 3** | **Rep. 1** | **Rep. 2** | **Rep. 3** |
| **Sample in Air [g]** | 374.9 | 373 | 371.5 | 276.1 | 274.5 | 274.4 | 379.3 | 377.6 | 377.3 |
| **Bags in Air [g]** | 38.5 | 27.3 | 27.3 | 27.0 | 18.3 | 27.0 | 26.9 | 27.4 | 26.6 |
| **Sample and Bags in Air [g]** | 413.4 | 400.3 | 398.9 | 302.9 | 292.7 | 301.2 | 406.4 | 405.1 | 404.6 |
| **Sample and Bags (opened) under Water [g]** | 219.3 | 219.3 | 218.3 | 161.0 | 162.2 | 159.9 | 220.3 | 220.4 | 220.1 |
| **Bowl Under Water [g]** | 1574 | 1574.0 | 1574.0 | 1372.4 | 1574.0 | 1372.4 | 1372.4 | 1574.0 | 1574.0 |
| **Sample and Bowl Under Water [g]** | 1798.6 | 1797.5 | 1797.0 | 1537.8 | 1738.3 | 1536.3 | 1596.7 | 1798.5 | 1798.7 |
| **MTSG Vacuum Sealing** | 2.460 | 2.463 | 2.460 | 2.451 | 2.480 | 2.449 | 2.417 | 2.436 | 2.423 |
| **MTSG Rice** | 2.494 | 2.495 | 2.502 | 2.494 | 2.491 | 2.483 | 2.447 | 2.466 | 2.472 |

**Table A.11: Core 5 (FM 973, Evotherm, 14 Months Aging, TxDOT 6613 ID: 8-3-5)**

| | Slice 1 | | | Slice 2 | | | Slice 3 | | |
|---|---|---|---|---|---|---|---|---|---|
| **Measurement** | **Rep. 1** | **Rep. 2** | **Rep. 3** | **Rep. 1** | **Rep. 2** | **Rep. 3** | **Rep. 1** | **Rep. 2** | **Rep. 3** |
| **Sample in Air [g]** | 411.2 | 409.5 | 407.3 | 269.0 | 267.0 | 266.8 | 406.9 | 404.9 | 404.7 |
| **Bags in Air [g]** | 27.2 | 27.5 | 27.1 | 27.4 | 27.5 | 26.6 | 27.4 | 27.1 | 26.6 |
| **Sample and Bags in Air [g]** | 438.5 | 436.3 | 434.4 | 296.2 | 294.7 | 293.6 | 434.1 | 431.6 | 431.1 |
| **Sample and Bags (opened) under Water [g]** | 242.3 | 241.9 | 240.3 | 156.4 | 157.1 | 155.6 | 240.1 | 238.1 | 238.4 |
| **Bowl Under Water [g]** | 1372.4 | 1372.4 | 1372.4 | 1574.0 | 1372.4 | 1372.4 | 1372.4 | 1372.4 | 1372.4 |
| **Sample and Bowl Under Water [g]** | 1617.8 | 1616.7 | 1616.4 | 1734.5 | 1531.5 | 1532.4 | 1616.3 | 1615.1 | 1615.5 |
| **MTSG Vacuum Sealing** | 2.466 | 2.488 | 2.472 | 2.443 | 2.477 | 2.443 | 2.476 | 2.467 | 2.469 |
| **MTSG Rice** | 2.480 | 2.479 | 2.494 | 2.479 | 2.475 | 2.498 | 2.496 | 2.496 | 2.504 |

**Table A.12 (part I: slices 1–4): Core 6 (YNP, HMA, 4 Years Aging)**

| | Slice 1 | | | Slice 2 | | | Slice 3 | | | Slice 4 | | |
|---|---|---|---|---|---|---|---|---|---|---|---|---|
| **Measurement** | **Rep. 1** | **Rep. 2** | **Rep. 3** | **Rep. 1** | **Rep. 2** | **Rep. 3** | **Rep. 1** | **Rep. 2** | **Rep. 3** | **Rep. 1** | **Rep. 2** | **Rep. 3** |
| **Sample in Air [g]** | 419.7 | 415.3 | 414.2 | 257.8 | 255.1 | 253.7 | 301.7 | 298.9 | 298.7 | 374.0 | 371.3 | 370.2 |
| **Bags in Air [g]** | 64.3 | 67.6 | 74.8 | 64.4 | 67.6 | 75.0 | 63.7 | 67.5 | 75.3 | 64.9 | 67.9 | 76.0 |
| **Sample and Bags in Air [g]** | 483.7 | 482.4 | 489.8 | 322.3 | 322.5 | 329.8 | 365.2 | 366.3 | 374.0 | 438.8 | 438.5 | 445.7 |
| **Sample and Bags (opened) under Water [g]** | 243.0 | 240.3 | 239.5 | 147.5 | 145.5 | 143.5 | 172.3 | 173.2 | 170.7 | 216.0 | 214.0 | 212.4 |
| **Bowl Under Water [g]** | 1572.7 | 1572.7 | 1572.7 | 1371.5 | 1572.7 | 1371.5 | 1572.7 | 1572.7 | 1572.7 | 1371.5 | 1572.7 | 1371.5 |
| **Sample and Bowl Under Water [g]** | 1820.6 | 1818.6 | 1818.0 | 1524.6 | 1723.7 | 1522.2 | 1751.7 | 1750.0 | 1750.0 | 1593.5 | 1792.3 | 1590.3 |
| **MTSG Vacuum Sealing** | 2.454 | 2.459 | 2.447 | 2.455 | 2.456 | 2.415 | 2.435 | 2.491 | 2.454 | 2.453 | 2.460 | 2.452 |
| **MTSG Rice** | 2.443 | 2.452 | 2.452 | 2.462 | 2.451 | 2.463 | 2.459 | 2.458 | 2.460 | 2.461 | 2.448 | 2.445 |

**Table A.12 (part II: slices 5–8)**

| Measurement | Slice 5 | | | Slice 6 | | | Slice 7 | | | Slice 8 | | |
|---|---|---|---|---|---|---|---|---|---|---|---|---|
| | Rep. 1 | Rep. 2 | Rep. 3 | Rep. 1 | Rep. 2 | Rep. 3 | Rep. 1 | Rep. 2 | Rep. 3 | Rep. 1 | Rep. 2 | Rep. 3 |
| **Sample in Air [g]** | 287.8 | 285.0 | 284.7 | 387.3 | 384.2 | 383.6 | 292.1 | 289.9 | 288.9 | 575.0 | 568.4 | 566.8 |
| **Bags in Air [g]** | 64.1 | 67.7 | 75.8 | 63.1 | 67.8 | 73.8 | 70.9 | 67.4 | 74.9 | 65.0 | 67.7 | 75.0 |
| **Sample and Bags in Air [g]** | 352.0 | 352.9 | 360.3 | 450.2 | 451.2 | 458.1 | 362.0 | 357.5 | 363.8 | 639.0 | 636.1 | 641.3 |
| **Sample and Bags (opened) under Water [g]** | 165.5 | 160.8 | 161.7 | 222.9 | 220.0 | 219.6 | 165.4 | 163.5 | 163.2 | 330.4 | 318.5 | 325.9 |
| **Bowl Under Water [g]** | 1572.7 | 1572.7 | 1572.7 | 1371.5 | 1572.7 | 1371.5 | 1572.7 | 1572.7 | 1371.5 | 1371.5 | 1371.5 | 1572.7 |
| **Sample and Bowl Under Water [g]** | 1743.4 | 1741.4 | 1741.2 | 1599.6 | 1799.0 | 1597.2 | 1744.8 | 1743.6 | 1541.6 | 1707.8 | 1705.0 | 1905.0 |
| **MTSG Vacuum Sealing** | 2.459 | 2.400 | 2.444 | 2.437 | 2.436 | 2.420 | 2.439 | 2.396 | 2.419 | 2.414 | 2.327 | 2.421 |
| **MTSG Rice** | 2.458 | 2.451 | 2.450 | 2.438 | 2.433 | 2.429 | 2.434 | 2.436 | 2.432 | 2.409 | 2.420 | 2.417 |

**Notes**

1. For additional discussion on ASTM methods see Woo W. J., Ofori-Abebresse E., Chowdhury A., Hilbrich J., Kraus Z., Martin A. E., and Glover C. J. (2007) *Polymer modified asphalt durability in pavements*, Chapter 5. Publication FHWA/TX-07/0-4688-1. College Station, Texas: Texas Transportation Institute, Texas A&M University System.

2. Vacuum Sealing MTSG Formula:

$$MTSG = \frac{\text{Sample}}{(\text{Sample \& Bags}) - (\text{Open Sample \& Bags Submerged}) - \frac{\text{Bags}}{\text{Bag Specific Gravity}}}$$

3. Rice MTSG Formula:

$$MTSG = \frac{\text{Sample}}{\text{Sample} - (\text{Sample \& Bowl Submerged} - \text{Bowl Submerged})}$$

4. Specific gravity of bag material (Provided by Instrotek Inc.): 0.923.

5. Construction loose mix MTSG (cores 1–5): 2.420, 2.400, 2.420, 2.400, 2.408.

6. Mix design MTSG (core 6): 2.424.

# APPENDIX B

# CARBONYL AREA, LSV[+], AND DSR FUNCTION[±] DATA FOR FM 973 FIELD CORES

[+] Low sheer rate limiting complex dynamic viscosity measured at 60 °C and 0.01 rad/s.
[±] Defined as $G'/(\eta'/G')$ referenced to 15 °C and 0.005 rad/s. See discussion in Chapter I.

**Table B.1: Carbonyl Area [arb. u.]: Primary Cores[a] and Original Binder**

| Field Aging [Months] | Slice | Warm Mix Technology | | |
|---|---|---|---|---|
| | | None (HMA) | Foamed | Evotherm |
| Original Binder | N/A | 0.56 | 0.57 | 0.58 |
| 0/1 | 1 | 0.75 | 0.68 | -- |
| | 2 | 0.77 | 0.67 | -- |
| | 3 | -- | 0.75 | -- |
| 8 | 1 | -- | -- | -- |
| | 2 | -- | -- | -- |
| | 3 | -- | -- | -- |
| 14 | 1 | 0.95 | 0.89 | 0.86 |
| | 2 | 0.88 | 0.82 | 0.79 |
| | 3 | 0.87 | 0.95 | 0.83 |

**Table B.2: Carbonyl Area [arb. u.]: Replicate Cores[b]**

| Field Aging [Months] | Slice | Warm Mix Technology | | |
|---|---|---|---|---|
| | | None (HMA) | Foamed | Evotherm |
| 0/1 | 1 | 0.77 | 0.78 | 0.79 |
| | 2 | 0.72 | 0.70 | 0.68 |
| | 3 | -- | 0.67 | 0.76 |
| 8 | 1 | 0.90 | 0.94 | 0.91 |
| | 2 | 0.86 | 0.80 | 0.79 |
| | 3 | 0.86 | 0.84 | 0.80 |
| 14 | 1 | 1.00 | 1.06 | 0.96 |
| | 2 | 0.87 | 0.86 | 0.81 |
| | 3 | 0.98 | 0.90 | 0.77 |

**Table B.3: LSV [Poise] (60 °C and 0.01 rad/s): Primary Cores[a] and Original Binder**

| Field Aging [Months] | Slice | Warm Mix Technology | | |
|---|---|---|---|---|
| | | None (HMA) | Foamed | Evotherm |
| Original Binder | N/A | 12000[c] | 18000 | 10000[c] |
| 0/1 | 1 | -- | -- | -- |
| | 2 | -- | -- | -- |
| | 3 | -- | -- | -- |
| 8 | 1 | -- | -- | -- |
| | 2 | -- | -- | -- |
| | 3 | -- | -- | -- |
| 14 | 1 | 63000 | 56000 | 57000 |
| | 2 | 55000 | 65000 | 56000 |
| | 3 | 58000 | 80000 | 57000 |

**Table B.4: LSV [Poise] (60 °C and 0.01 rad/s): Replicate Cores[b]**

| Field Aging [Months] | Slice | Warm Mix Technology | | |
|---|---|---|---|---|
| | | None (HMA) | Foamed | Evotherm |
| 0/1 | 1 | -- | 50000 | 47000 |
| | 2 | -- | 37000 | 25000 |
| | 3 | -- | 31000 | 41000 |
| 8 | 1 | 110000 | 69000 | 92000 |
| | 2 | 69000 | 81000 | 46000 |
| | 3 | 61000 | 102000 | 55000 |
| 14 | 1 | -- | -- | -- |
| | 2 | -- | -- | -- |
| | 3 | -- | -- | -- |

**Table B.5: DSR Function[d] [MPa/s]: Primary Cores[a] and Original Binder**

| Field Aging [Months] | Slice | Warm Mix Technology | | |
|---|---|---|---|---|
| | | None (HMA) | Foamed | Evotherm |
| Original Binder | N/A | 0.000021[c] | 0.000037 | 0.000020[c] |
| 0/1 | 1 | -- | -- | -- |
| | 2 | -- | -- | -- |
| | 3 | -- | -- | -- |
| 8 | 1 | -- | -- | -- |
| | 2 | -- | -- | -- |
| | 3 | -- | -- | -- |
| 14 | 1 | 0.000201 | 0.000181 | 0.000189 |
| | 2 | 0.000172 | 0.000224 | 0.000191 |
| | 3 | 0.000202 | 0.000297 | 0.000189 |

**Table B.6: DSR Function[d] [MPa/s]: Replicate Cores[b]**

| Field Aging [Months] | Slice | Warm Mix Technology | | |
|---|---|---|---|---|
| | | None (HMA) | Foamed | Evotherm |
| 0/1 | 1 | -- | 0.000149 | 0.000132 |
| | 2 | -- | 0.000103 | 0.000057 |
| | 3 | -- | 0.000080 | 0.000111 |
| 8 | 1 | 0.000362 | 0.000221 | 0.000321 |
| | 2 | 0.000220 | 0.000271 | 0.000133 |
| | 3 | 0.000203 | 0.000400 | 0.000184 |
| 14 | 1 | -- | -- | -- |
| | 2 | -- | -- | -- |
| | 3 | -- | -- | -- |

**Notes**

[a]The primary cores correspond to cores 1–5 in Chapter III, and the 14 month primary cores correspond to cores 7–9 in Chapter IV. Primary cores were received as whole cores and x-ray CT scans are available.

[b]The replicate cores were used as the control cores in Chapter III (see Figure 16) and whole-core average CA values from the 0/1 month replicate cores were used for the construction core CA values in Chapter IV. Cut-off core portions were received and x-ray CT scans are not available.

[c]Data collected by Guanlan Liu.

[d]Defined as $G'/(\eta'/G')$ referenced to 15 °C and 0.005 rad/s. See Chapter I for discussion.

# APPENDIX C

# FOAMED VALERO 70-22[+] POV[±] AGING EXPERIMENT DATA

[+] Binder used in FM 973 foaming test section. See Glover, C. J., Liu, G., Rose, A. A., Tong, Y., Gu, F., Ling, M., Arambula, E., Estakhri, C., Lytton, R. (2014b). *Evaluate Binder and Mixture Aging for Warm Mix Asphalt: Technical Report*. Publication FHWA/TX-13/0-6613. College Station, Texas: Texas Transportation Institute, Texas A&M University System.

[±] Pressure Oxidation Vessel. See Chapter I for a brief discussion and references.

## Table C.1: CA[a], LSV[b], and DSR Function[c] Results

| Aging Time [Days] | Temperature | | | | | | | | | | | |
|---|---|---|---|---|---|---|---|---|---|---|---|---|
| | 140 °F | | | 163 °F | | | 186 °F | | | 208 °F | | |
| | CA | LSV | DSR Fn | CA | LSV | DSR Fn | CA | LSV | DSR Fn | CA | LSV | DSR Fn |
| **0** | 0.57 | 18000 | 0.000037 | 0.57 | 18000 | 0.000037 | 0.57 | 18000 | 0.000037 | 0.57 | 18000 | 0.000037 |
| **1** | -- | -- | -- | 0.64 | 24000 | 0.000055 | 0.62 | 30000 | 0.000082 | 0.77 | 55000 | 0.000159 |
| **2** | 0.56 | 27000 | 0.000063 | 0.58 | 27000 | 0.000063 | 0.67 | 44000 | 0.000120 | 0.84 | 102000 | 0.000318 |
| **3** | -- | -- | -- | 0.62 | 27000 | 0.000069 | 0.96 | 77000 | 0.000241 | -- | -- | -- |
| **4** | -- | -- | -- | -- | -- | -- | -- | -- | -- | 1.09 | 314000 | 0.001020 |
| **5** | 0.62 | 32000 | 0.000102 | 0.75 | 40000 | 0.000105 | 0.90 | 73000 | 0.000217 | -- | -- | -- |
| **6** | -- | -- | -- | -- | -- | -- | 0.90 | 40000 | 0.000141 | 1.26 | 252000 | 0.001087 |
| **7** | -- | -- | -- | 0.78 | 48000 | 0.000130 | 0.95 | 64000 | 0.000221 | 1.32 | 329000 | 0.001250 |
| **10** | 0.68 | 39000 | 0.000106 | 0.77 | 61000 | 0.000190 | 1.07 | 135000 | 0.000470 | 1.55 | 973000 | 0.003511 |
| **15** | -- | -- | -- | 0.89 | 63000 | 0.000200 | 1.07 | 185000 | 0.000726 | 1.50 | 3981000 | 0.009304 |
| **20** | 0.74 | 53000 | 0.000154 | 0.84 | 68000 | 0.000216 | 1.33 | 321000 | 0.001348 | 2.15 | -- | -- |
| **25** | -- | -- | -- | -- | -- | -- | -- | -- | -- | 1.66 | -- | 0.039281 |
| **30** | 0.85 | 45000 | 0.000148 | 1.04 | 92000 | 0.000364 | 1.39 | 660000 | 0.003304 | 1.55 | -- | 0.030960 |
| **40** | -- | -- | -- | 1.08 | 138000 | 0.000619 | 1.74 | 2394000 | 0.008177 | -- | -- | -- |
| **45** | 0.89 | 157000 | 0.000623 | -- | -- | -- | -- | -- | -- | -- | -- | -- |
| **55** | -- | -- | -- | 1.24 | 166000 | 0.000915 | 1.84 | 2513000 | 0.008165 | -- | -- | -- |
| **62** | 0.94 | 86000 | 0.000372 | -- | -- | -- | -- | -- | -- | -- | -- | -- |
| **91** | 1.06 | 93000 | 0.000487 | -- | -- | -- | -- | -- | -- | -- | -- | -- |

[a]Carbonyl area

[b]Low sheer rate limiting complex dynamic viscosity measured at 60 °C and 0.01 rad/s reported in units of Poise.

[c]Defined as $G'/(\eta'/G')$ referenced to 15 °C and 0.005 rad/s reported in units of MPa/s. See Chapter I discussion.

**Table C.2: Parameters Determined Based On POV Aging Results[a]**

| Reaction Kinetics Parameters[b] | | Viscosity HS[c] Relation[d] | | DSR Function HS[c] Relation[e] | |
|---|---|---|---|---|---|
| $E_{ac}$ [kJ/mol] | 65.8 | Viscosity HS | 3.96 | DSR Fn HS | 4.8 |
| $A_c$ [CA/Day] | $8.22 \times 10^7$ | $m_{LSV}$ | 7.71 | $m_{DSR\ Fn}$ | -12.7 |
| $E_{af}$ [kJ/mol] | 47.1 | | | | |
| $A_f$ [1/Day] | $2.45 \times 10^6$ | | | | |
| M | 0.18 | | | | |

[a]For additional discussion and graphs see Glover, C. J., Liu, G., Rose, A. A., Tong, Y., Gu, F., Ling, M., Arambula, E., Estakhri, C., Lytton, R. (2014b). *Evaluate Binder and Mixture Aging for Warm Mix Asphalt: Technical Report*, Chapter 3 Publication FHWA/TX-13/0-6613. College Station, Texas: Texas

[b]Optimization excluded aging temperature 208 °F data because of excessively scattered CA results.

[c]Hardening Susceptibility

[d]Corresponds to form: Viscosity [poise] = $e^{m_{LSV}} \cdot e^{\text{Viscosity HS}\cdot CA}$.

[e]Corresponds to form: DSR function [MPa/s] = $e^{m_{DSR\ Fn}} \cdot e^{\text{DSR Fn HS}\cdot CA}$.

# APPENDIX D

# INVESTIGATION OF EFFECTS OF RECYCLING AGENTS IN RECYCLED ASPHALT BLENDS: OXIDATION SCREENING AND EXUDATION DROPLET TESTING

SECTION I: OXIDATION SCREENING[+]

## INTRODUCTION

The performance of an asphalt paving mixture containing reclaimed asphalt pavement (RAP) or recycled asphalt shingles (RAS) depends, in part, on the properties of the resulting binder blend. When virgin binders are blended with RAP or RAS the properties of the resulting blend are influenced by the recycled binder. It is often desired to reverse this influence in order to produce a blend with more favorable properties. To achieve this, recycling agent (RA) may be added to the binder blend. The effectiveness of a RA depends on its ability to positively affect both the physical properties of the blend and the chemical properties, which influence how the physical properties will change with the binder's in-pavement life cycle.

Therefore, to determine whether recycling agents can reverse the influence of the recycled materials, evaluation of the blend must include both initial physical blend properties, and how those properties will change with time. Evaluation of initial physical properties can be appropriately limited to physical measurements on the recycled blend (e.g. measurements of the complex dynamic elastic modulus, G*, and the corresponding phase angle, δ). Evaluation of how a blend's physical properties will change with time requires a model that will allow for predictions with time. This is because a direct test of a binder's performance over a pavement's life cycle is, in general, time prohibitive. As a solution, measurements of a binder's reaction kinetics parameters, along with a pavement aging model, can be used predict in-field binder performance over the life of a pavement.

While measurement of a binder's reaction kinetics parameters is feasible, it is relatively time consuming, and is not necessary to answer the simpler question of whether two binders have different reaction kinetics parameters. At present, complete reaction kinetics parameters determination requires several months, and reaction kinetics parameters are asphalt specific. Despite this, when considering the effect of a binder additive (such as a RA), it may be that the RA does not affect the base binder's kinetics parameters. Therefore, rather than determine the kinetics parameters for each blend of interest, it may be possible to screen for additives that influence the reaction kinetics parameters of binder blends.

In theory, if a binder's CA reaction rate at a given temperature and pressure (other than an isokinetic temperature-pressure combination) matches the reaction rate of

[+] This work was performed as part of Phase I and Phase II of project NCHRP 9-58, *The Effects of Recycling Agents on Asphalt Mixtures with High RAS and RAP Binder Ratios*.

another binder, then the two binders will have equal reaction kinetics parameters. Therefore, for screening purposes, it should be possible to age a binder at a single temperature and pressure and compare the CA reaction rate to that of the alternative binder.

In practice, measurement of a binder's CA reaction rate at a single temperature-pressure combination for comparison with the reaction rate of another binder is complicated because rates must be fast enough, or times must be long enough, to produce measureable differences. Elevated pressure, such as the pressure typically used for PAV aging (20.7 atm. gauge), increases CA reaction rate. Importantly, binders having higher CA reaction rates at PAV pressure are also expected to have higher reaction rates at atmospheric pressure (Cui et al, 2014). A further complication is that typically PAVs are operated somewhat near to the isokinetic temperature (for PAV pressure ~100 °C). To measure differences in asphalt reaction rates it is preferred or even necessary, to operate further from the isokinetic temperature. In addition, it is preferred to test at temperatures lower than 100 °C for two reasons. First, relative reaction rates will reverse above the isokinetic temperature, and second it is suspected that at higher temperatures asphalt oxidation reactions may differ significantly from those at atmospheric conditions.

In this work, PAV screening tests at 60 °C were used to determine if specific RAs affect binder CA reaction rates, and hence reaction kinetics parameters.

## MATERIALS AND METHODS

### Materials

#### *Part I: Virgin Binder plus RA PAV Screening*

Screening tests were performed using 64-22 virgin binder from the Texas project, and the same binder mixed with RA to create 10% (wt. RA/wt. total blend) blends. Specifically, the following screening tests were performed.

- 64-22 (virgin binder from the Texas project)
- R (Safety Kleen REO)
- A1 (Hydrolene H90T)
- P (Hydrolene SP125)
- T1 (Hydrogreen)

The total mass of asphalt blend prepared per screening was 80 grams, which consisted of 72 grams virgin binder and 8 grams of RA.

#### *Part II: Control Blend Plus RA PAV Screening*

Screening tests were performed using a control blend, and the control blend mixed with RA to create 10% (wt. RA/wt. total blend) blends. The addition of the RA to achieve

10% was by replacement of the virgin binder in the control blend. The control blend contained a RBR of 30% (the control blend contained 10% RAP (wt. RAP binder/wt. total blend) and 20% RAS (wt. RAS binder/wt. total blend)). Specifically, the following screening tests will be performed.

- Control (virgin binder from the Texas project with 30% recycled binder)
- R (Safety Kleen REO)
- A1 (Hydrolene H90T)
- P (Hydrolene SP125)
- T1 (Hydrogreen)

**Methods**

PAV screening is performed to determine if RA addition affects CA reaction rates. PAV aging is conducted at 60 °C, which is the lowest operating temperature for the PAVs available. This temperature was selected because it is relatively far from the isokinetic temperature (~100 °C). As discussed above, the further away the aging temperature is from the isokinetic temperature the larger the differences in the asphalt reaction rates are expected to be.

Aging times are 0, 24, 48, 72, 96, and 120 hours. Figure D.1 provides a detailed comparison of expected CA increase at 60 °C with the expected increase at the standard temperatures (i.e. 90 °C and 100 °C). The expected CA increase at atmospheric pressure and 85 °C (5 day limit) is also shown for reference (this estimation assumes no oxygen diffusion resistance in the binder). All estimates are based on reported kinetics parameters for a binder produced by the same manufacturer that also had the same PG grade (Cui et al, 2014) (details provided in Table D.1). Figure D.1 also shows the number of replicates for each aging time. Aged binders are tested for carbonyl area using FTIR and aging rates are determined.

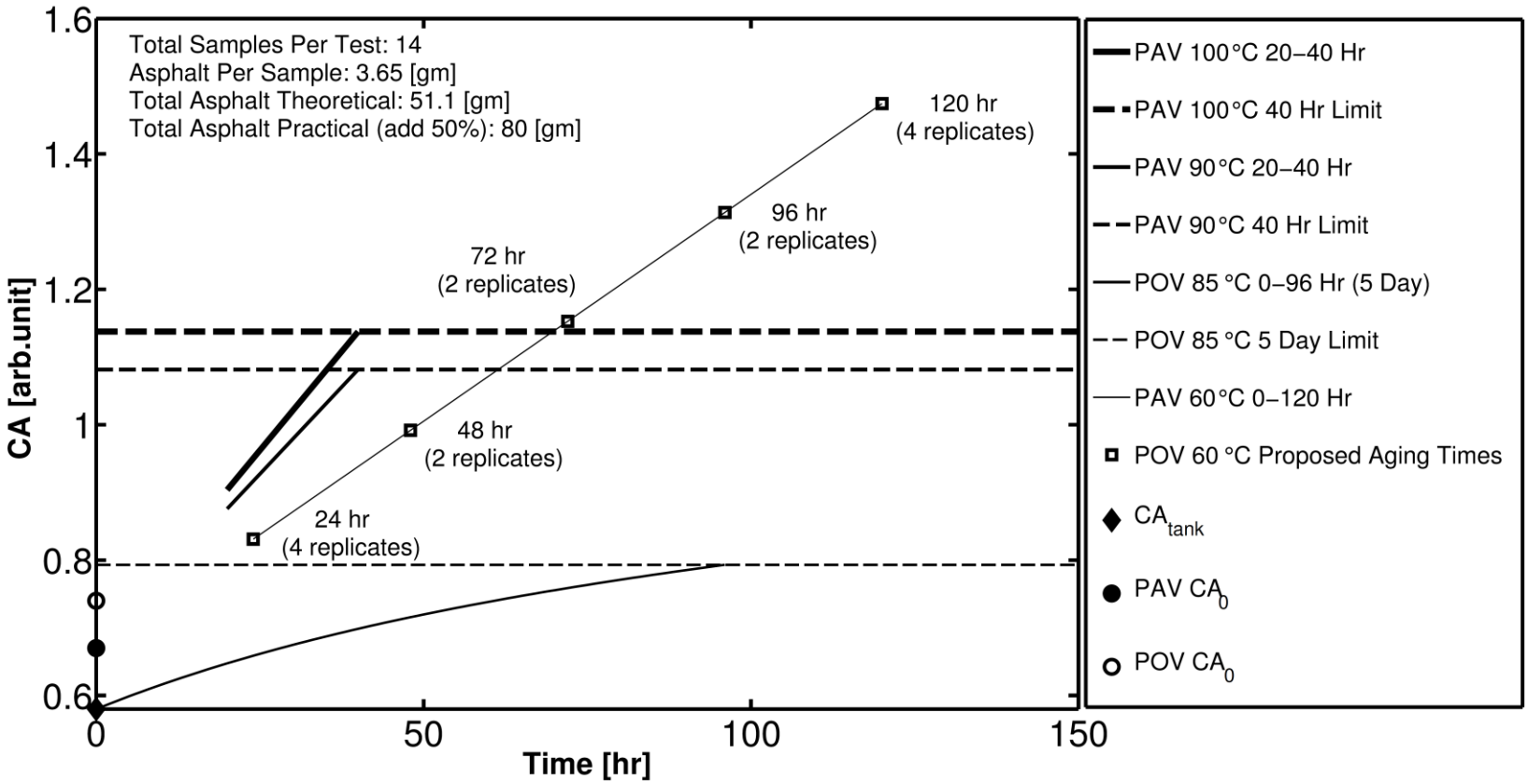


**Figure D.1. Proposed 60 °C PAV Screening Aging Times (rough comparison with expected PAV growth at 90–100 °C for 40 hr.). Estimates based on kinetics data from Cui et al., 2014, and supplemental data from research files, for Lion 64-22 binder (from TxDOT project 6009).**

**Table D.1. Kinetics Parameters, etc. for Figure 1 Preparation.**

| | PAV | POV |
|---|---|---|
| **Pressure** | 20.7 [atm. gauge] | 1.0 [atm. Abs.] |
| **Film Thickness** | 3.2 [mm] | 0.8 [mm] |
| $\mathbf{E_{ac}}$ | 14.4 [kJ/mol] | 56.1 [kJ/mol] |
| $\mathbf{A_c}$ | 1.2 [CA/hr] | $3 \cdot 10^6$ [CA/day] |
| $\mathbf{M}^{a}$ | 0.09 [arb. unit] | 0.16 [arb. unit] |
| $\mathbf{E_{af}}$ | -- | see footnote[b] |
| $\mathbf{A_f}$ | -- | see footnote[b] |
| $\mathbf{CA_{tank}}$ | 0.58 | 0.58 |

[a]PAV value based on value from Yuanchen's data (from group files) for 100 °C PAV Run. POV value is an average value for $M_{RTFOT}$ calculated from Liu, 1996.
[b]Fast-rate kinetics parameters determined using correlations provided by Jin et al., 2011.

## RESULTS

### Predicted Rate vs Actual Rate: Effect of Activation Energy

Before looking at a detailed comparisons including recycling agent effects, the aging rate of the virgin and control binders is compared to the predicted aging rate; the comparison emphasizes the relationship between binder activation energy and aging rate, and further shows that two binders coming from a single manufacturer and having the same PG grade may, nonetheless, age very differently. As discussed above, the virgin binder is a PG 64-22 from a given manufacturer, and, for estimation purposes, kinetics parameters for a binder from the same manufacturer and having the same PG grade where used to estimate oxidation rate (see above). Further, using relations proposed by Cui et al. (2014) and Glover (presentation, 2014), it is possible to relate PAV CA growth rate to PAV *Eac* and POV *Eac*. Key equations are presented, and the above-described relations are presented graphically in Figure D.2.

*CA Constant-Rate Growth Rate Equation (Arrhenius Form)*

$$\text{Rate} = A \cdot e^{-\frac{\text{PAV } E_{ac}}{R \cdot T}}$$

- Rate: CA growth Rate [CA/hr]
- *A*: Pre-exponential Factor [ CA/hr]
- PAV $E_{ac}$: PAV Constant Rate Activation Energy [kJ/mol]
- *R*: Ideal gas constant [kJ/mol·K]
- *T*: Temperature [K]

*Relation Between PAV $E_{ac}$ and PAV Pre-exponential Factor*

$$A = C_1 \cdot e^{C_2 \cdot \text{PAV } E_{ac}}$$

- *C1*: Constant, 0.0103 [CA/hr]
- *C2*: Constant, 0.3276 [mol/kJ]

*Relationship Between PAV $E_{ac}$ and POV $E_{ac}$*

$$\text{PAV } Eac = 1.89 \cdot \text{POV } Eac - 91.5$$

- POV $E_{ac}$: POV Constant Rate Activation Energy [kJ/mol]

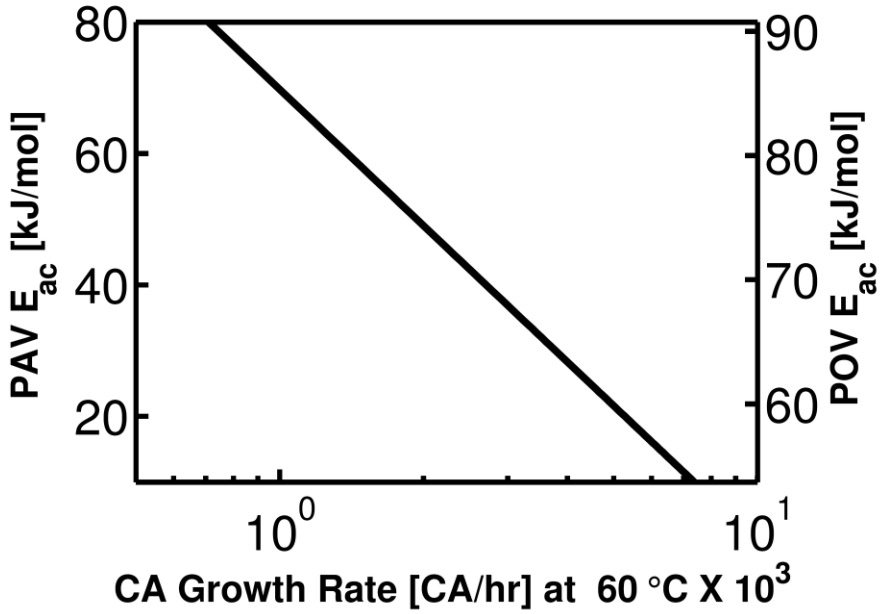


**Figure D.2. Graphical relation between PAV CA growth rate, PAV Eac, and POV Eac.**

Figure D.3 shows that the virgin and control binder CA growth rates are slower than the predicted CA growth rate. Although, the control best-fit CA growth line is shifted above the virgin line, the virgin and control binder growth rates are similar (0.0023 and 0.0021 [CA/hr], respectively) and probably cannot be statistically distinguished. The faster (0.007 [CA/hr]) predicted virgin growth rate is based on a PAV $E_{ac}$ value of 14.4 [kJ/mol] (same PG grade, same manufacturer binder, from TxDOT project 6009). In contrast, the virgin and control binder PAV $E_{ac}$ values were calculated to be 45 and 48 [kJ/mol] respectively. POV $E_{ac}$ values were also calculated and are shown.

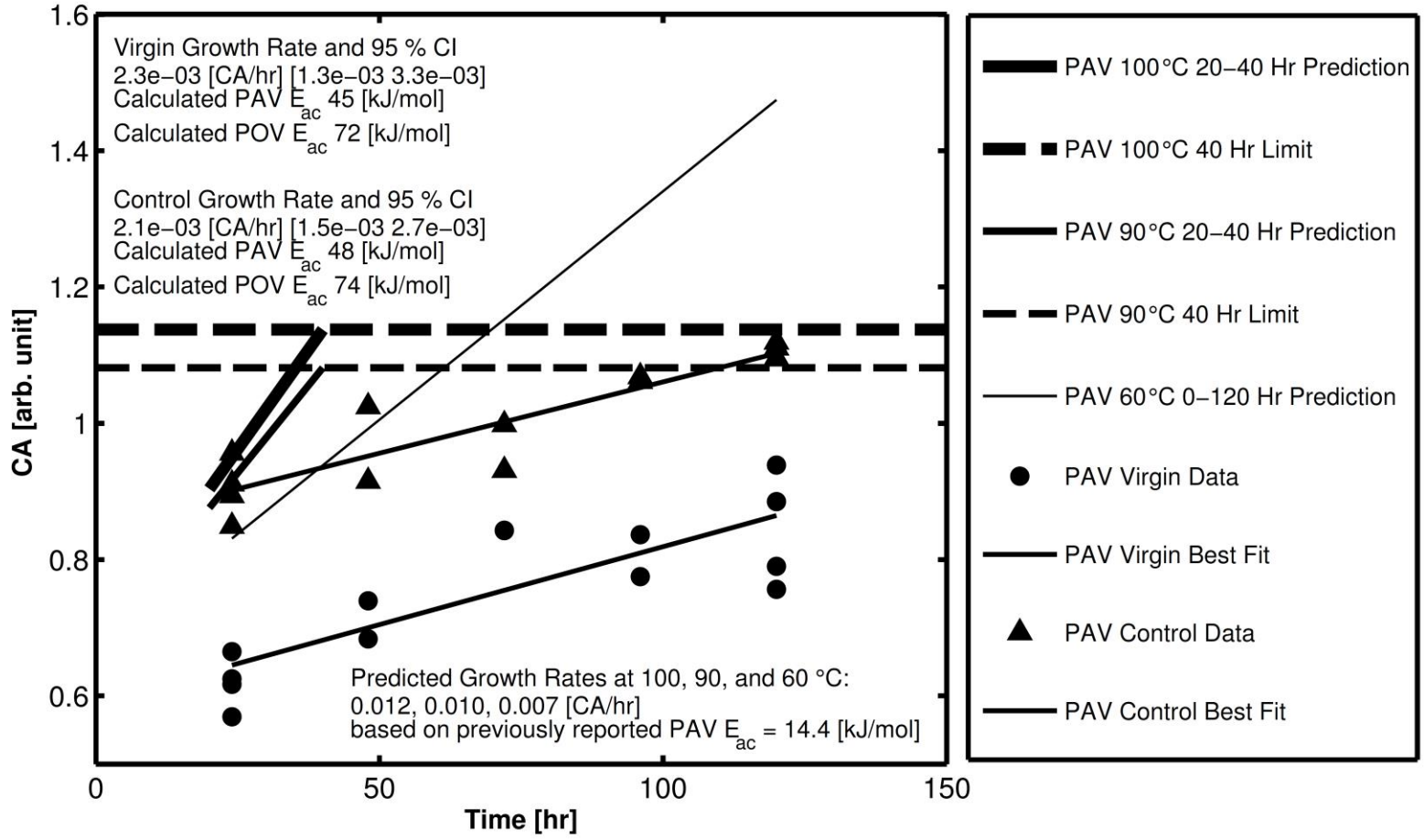


**Figure D.3. Comparison of virgin and control binder growth rates and activation energies with predicted growth rate based on a previously reported PAV *Eac* for a binder from the same manufacturer as the virgin binder and also having the same PG grade as the virgin binder.**

**Part I Results: Virgin Binder Compared to Virgin Binder with Recycling Agents**

Figure D.4 shows the individual, measured, PAV-aged CA values with best fit regression lines for each binder blend. Each graph represents a single binder blend (virgin is considered a blend here). On each graph, the ordinate range is set to 0.6 to simplify visual comparison of the growth rates. In particular it is noted that while addition of the T1 RA strongly increases measured CA, the high CA values result from the high CA content in the T1 RA rather than an increased aging rate. The graph on the bottom right shows all of the best-fit regression lines together (the T1 line has been shifted down for better visual comparison).

Figure D.5 presents the CA growth rate (slopes of regression lines from graphs in Figure D.4) for the virgin binder and each of the virgin-RA blends. A statistical comparison is made to compare the grow rate of each blend with the virgin binder growth rate. The p value represents the probability of seeing the measured difference between the blend and the virgin growth rate, due to measurement uncertainty, if in reality their growth rates are equal. Using a 90% confidence level, there is evidence that addition of P and TI RAs to the virgin binder reduces the CA growth rate. There is no evidence that any of the RAs increase the CA growth rate.

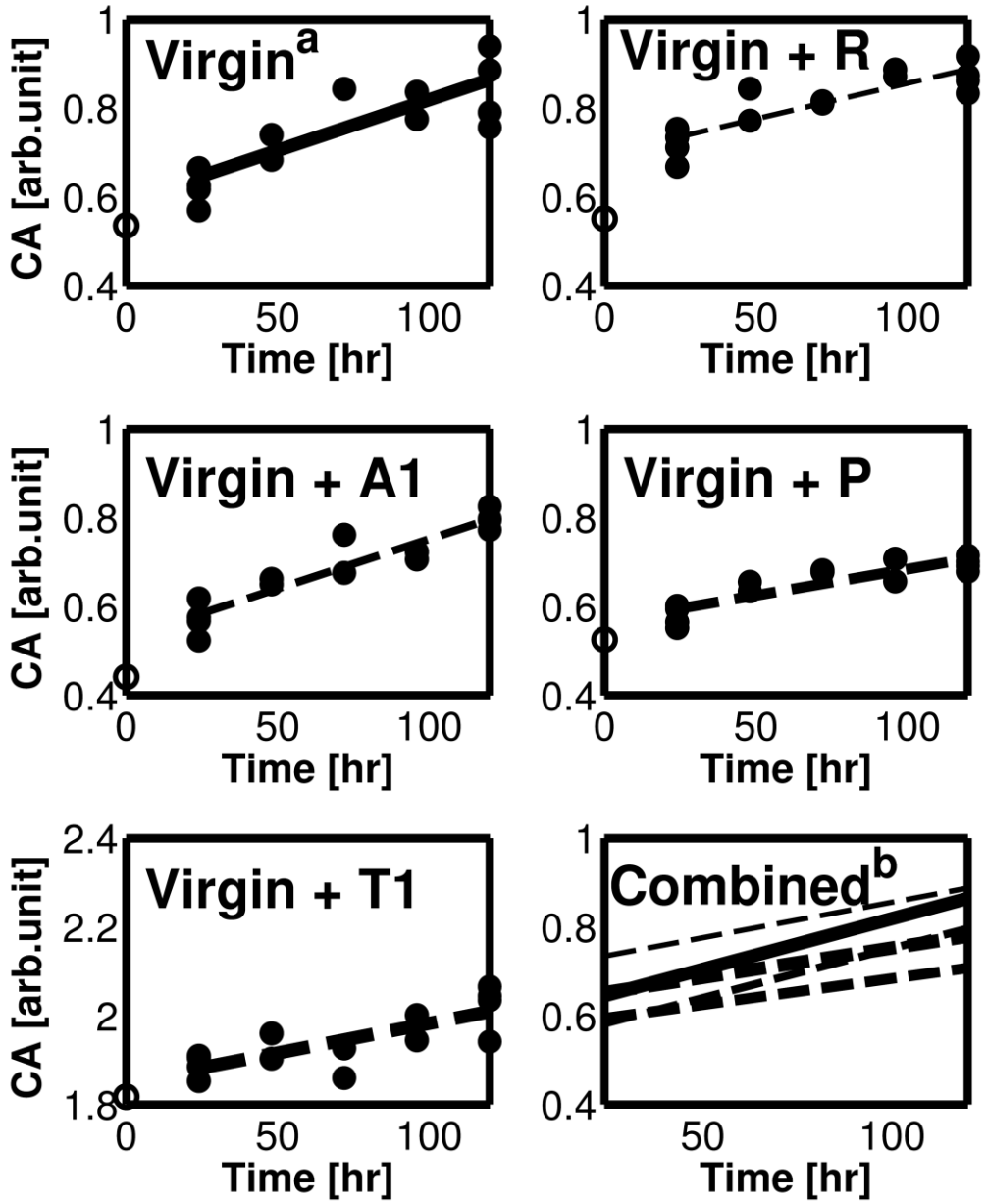


**Figure D.4. Carbonyl (CA) growth with time (60 °C, 20.7 atm. gauge, and 120 hr. total aging time). Unaged blend CA value shown as marker without fill at zero aging time. [a]Virgin asphalt is PG 64-22 from the Texas project. [b]The T1 blend best-fit regression line has been shifted down by 1.23 for better visualization of the relative slopes.**

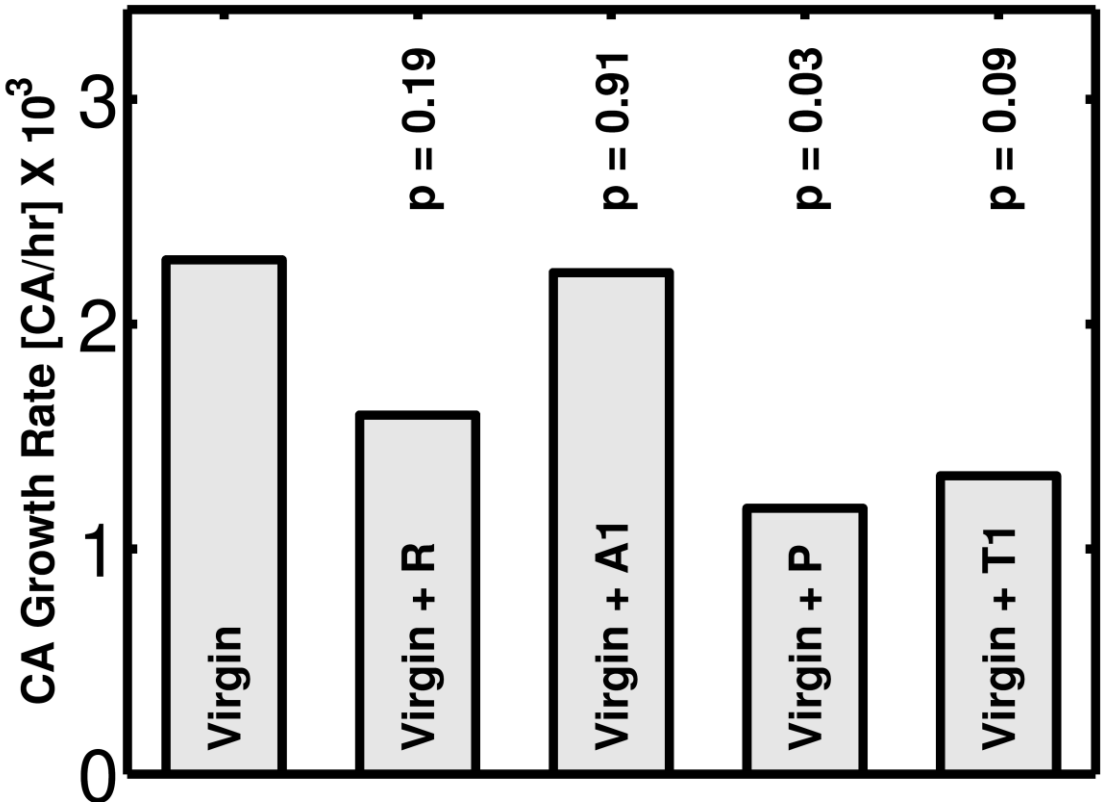


**Figure D.5. CA growth rates for the virgin asphalt and the four blends. Each p value represents the likelihood of finding the given blend growth rate and the virgin growth rate if their true growth rates are equal. The calculation is based on $t_o$ = (virgin slope – blend slope)/ sqrt((standard error virgin slope^2)+(standard error blend slope^2)). The p value is calculated from the t statistic as 2*probability(t>|$t_o$|) with degrees of freedom 14+14-4 = 24.**

**Part II Results: Control Binder Compared to Control Binder with Recycling Agents**

Figures D.6 and D.7 are analogous to figures D.4 and D.5 discussed above, but control binder (virgin plus recycled material, see above) replaces the virgin binder. Comparing figure D.6 to figure D.4 presented above, CA values are shifted up as expected. The reason is because the recycled material blended with the virgin binder has higher CA levels than the virgin binder. Looking at Figure D.7, the impact of the RAs on the control binder CA growth rate is analogous to the impact on the virgin growth rate (Figure D.5). Looking at the p values and using a 90% confidence level, as before, there is evidence that the A1, P, and T1 recycling agents decrease the CA growth rate. Again, there is no evidence that any of the RAs increase the CA growth rate.

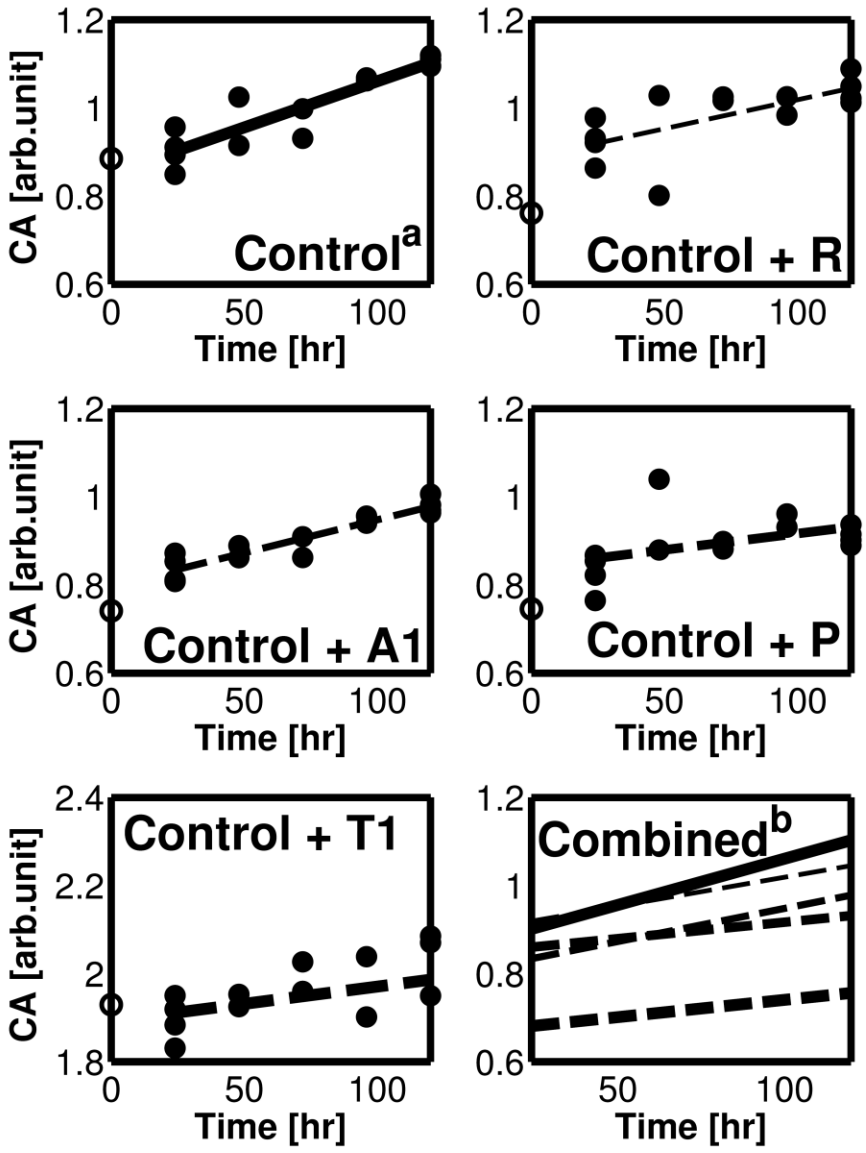


**Figure D.6. CA growth with time (60 °C, 20.7 atm. gauge, and 120 hr. total aging time). Unaged blend CA value shown as marker without fill at zero aging time. [a]Control asphalt is Virgin PG 64-22 from the Texas project with a RBR of 30% (10% RAP/20%RAS). [b]The T blend has been shifted down by 1.23 for better visualization of the relative slopes.**

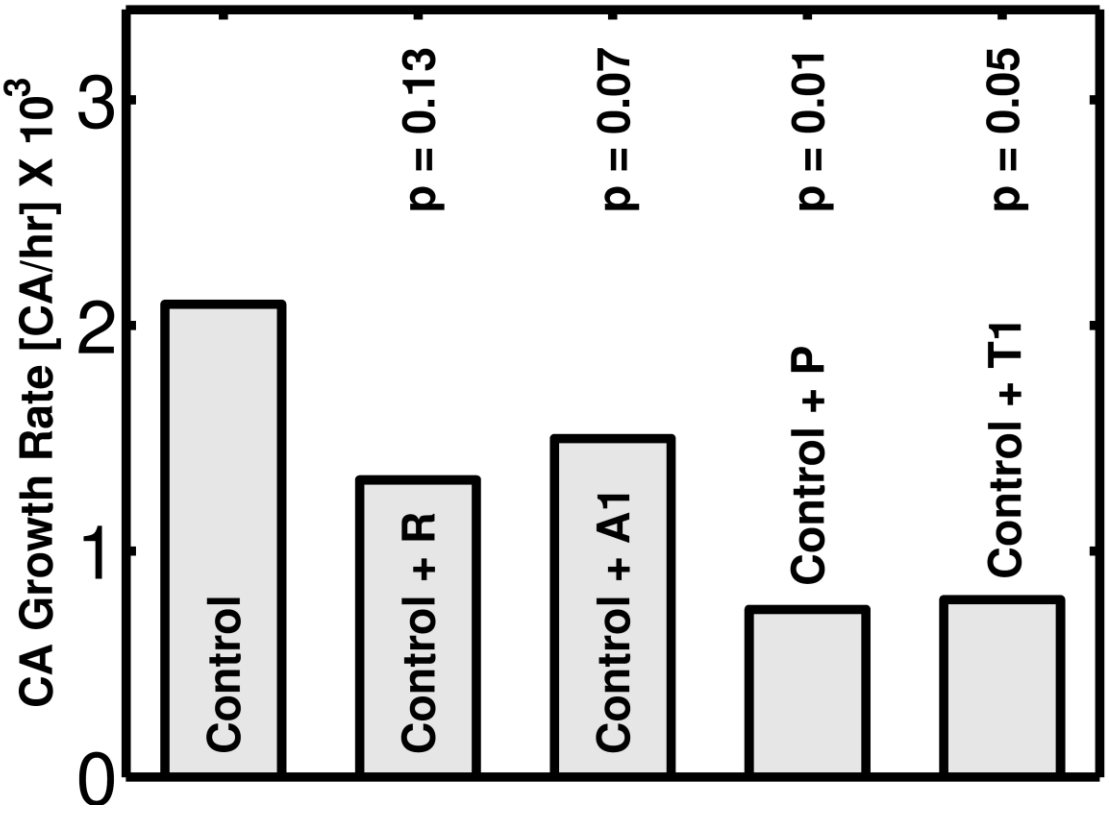


**Figure D.7: CA growth rates for the control asphalt and the four blends. Each p value represents the likelihood of finding the given blend growth rate and the control growth rate if their true growth rates are equal. The calculation is based on $t_o$ = (virgin slope – blend slope)/ sqrt((standard error virgin slope^2)+(standard error blend slope^2)). The p value is calculated from the t statistic as 2*probability(t>|$t_o$|) with degrees of freedom 14+14-4 = 24.**

**Part I and II Results Compared**

Figure D.8 presents the CA growth rates determined in both parts I and II. The trends match perfectly, but it appears that the RAs may have a stronger influence on the control binder than on the virgin binder, i.e. the RAs seem to reduce the CA growth rate more when added to the control binder than when added to the virgin binder. Alternatively, the evidence could be interpreted as a dilution effect, that is CA growth in the recycled binders may be slower than in the virgin binder and therefore the reduced CA growth rates are explained simply by a fraction of the blend being recycled material.

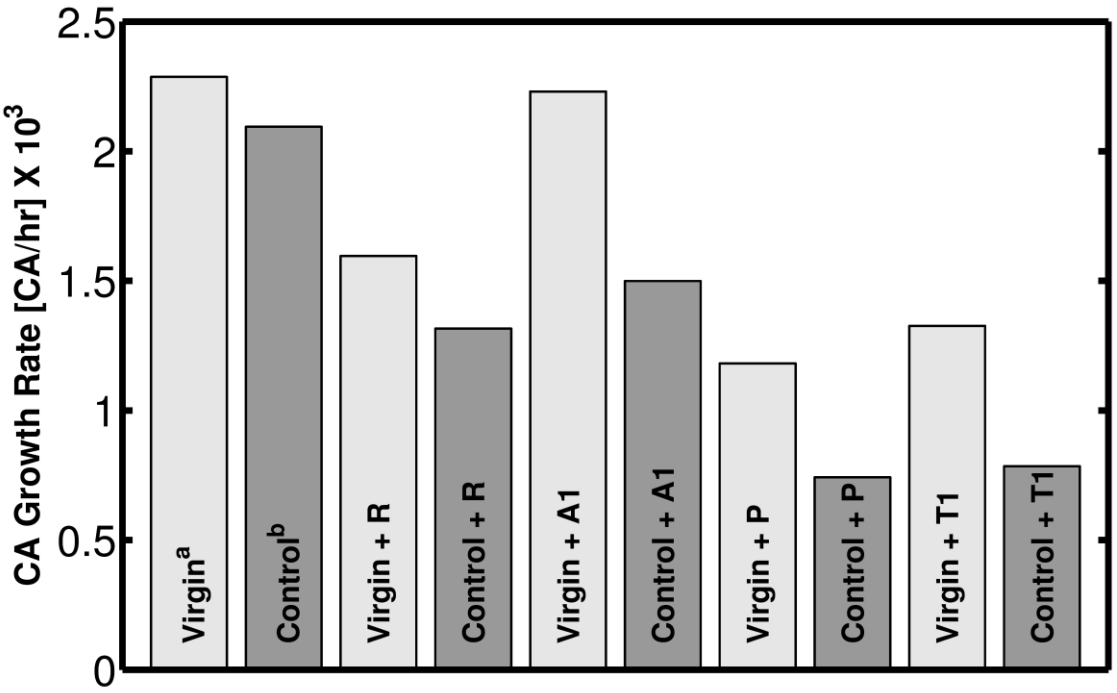


**Figure D.8: CA growth rate (60 °C, 20.7 atm. gauge, and 24–120 hr. aging). [a]Virgin PG 64-22 from the Texas project . [b]Control asphalt is virgin PG 64-22 from the Texas project with a RBR of 30% (10% RAP/20%RAS).**

**CONCLUSIONS**

There is no evidence that binder aging rates, as measured by CA growth, are increased by the RAs tested. Tests included virgin and control (virgin with RAP and RAS material) binders and virgin and control binder blends. Four recycling agents were included in the tests: R, A1, P, and T1. There is evidence that the P and T1 RA-virgin blends aged more slowly than the virgin binder. There is also evidence that A1, P, and T1 RA-control blends aged more slowly than the control blend.

SECTION II: EXUDATION DROPLET TESTING[+]

## INTRODUCTION

The efficacy of a binder recycling agent (RA) depends not only on the properties of the blend containing the RA, but also on the miscibility of the RA with the binder and other blend components. If the RA and the binder, or binder components, are not miscible, some components may exude from the blend, leaving behind a hardened blend.

Researchers have recognized the possibility of exudation and selective absorption into surrounding aggregate. The Shell Bitumen Handbook states that when a binder is "unbalanced" it may exude oily components into surrounding aggregate, which results in hardening of the remaining binder (Read and Whiteoak, 2003). Glover et al. (2014, Chap. 12: Absorption Spectrum Tests) studied selective absorption of binder components into limestone aggregates. Cutting the aggregates revealed darker outer penetration rings and fluorescing (under UV light) inner penetration rings. The inner rings were hypothesized to have resulted from light, non-polar, aromatic hydrocarbons traveling deeper into the aggregate than the darker components, which resulted in a darker ring closer to the aggregate surface. Interestingly, Glover et al. (2014) note that the absorptive process not only affects the remaining binder, but actually influences the physical properties of the aggregate (imparts viscoelastic characteristics).

In an effort to determine whether an asphalt can be considered balanced researchers from Shell Bitumen developed an exudation droplet test (Read and Whiteoak, 2003; Van Gooswilligeng et al., 1989), which has since been applied to asphalt additives. In brief, the exudation droplet test (described below) requires incubation of a binder droplet in a round recess of a marble slab and looks for a fluorescing ring surrounding the recess after incubation, which evidences exudation. Glaser and Porot (2014) applied the method to evaluate the miscibility of rejuvenating agents and binder.

Following the guidance of Glaser and Porot (2014) this work uses the exudation droplet test to evaluate the compatibility of recycling agents (RAs) with binder blends.

Additionally, in an effort to improve fundamental understanding of the exudation droplet test results the RAs used in this study and selected paraffinic materials are individually investigated.

---

[+] This work was performed as part of Phase II of project NCHRP 9-58, *The Effects of Recycling Agents on Asphalt Mixtures with High RAS and RAP Binder Ratios*.

## MATERIALS AND METHODS

### Materials

#### *Binder Blends*

The binder blends tested include those tested in the oxidation screening tests plus two additional blends from the Texas expanded set. Table D.2 provides a complete listing. For clarity, abbreviations used in Table D.2 are explicitly defined: RBR abbreviates recycled binder ratio, RAP abbreviates reclaimed asphalt pavement, RAS abbreviates recycled asphalt shingles, and RA, as above, abbreviates recycling agent.

**Table D.2. Binder Blends.**

| Blend Group | Base Binder | RBR wt.%[a] | RAP wt.%[b] | RAS wt.%[c] | RA | RA wt. %[d] |
|---|---|---|---|---|---|---|
| Virgin | TX 64-22 | 0 | 0 | 0 | -- | 0 |
| | TX 64-22 | 0 | 0 | 0 | R[e] | 10 |
| | TX 64-22 | 0 | 0 | 0 | P[f] | 10 |
| | TX 64-22 | 0 | 0 | 0 | A1[g] | 10 |
| | TX 64-22 | 0 | 0 | 0 | T1[h] | 10 |
| Control | TX 64-22 | 30 | 10 | 20 | -- | 0 |
| | TX 64-22 | 30 | 10 | 20 | R | 10 |
| | TX 64-22 | 30 | 10 | 20 | P | 10 |
| | TX 64-22 | 30 | 10 | 20 | A1 | 10 |
| | TX 64-22 | 30 | 10 | 20 | T1 | 10 |
| Additional TX Expanded | TX 64-22 | 50 | 25 | 25 | T1 | 10 |
| | TX 64-28 | 50 | 25 | 25 | T1 | 10 |

[a]wt. recycled material/wt. total blend
[b]wt. RAP/wt. total blend
[c]wt. RAS/wt. total blend
[d]wt. RA/wt. total blend
[e]re-refined lube oil
[f]paraffinic oil
[g]aromatic extract
[h]tall oil

#### *Additional Paraffinic Materials*

As mentioned above, in additional to individual study of the RAs, selected additional paraffinic materials are individually studied. In particular, Table D.3 details the four paraffinic materials selected (primarily based on availability):

**Table D.3. Selected Paraffinic Materials.**

| Material Name | Description | Manufacturer/Supplier | Remarks |
|---|---|---|---|
| **Sasobit** | paraffin waxes and hydrocarbon waxes | Sasol Chemicals LLC | warm mix additive, pellets (see results) |
| **Paraffin, Prills** | paraffin wax fume | J. T. Baker | pellets (much smaller than Sasobit pellets) |
| **Chap Aid** | see below[a] | Walgreens | personal product similar to ChapStick |
| **VWR 20 Vacuum Pump Oil** | 100% neutral paraffinic oil, solvent refined | Inland Vacuum Industries | -- |

[a]active ingredients - padimate O, 1.5%; petrolatum 45%; inactive ingredients – camphor, copernicia (carnauba) wax, cetyl alcohol, D&C red No 6 Barium Lake, fragrance, isopropyl lanolate, isopropyl myristate, lanolin, methylparaben, mineral oil, paraffin, propylparaben, whit wax.

***Marble Slabs***

The exudation droplet test requires a one-time-use marble slab with a round recess approximately 1 mm deep and 10 mm in diameter. The slabs used in the work reported herein come from the only known current supplier: Marini Marmi Srl (1 Via Gre, 24063 Castro (Bergamo), Italy). Marble slabs from Marini Marmi Srl have 5 recesses each.

***Ultraviolet Light and Camera***

After incubation, samples are illuminated using an ultraviolet light (UV) camera (additional discussion below). In this work a MineraLight Lamp (Model UVGL-58, multiband UV (-254/366), Ultra-Violet Light Products) was used on the short wave setting.

Images were taken using a digital camcorder with still imaging capability (Sony HandyCam HDR-CX440).

**Methods**

***Sample Preparation***

Prior work provides limited guidance regarding sample size and preparation; a complete technique is developed and described.

Guidance from prior work regarding sample size is limited to use of the term "droplet" (Read and Whiteoak, 2013) and a visual image in the presentation by Glaser and Porot (2014) showing a small droplet.

Initial testing in this work resulted in a determination that a 0.01 gram sample size is reasonable. At first a 0.005 gram sample size was attempted. This small sample was difficult to work with and left ample space in a recess. A 0.01 gram sample is somewhat easier to place in a marble slab recesses and provides a more substantial test sample. Even with the larger sample size spillage was limited, and in any case spillage appears to result primarily from the marble slab not being perfectly level during incubation rather than from overfilling.

Although the 0.01 gram samples were easier to manage, weighing and placement of clean samples required development of a specialized sampling procedure. Beads of asphalt were put onto small rectangles of aluminum (cut from a roll of aluminum sheeting available from the Home Depot) using a small spatula. Each bead was chilled in a freezer (about 10 minutes) and a sample was cut, using an X-ACTO knife, from the bead and placed onto a second, tared, rectangular piece of aluminum. Slight addition or removal was performed until the tared sample weight was 0.01+/-0.002 grams. Figure D.9 illustrates the the beads and the samples. Weighed samples (Figure D.9(b)) were transferred to the marble slab recesses using the X-ACTO knife and a small spatula. Figures of the weighed samples in the marble recesses are shown with the results.

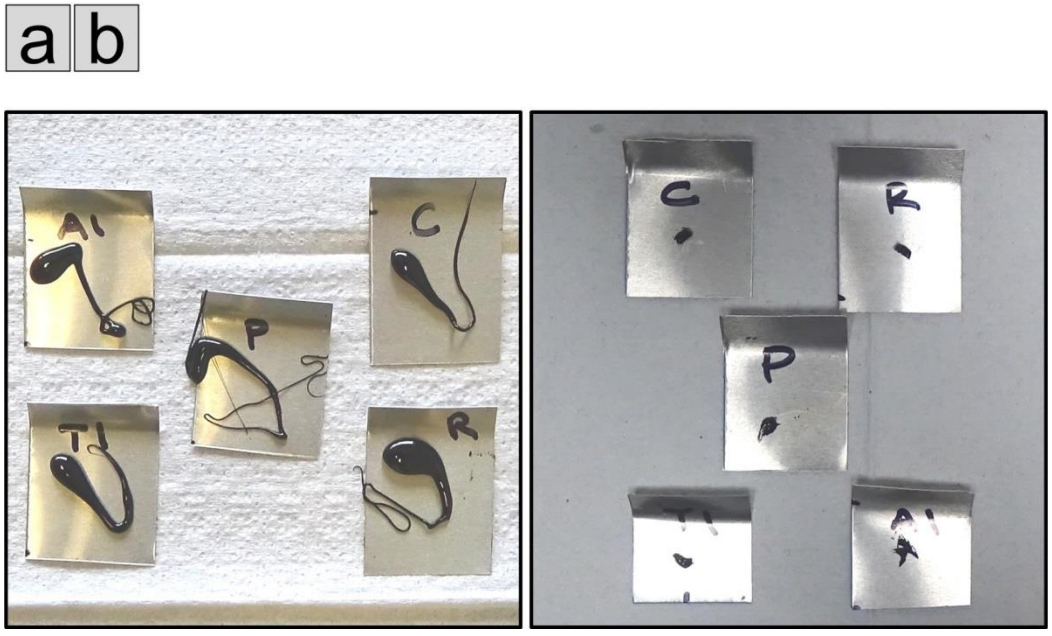


**Figure D.9. (a) Asphalt Beads (b) Weighed Asphalt Samples; example showing control blends.**

Slightly different preparation methods were used for the pure RA samples and the paraffinic material samples. The RAs are less viscous than the binder blends and sampling was performed using disposable glass pipets (VWR Pasteur Pipet, size 5.75 inch). The RAs were warmed in a 60 °C nitrogen blanketed oven for approximately 5 minutes to reduce viscosity. A pipet was used to place a single drop in a recess of a tared marble slab. The marble slab was subsequently weighed to determine the sample size. Paraffinic material preparation depended on the specific paraffinic material. The vacuum pump oil was sampled in the same manner as the RAs. The Chap Aid was sampled in the same manner as the binder blends, except placement of the bead onto the aluminum rectangle was simply a matter of cutting off an end portion from the original product using a plastic knife, and no chilling was required. Sasobit and the paraffinic prills are supplied as beads and therefore preparation involves only placing the beads into a recess: a single bead for Sasobit and a small clump of beads for the paraffin prills.

***Sample Incubation***

After placing the binder in the recess, the slab is placed in a nitrogen-blanketed oven. In this work, this step is referred to as incubation. The term aging is not used because aging refers to asphalt oxidation and the resultant rheological hardening, whereas here oxidation is intentionally minimized through use of a nitrogen blanket. Unless otherwise noted, the incubation period is 4 days and the incubation temperature is 60 °C.

***Sample Inspection and Imaging***

After incubation, the slab is illuminated using UV light to determine the width of any oily or light-colored ring surrounding the recess in the marble slab. Read and Whiteoak (2003), investigating balanced vs. unbalanced bitumen report that, "[r]ing widths vary from a few tenths of a millimeter for a balanced bitumen to several millimeters for an unbalanced bitumen." Glaser and Porot (2014) indicate that exudation is confirmed when the width of the light-colored ring exceeds 1.5 mm. In this work the handheld UV light was placed on the same surface as the marble slab and was positioned to be abutting the marble slab. All other lights in the room were turned off.

Images were taken using the digital camcorder. The camcorder was secured above the marble slab using a tripod. The focus was adjusted manually. Pictures were taking using the delay timer function to avoid accidental movement of the camera during imaging.

***Image Preparation***

Images were inserted into Visio software for editing and analysis. The edited Visio files were saved as JPEG file interchange format images with 300 ppi resolution. The JPEG images were inserted into this report.

## RESULTS

### Virgin and Control Blends

Figures D.10, D.11, and D.12 show images of the samples before and after incubation. Figure D.10 shows the results for the virgin blends, Figure D.11 shows the results for the control blends, and Figure D.12 shows the results for the additional Texas expanded blends. Each figure has three subfigures: (a) the samples in the marble slab recesses under natural light prior to incubation, (b) the samples in the marble slab recesses under natural light after incubation, and (c) the samples in the marble slab recesses under UV light after incubation.

Each of the samples shows a florescent ring under UV light and it was attempted to quantify the thickness of these rings. For each sample the thickest portion (ignoring apparent abnormalities such as blotchy spots) of the florescent ring was visually selected and its width was estimated. Estimation was performed in Visio by comparing the width of the recess (known to be 10 mm) with the width of the band at the selected portion. For each sample the ring portion selected as the thickest is indicated using double arrows and the thickness is provided in the center of the sample.

Examining the results for the virgin blends a few insights are noted. Although all of the florescent rings appear to have widths less than 1.5 mm, the P blend appears to have substantially more exudation than the virgin sample. The ring around the R blend, while not as wide as the ring around the P blend, also appears to be substantially wider than the ring around the virgin sample. The exudation from the A1 blend appears very similar to that of the virgin sample, and the T1 blend actually appears to have less exudation than the virgin sample.

Results for the control blends appear generally analogous to those for the virgin blends, but with increased exudation. The control blends include recycled binder and therefore it is not surprising that they show inferior miscibility (i.e. greater exudation) when compared with the virgin blends. As for the virgin blends, the control P and R blends show the greatest exudation, and the control without RA and TI blends show the least exudation. The P blend florescent ring exceeds the 1.5 mm miscibility limit stated by Glaser and Porot (2014).

The results for the two Texas expanded blends are somewhat surprising because they show less exudation than the control T1 blend. Recall that for both the virgin and control blend groups, the T1 blends showed relatively little exudation, and, as expected, the control plus T1 blend showed more exudation than the virgin plus T1 blend. Surprisingly, though, for the two Texas expanded blends, which have the highest RBR (0.5), there appears to be less exudation than for the T1 control blend, which had a RBR of 0.3.

As a final note on these results, it appears that the blends containing the A1 and T1 RAs tend to spread out in the recesses more completely than the other blends. In part, this probably reflects a greater ability of the A1 and T1 RAs to lower the viscosity of the resulting blend, given the same weight percent RA. Additionally, as the RBR for a given blend is increased the blend's viscosity increases and its ability to spread within a recess decreases (e.g. cf. virgin + T1 with control + T1). It is also possible that exuded material tends to inhibit the ability of a blend to wet and spread over the marble. This hypothesis agrees with the results shown for the blends containing the P RA. These blends result in a relatively large amount of exuded material and show limited spreading within their respective recesses; in effect the exuded material may be corralling the blend.

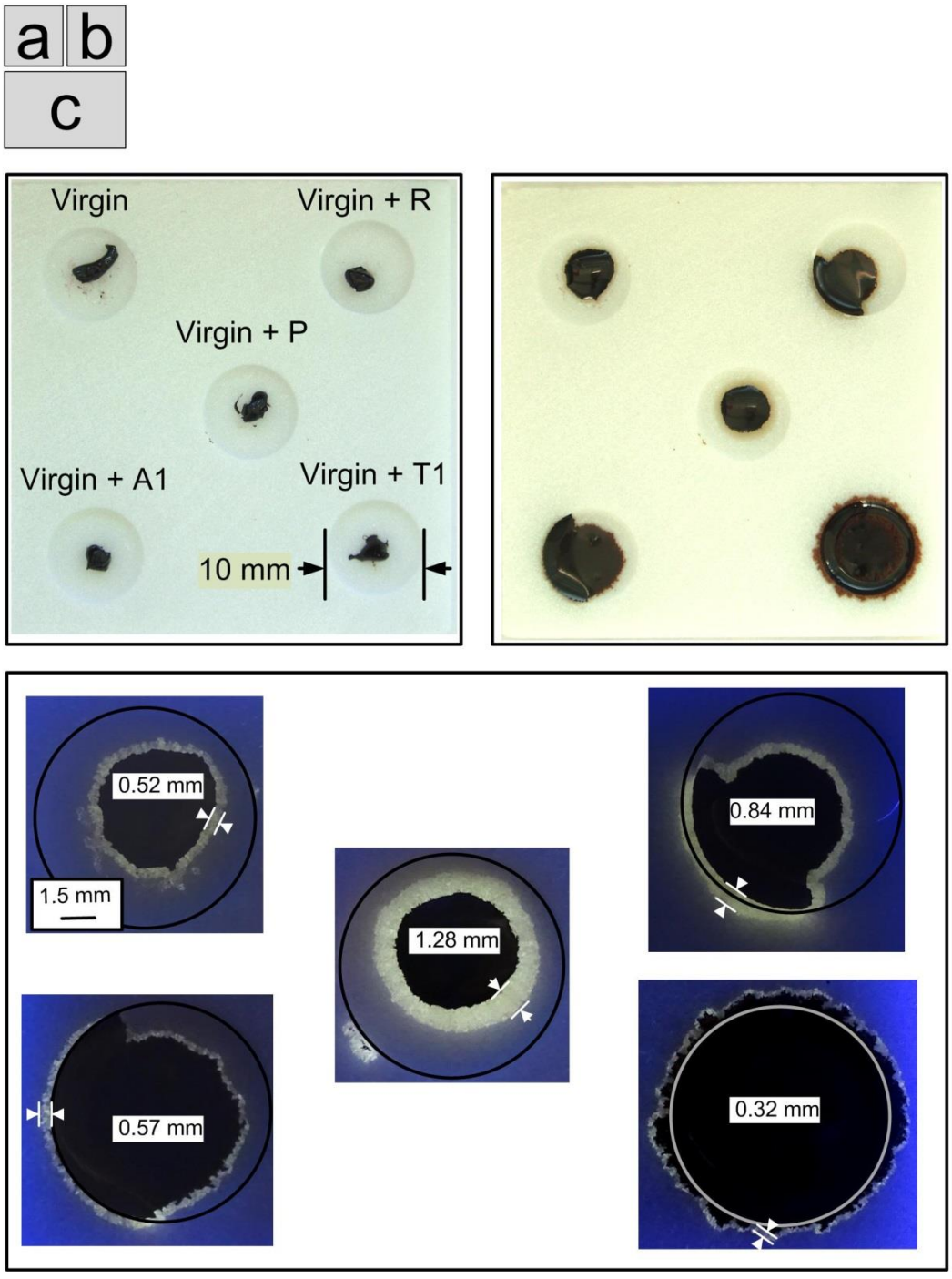


**Figure D.10. (a) Virgin Samples Under Natural Light Before Incubation (b) Virgin Samples Under Natural Light After Incubation (c) Virgin Samples Under UV Light After Incubation.**

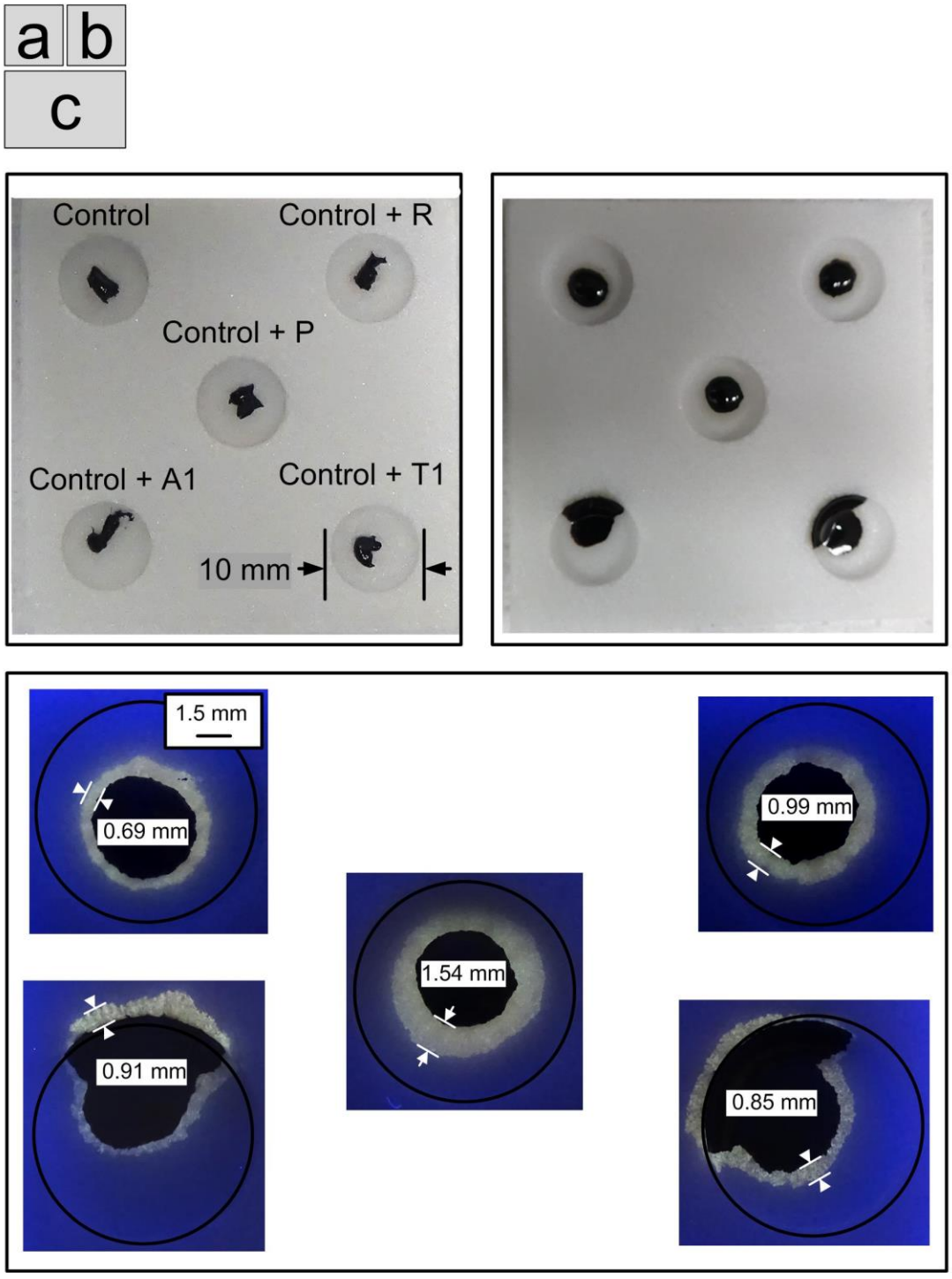


**Figure D.11. (a) Control Samples Under Natural Light Before Incubation (b) Control Samples Under Natural Light After Incubation (c) Control Samples Under UV Light After Incubation.**

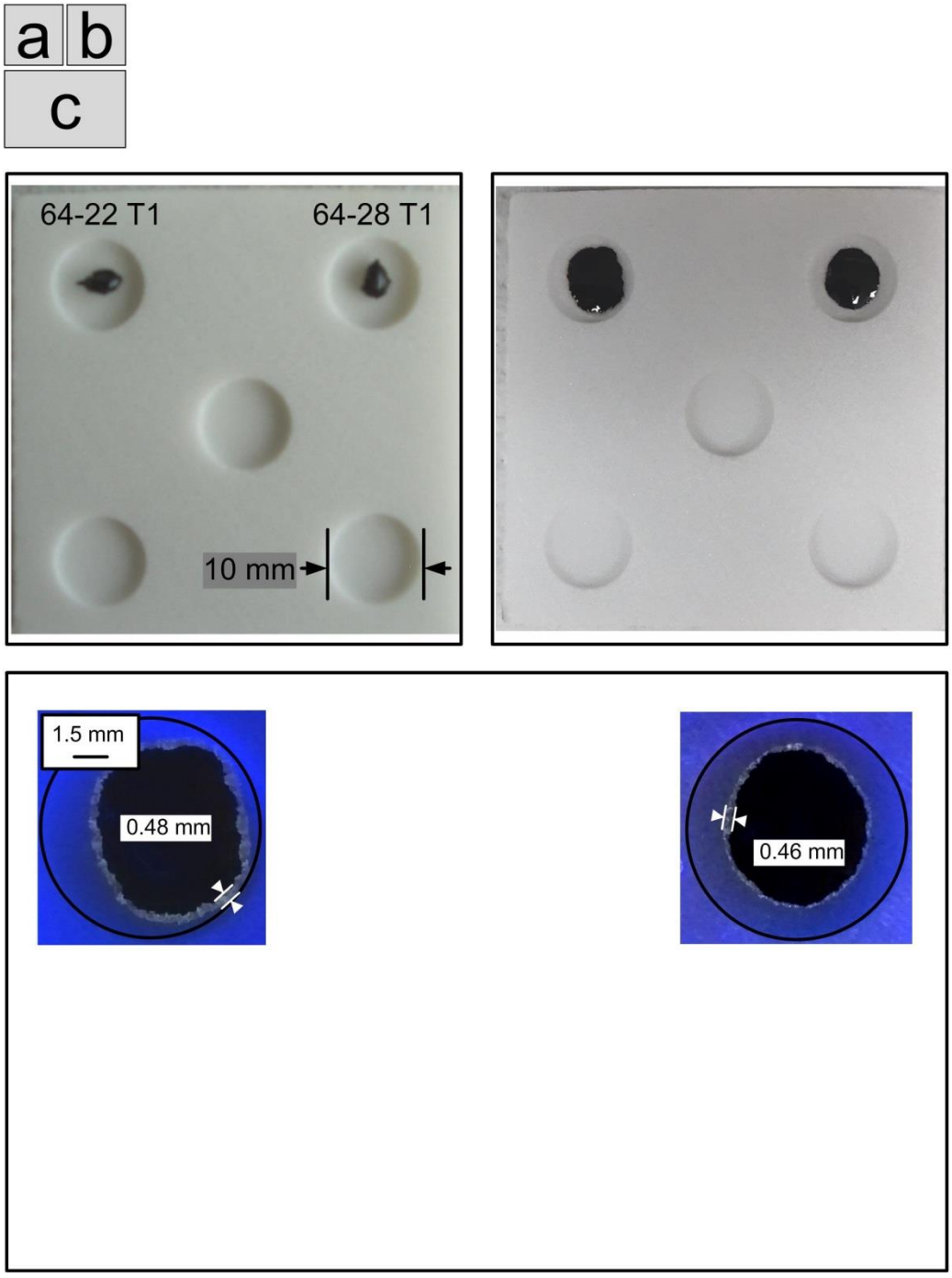


**Figure D.12. (a) Texas Expanded Samples Under Natural Light Before Incubation (b) Texas Expanded Samples Under Natural Light After Incubation (c) Texas Expanded Under UV Light After Incubation.**

Figure D.13 shows a plot of the ring widths for the virgin and control blends and puts the blends with the same RA side by side. This figure shows, possibly more clearly, that the control blends tend to have greater exudation (i.e. inferior miscibility). Again, the control with P RA blend is the only blend that has a ring width exceeding the 1.5 mm threshold.

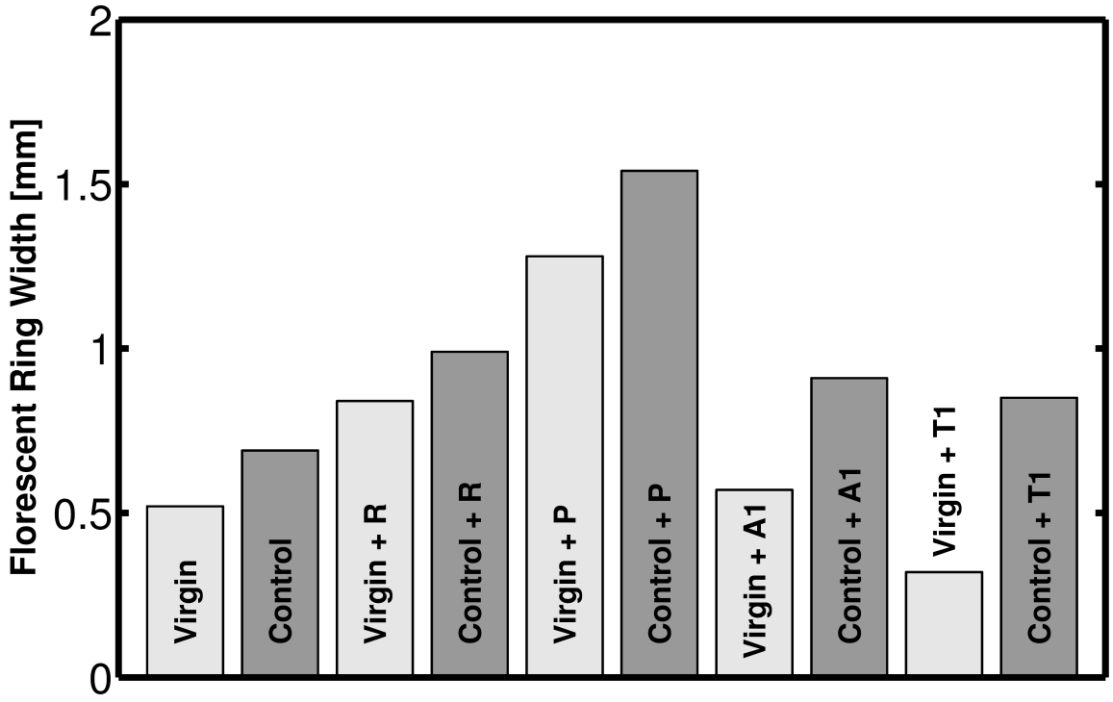


**Figure D.13. Virgin Blends and Control Blends Florescent Ring Widths Comparison.**

**Replicate Testing, T1 Blends**

Replicate testing was performed on all of the blends containing T1 RA. The incubated samples, under natural and UV light, are shown in Figure D.14. Figure D.15 shows a plot comparing the original test results with the results from the replicate tests. The trends for the original tests match the trends for the replicate tests, which confirms that the TX expanded blends show less exudation than the control plus T1 blend even though they have a higher RBR (0.5 vs 0.3). The replicate testing also provides evidence that the test method is sufficiently repeatable to distinguish these blends.

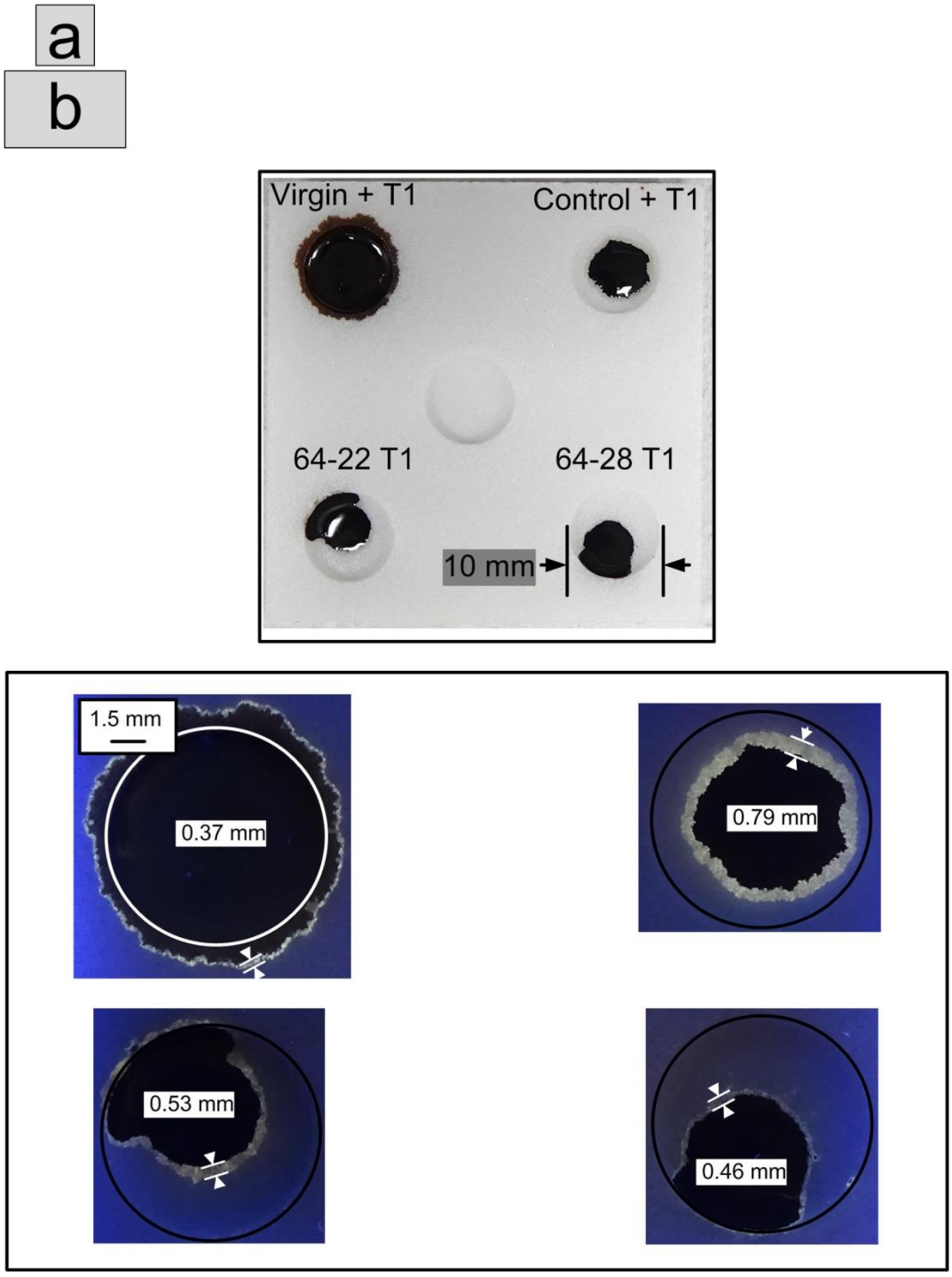


**Figure D.14. (a) T1 Replicate Samples Under Natural Light After Incubation (b) T1 Replicate Samples Under UV Light After Incubation.**

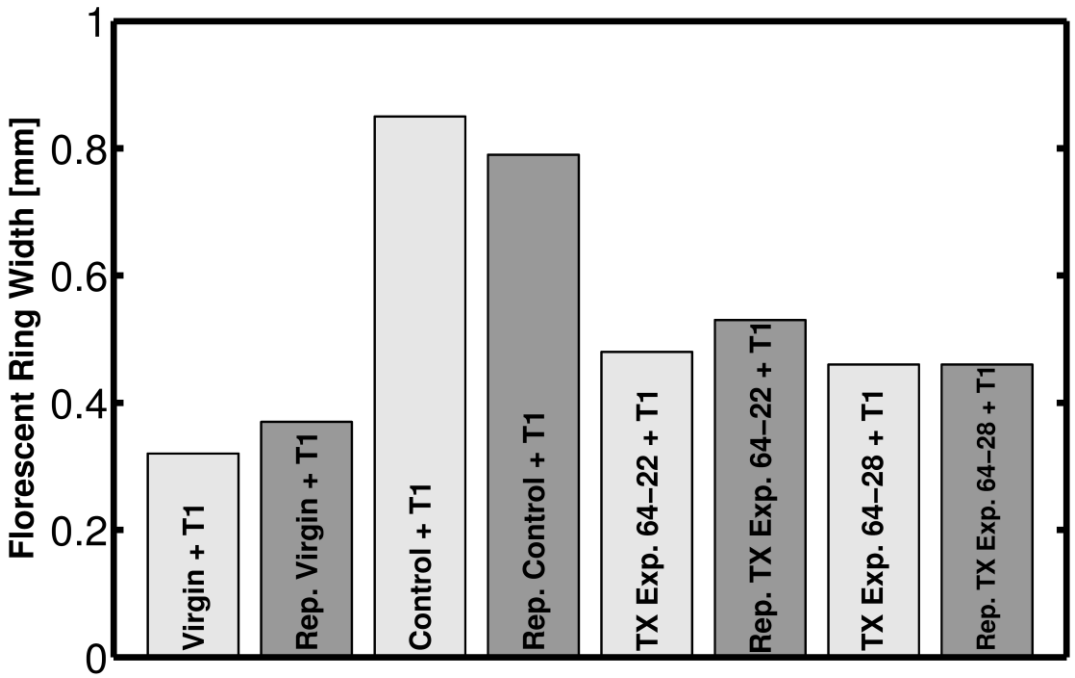


**Figure D.15. Original Tests on Blends with T1 RA and Replicate Tests, Florescent Ring Widths Comparison.**

**RA and Paraffinic Material Florescence Investigation**

Figure D.16 shows the RA samples before and after incubation. The subfigures follow the same pattern as virgin, control, and Texas expanded blends: (a) the samples in the marble slab recesses under natural light prior to incubation, (b) the samples in the marble slab recesses under natural light after incubation, and (c) the samples in the marble slab recesses under UV light after incubation. Sample sizes are as follows: R 0.01 g., P 0.012 g., A1 0.012 g., and T1 0.007 g. As above, incubation was in a nitrogen blanketed oven at 60 °C, but the incubation period was only 1 hour. The relatively short incubation period was intended to allow the samples to melt into the recesses and to begin diffusing into the marble.

Still considering Figure D.16, the RAs can be distinguished in terms of both florescence and diffusion. Surprisingly, under UV light the A1 RA produces a much brighter white florescent glow than any of the other RAs. The P RA produces a light glow, there is a very light florescent ring around the R RA (difficult to see in the image), and the T1 RA produces no perceivable florescence. Looking at subfigure (b), there are substantial differences in diffusion into the marble slab. Diffusion is ranked from most to least as: P, A1, T1, and R.

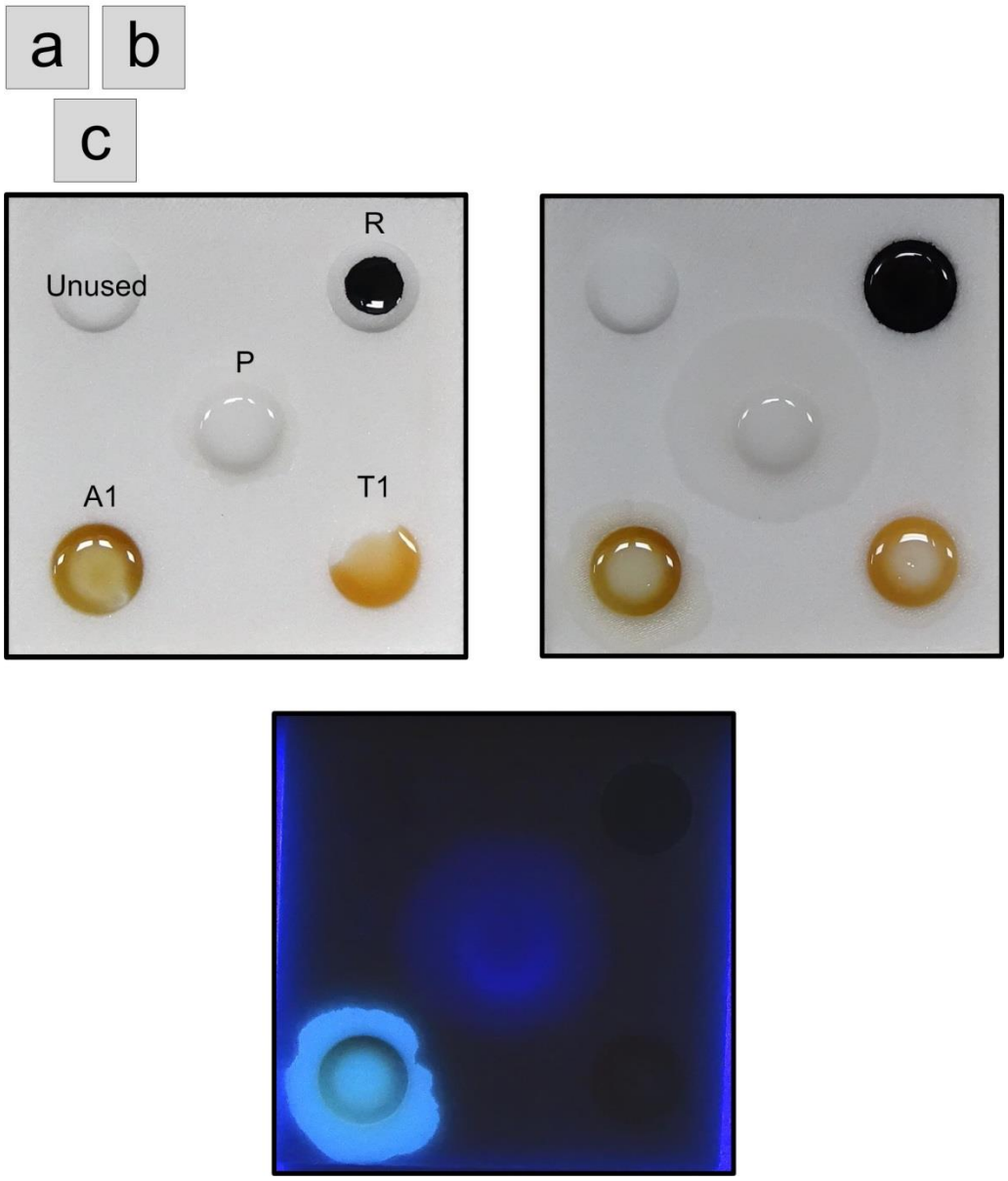


**Figure D.16. (a) RA Samples Under Natural Light Before Incubation (b) RA Samples Under Natural Light After Incubation[a] (c) RA Samples Under UV Light After Incubation[a]. [a]60 °C, 1 hr.**

Figure D.17 shows the selected paraffinic materials before and after two incubation periods. Sample sizes are as follows: Sasobit 0.012 g., paraffin prills 0.009 g., Chap Aid 0.013 g., and vacuum pump oil 0.015 g. The Sasobit material, which has a higher melting point than the other paraffinic materials, was incubated separately at 100–120 °C for two 10 minute periods. The other materials were incubated at 60 °C, as done

elsewhere in this work, for the incubation times shown in Figure D.17 (i.e. a 5 minute period followed by a 10 minute period). The left column of images (i.e. subfigures a, c, and e) shows the samples under natural light, and the right column of images (i.e. subfigures b, d, and f) show the samples under UV light.

As for the RAs, the individual paraffinic materials can be compared in terms of diffusion. Considering the images under natural light, the vacuum pump oil and Chap Aid appear to diffuse into the marble slab more than the paraffin prills and Sasobit. It is likely that Sasobit and the paraffin prills comprise slightly longer carbon chains, which prevent them from diffusing through the marble slabs as readily. This rapid diffusion seems comparable to the diffusion seen with the P RA shown above (slightly more diffusion for the P RA, but also 1 hour of incubation rather than 15 minutes). This corresponds with the fact that the P RA is a liquid at room temperature, and hence probably has carbon chain lengths closer to those of vacuum pump oil than to those of Sasobit or the paraffin prills. For all of the paraffinic materials an increase in diffusion can be seen from after the first incubation period to after the second incubation period.

The individual paraffinic materials can also be compared in terms of florescence under UV light. Consider the images under UV light, all of the paraffinic materials produce a light florescence (paraffin prills especially light ) comparable to the P RA, as expected. As the material spreads and diffuses, with incubation time, the florescent area widens but diminishes in intensity.

Comparing the results from the individual RAs and paraffinic materials with the results from the binder blends, one possibility is that the RAs cause the binders to exude their aromatic components, and the P RA causing the greatest exudation. Recall that the blends containing the P RA had the widest florescent rings. Although the P RAs fluoresce somewhat under UV light, it is clear that the A1 recycling agent, an aromatic extract, produces a much brighter florescence. Putting these results together, it is possible that the P RA has a strong ability to push out the aromatic components from a binder blend, which leads to a relatively wide and bright florescent ring. This makes sense from a polarity point of view because paraffinic materials are non-polar, whereas aromatic materials are polar and hence probably have poor miscibility with paraffinic materials.

Alternatively, it is possible that in the binder blend tests the paraffinic materials are being exuded but tend not to diffuse as readily as when they are tested by themselves. If for some reason, the paraffinic materials are exuded but remain relatively concentrated in the area immediately surrounding the blend, then the paraffinic material might produce a relatively bright florescent ring.

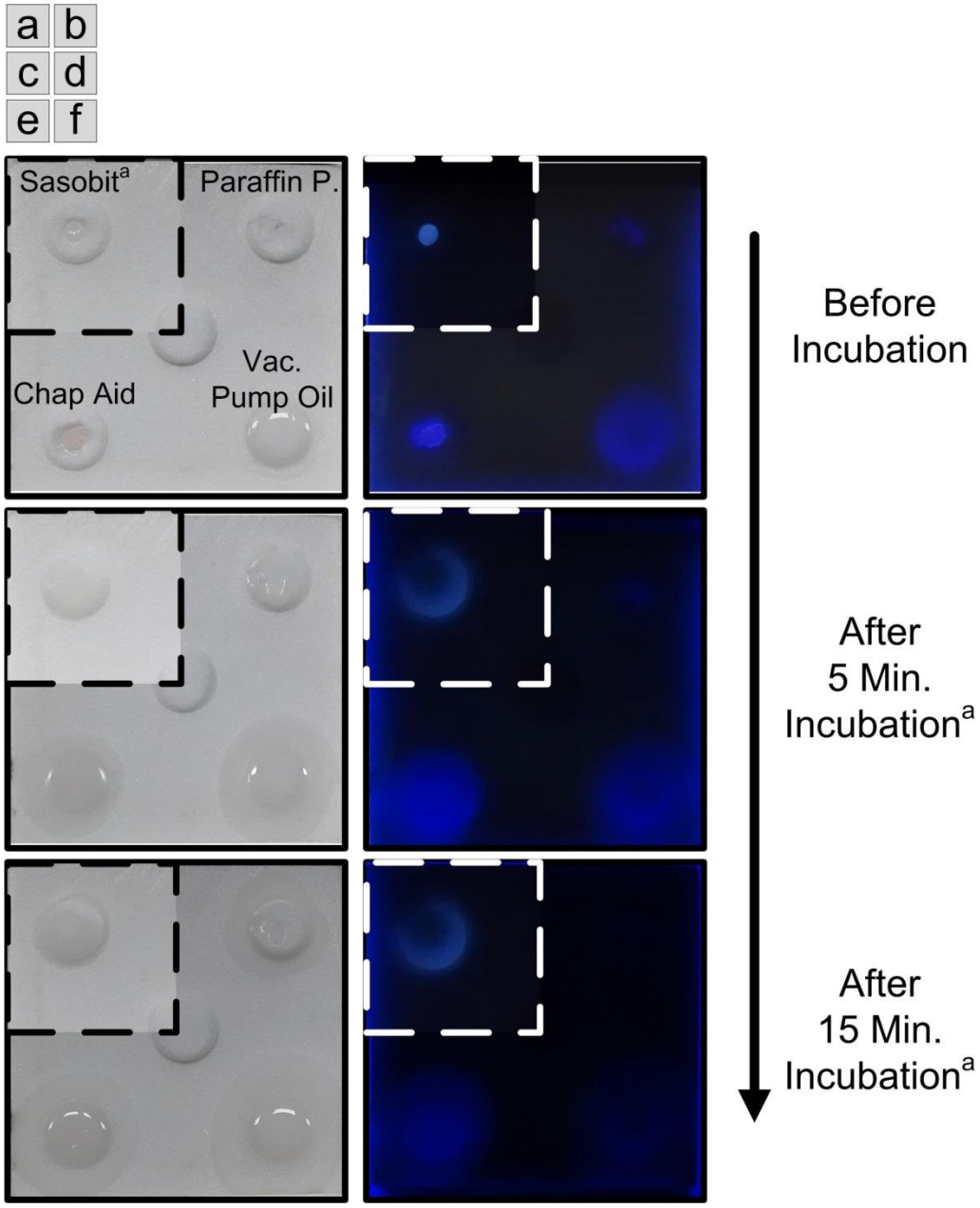


**Figure D.17. (a) Paraffinic Samples Under Natural Light Before Incubation (b) Paraffinic Samples Under UV light Before Incubation (c) Paraffinic Samples Under Natural Light After 5 Min. Incubation[a] (d) Paraffinic Samples Under UV Light After 5 Min. Incubation[a] (e) Paraffinic Samples Under Natural Light After 15 Min. Incubation[a] (f) Paraffinic Samples Under UV Light After 15 Min. Incubation[a]. [a]Sasobit incubated separately at 100–120 °C because of higher melting point, and incubation for 10 Min. and 20 Min. rather than 5 Min. and 15 Min.**

## CONCLUSIONS

A method for implementing binder blend miscibility testing was developed and virgin, control, and Texas expanded blends were tested. A sample size of 0.01 grams was found reasonable. Sample placement involved preparing an asphalt bead on a piece of aluminum, freezing the bead, and then cutting a sample from the bead and placing it onto a second, tared piece of aluminum. As specified in earlier work, samples were incubated for 4 days at 60 ° C. After incubation, samples were placed under UV light, images taken, and florescent ring widths compared. In general, the control blends showed greater exudation (wider rings) than the virgin blends. For both control and virgin blends, the blends containing P RA showed the widest rings, and the blends containing the R RA showed the second widest rings. Two additional Texas expanded blends having RBRs of 0.5 and T1 RA were also tested. Surprisingly, exudation rings were not as wide as the control T1 blend.

To improve understanding of the repeatability of the procedure, and of the miscibility of the T1 blends, testing was repeated on all 4 of the blends containing the T1 recycling agent. The replicate tests showed trends analogous to the original tests and provide evidence that the tests are sufficiently repeatable to distinguish the blends.

The RAs and selected paraffinic materials were tested individually to improve understanding of the binder blend results. Comparing the individual RA results, surprisingly, the A1 recycling agent (an aromatic extract) showed the strongest florescence under UV light followed by P, then R, and finally T1. The paraffinic materials showed moderate florescence under UV light, comparable to the P RA. The Chap Aid and vacuum pump oil showed a strong tendency to diffuse into the marble slab, which was also shown by the P RA. One hypothesis is that the RAs, especially the P RA, cause the binder blends to exude their aromatic components, which are then seen as florescent rings under UV light.

SECTION III: APPENDIX D REFERENCES

Cui, Y., Jin, X., Liu, G., and Glover, C. J. (2015). An Accelerated Method for Determining Asphalt Oxidation Kinetics Parameters for Use in Pavement Oxidation and Performance Modeling. *Petroleum Science and Technology* 32:2691–2699.

Glaser, R., and Porot, L. (2014). Miscibility and microstructure property changes in RAP binder / rejuvenator blends. In *12th ISAP Conference: A step forward toward a better understanding of the blending between recycled and virgin asphalts*. Raleigh, North Carolina.

Glover, C. J., Han, R., Jin, X., Prapaitrakul, N., Cui, Y., Rose, A., Lawrence, J. J., Padigala, M., Arambula, E., Park, E. S., and Martin, A. E. (2014a). *Evaluation of binder aging and its influence in aging of hot mix asphalt concrete.* Publication FHWA/TX-14/0-6009-2. College Station, Texas: Texas Transportation Institute, Texas A&M University System.

Read, J., and Whiteoak, D. (2003). *The Shell Bitumen Handbook*, 5th ed. Marsh Wall, London: Thomas Telford Publishing.

Van Gooswilligen, G., De Bats, F. TH., and Harrison, T. (1989). Quality of paving grade bitumen – a practical approach in terms of functional tests. In *Proceedings 4th Eurobitume Symposium*, pp. 290–297. Madrid, Spain.